



Exploring the Semiconducting Josephson Junction of Nanowire-based Superconducting Qubits

ANDERS KRINGHØJ

Ph.D. Thesis
Center for Quantum Devices
Niels Bohr Institute
University of Copenhagen

Academic advisor:
Charles M. Marcus

Assessment committee:
Attila Geresdi
Jukka Pekola
Jens Paaske

January 2020



Center for
Quantum
Devices

Abstract

This thesis investigates superconducting qubits based on proximitized InAs/Al nanowires. These qubits consist of semiconducting Josephson junctions, and present a gate tunable derivative of the transmon qubit. Beyond the gateable nature, this new qubit (the gatemon) exhibits fundamentally different characteristics depending on operating regime, which is the main focus of this thesis.

First, a systematic investigation of gatemon anharmonicity is presented. Here, we observe a deviation from the traditional transmon result. To explain this, we derive a simple model yielding information about the transmission properties of the semiconducting Josephson junction. In conclusion we find that the junction is dominated by 1–3 conduction channels with at least one channel reaching transmission probabilities greater than 0.9 certain gate voltages, in clear contrast to the sinusoidal energy phase relations that describe conventional transmon junctions.

Next, we present a new gatemon design, where a semiconducting region is operated as a field-effect-transistor to allow transport through the gatemon device without introducing a new dominant relaxation source. In addition, we demonstrate clear correlation between transport and transitional circuit quantum electrodynamics qubit measurements. In this geometry, for certain gate voltage, we observe resonant features in the qubit spectrum, both in transport and qubit measurements. Across the resonances, we carefully map the charge dispersion, which, at resonance, shows clear suppression orders of magnitude beyond what is traditionally expected. We explain this by an almost perfectly transmitting conduction channel, which renormalizes the charge of the superconducting island. This is in quantitative agreement with a developed resonant tunneling model, where the large transmission is achieved by a resonant level with nearly symmetric tunnel barriers.

Finally, we demonstrate compatibility with operation in large magnetic fields and the destructive Little-Parks regime. As we enter the first lobe of the oscillating qubit spectrum, we observe the emergence of additional coherent energy transitions. We explain these as transitions between Andreev states, which experience a path-dependent phase difference across the Josephson junction due to the phase twists associated with the Little-Parks effect. These observations are in qualitative agreement with numerical junction model.

Acknowledgments

During my time in QDev I have had the pleasure of working with numerous great people, who have all participated in creating a helpful atmosphere. I have come to greatly appreciate the culture where everybody helps and shares their experiences with each other regardless of subgroup or project.

I would like to express my deep gratitude to my supervisor, **Charlie Marcus**. Firstly, I would like to thank you for allowing me to do research in the group, and in your inspiring fashion teaching and motivating me to progress in research. Secondly, I want to thank you for always being available and for genuinely caring about my education. I find that truly remarkable given the amount of students and post docs in QDev.

Next, I would like thank the “original” gatemon team **Karl Petersson**, **Thorvald Larsen**, and **Lucas Casparis**, who have all played a tremendous role in my education as an experimentalist. During my work with you, **Karl**, I have been impressed with your ability to always come up with ideas on how to proceed, on everything from troubleshooting the setup, the fridge or the fabrication recipes, to dealing with theoretical questions while planning experiments or in analysis. Many of the first hands-on skills and basic understanding of the relevant concepts I had to learn in the beginning of my time in QDev, I learned from **Thorvald**. Over the years we have developed a close partnership with discussions at the experimental setups, in the office, and over countless cups of coffee. I have truly appreciated working with you and appreciated the friendship we have developed. **Lucas**, I also want to give you a big thanks for your guidance in measurements, especially in my early days in QDev. Besides being a great colleague I have also enjoyed all our laughs and discussions in the office on everything from sport’s results to children advice.

I also want to thank **Bernard van Heck**, who despite only being in QDev for three months managed to play an incredible role in my PhD. I really enjoyed our three months of experiments together and all our collaborations since.

I owe a big thanks to **Rob McNeil**, who fabricated numerous devices that I was privileged to measure. I am very thankful for that. And thank you for always doing it with a smile, you have many times affected my mood in a

positive way. Many thanks to **Marina**, **Karthik**, **Maren**, **Karolis**, **Aga**, **Sachin**, and **Shiv** for carrying the fabrication of some of the devices presented in this thesis. And a special thanks to you **Shiv** for taking your time in teaching me how to use the fabrication tools, always with valuable explanations and sharing your advices. I would also like to thank both **Oscar Erlandsson** and **Deividas Sabonis**, who I have worked closely with in several experiments, learning from your experiences and input. I would also like to thank **Ivana Petkovic** for a good partnership while you were here. Also a thank you to **Judith Suter** and **Eoin O'Farrell** for working hard tying to make life easier for the rest of us during our common project. Big thanks to **Sepehr Ahmadi** for helping me with measurements.

A big thanks to **Peter Krogstrup**, **Jesper Nygård** and their team, who have provided the nanowire materials that made this research possible.

I would like to give special thanks to **Natalie Pearson**. Although our projects turned in different directions, I really enjoyed working with you, and sitting next to you for more than three years, you have been a great support and a good friend. I would also like to thank **Albert Hertel** for always being open to a question or discussions in our office, and for valuable feedback on the thesis.

A thank you to **Ferdinand Kuemmeth** for many useful advices, in particular in the beginning of my PhD. I would like to thank **Karsten Flensberg**, **Michael Hell**, and **Martin Leijnse** for fantastic theory input, who led to the understanding of gatemon anharmonicity and the ideas of the renormalization of the charging energy. I would also like to thank the theorists in Santa Barbara, who were always helpful with any request I might have had. Special thanks to **Dima Pikulin** for your most valuable input on RCSJ modeling. Also special thanks to **Georg Winkler** for the collaboration on modeling of Andreev states, which have been crucial in understanding the (at first) mysterious behaviour of full-shell gatemon qubits in a magnetic field.

During my PhD I had the pleasure of collaborating with the group in Delft. Thanks to **Angela**, **Arno**, **Gijs**, **James**, **Leo**, and **Willemijn**, who I all enjoyed interacting with and for welcoming me for a couple of visits.

I also had the fantastic opportunity of visiting **Will Oliver's** lab at MIT for a month. Many thanks to you, **Will**, for welcoming me to the group. Special thanks to **Morten Kjærgaard** for organising everything and for having me in the subgroup. And for welcoming me and my family, we all greatly

appreciated spending time with you and your family. Special thanks to **Ami Greene**, who I partnered up with for most of my stay. Thank you for sharing your work and allowing me to participate in your research. In general, the whole group were all very open, and all helped making my stay memorable.

I am very thankful to **Attila Geresdsi**, **Jukka Pekola**, and **Jens Paaske** for taking their time to be in my committee and wanting to read the thesis.

I would like to thank **Fabio**, **Sole**, and **Alexander**, who I have developed great friendships with and despite never working closely with you, we have had countless useful scientific discussions. And of course many valuable non-scientific discussions. Thanks to **Asbjørn** for many good moments all the way from day one. I would also like to thank our fantastic administrative staff, **Dorthe**, **Katrin**, **Maria**, **Marianne**, **Tina**, who are always willing to help, it is greatly appreciated. Thanks to **Ruben** for sharing his expertise on the electronic setup. Also a big thanks to all the technical and software staff for contributing to experiments running as smooth as possible and for always being helpful. At last thanks to all the people in **QDev** who participated in making the lab a place I have enjoyed coming and creating a nice working environment.

Finally, I would like to thank friends and family for their support throughout my PhD with special thanks to **Sarah** for keeping our family on track in stressful times and to my daughter **Ellinor** for making it much easier to remember that failed experiments are not the end of the world.

Contents

1	Introduction	1
1.1	Thesis outline	4
2	Circuit Quantum Electrodynamics	7
2.1	The <i>LC</i> oscillator	8
2.2	Anharmonic oscillators	12
2.3	Semiconductor-based superconducting qubits	19
2.4	Qubit readout and manipulation	29
2.5	Hybrid cQED - Majorana transmon	34
3	Experimental Methods	35
3.1	Device fabrication	35
3.2	Mounting the device	38
3.3	Measurement setup	40
3.4	Measurement Techniques	43
4	Anharmonicity of a Superconducting Qubit with a Few-Mode Josephson Junction	51
4.1	Introduction	52
4.2	Theory	54
4.3	Anharmonicity measurements	56
4.4	Anharmonicity analysis	58
4.5	Conclusions	60
5	Deterministic Dielectrophoretic Assisted Assembly of Nanowire-based Gatemon Qubits	63
5.1	Introduction	64
5.2	Nanowire assembly	64
5.3	Qubit measurements	68
5.4	Conclusions	70

6 Controlled DC Monitoring of a Superconducting Qubit	71
6.1 Introduction	72
6.2 Relaxation of leaded gatemon qubits	74
6.3 Correlation of DC and cQED measurements	78
6.4 Conclusions	81
6.5 Experimental setup	81
6.6 RCSJ modelling details and additional transport data	83
7 Suppressed Charge Dispersion via Resonant Tunneling in a Single-Channel Transmon	85
7.1 Introduction	86
7.2 Resonant tunneling model	88
7.3 Charge dispersion measurements	90
7.4 Charge dispersion analysis	93
7.5 Conclusions	95
7.6 Extended theory	95
7.7 Transport measurements	100
7.8 Charge dispersion extraction	101
7.9 Spectroscopy and charge dispersion in the open regime	102
8 Phase-twisted Andreev States in Proximity-Induced Semiconducting Josephson Junctions	105
8.1 Introduction	106
8.2 Field compatible device	107
8.3 Phase-twisted Andreev states	108
8.4 Numerical simulations	111
8.5 Time domain measurements	113
8.6 Field dependence of resonator frequency	114
8.7 Gate dependence in zeroth and first lobe	116
8.8 Charge dispersion in field	117
8.9 Conclusions	120
9 Outlook	123
Appendix A Fabrication	125
Appendix B Fabrication	129
References	133

List of Publications

The work of this thesis has resulted in the following publications:

A. Kringhøj, L. Casparis, M. Hell, T. W. Larsen, F. Kuemmeth, M. Leijnse, K. Flensberg, P. Krogstrup, J. Nygård, K. D. Petersson, and C. M. Marcus, “Anharmonicity of a superconducting qubit with a few-mode Josephson junction”, *Phys. Rev. B* **97**, 060508(R) (2018).

L. Casparis, M. R. Connolly, M. Kjaergaard, N. J. Pearson, **A. Kringhøj**, T. W. Larsen, F. Kuemmeth, T. Wang, C. Thomas, S. Gronin, G. C. Gardner, M. J. Manfra, C. M. Marcus, and K. D. Petersson, “Superconducting gatemon qubit based on a proximitized two-dimensional electron gas”, *Nat. Nanotechnol.* **13**, 915 (2018).

L. Casparis, N. J. Pearson, **A. Kringhøj**, T. W. Larsen, F. Kuemmeth, J. Nygård, P. Krogstrup, K. D. Petersson, and C. M. Marcus, “Voltage-controlled superconducting quantum bus”, *Phys. Rev. B* **99**, 085434 (2019).

A. Kringhøj, T. W. Larsen, B. van Heck, D. Sabonis, O. Erlandsson, I. Petkovic, D. I. Pikulin, P. Krogstrup, K. D. Petersson, and C. M. Marcus, “Controlled dc Monitoring of a Superconducting Qubit”, *Phys. Rev. Lett.* **124**, 056801 (2020).

A. Kringhøj, B. van Heck, T. W. Larsen, O. Erlandsson, D. Sabonis, P. Krogstrup, L. Casparis, K. D. Petersson, and C. M. Marcus, “Suppressed Charge Dispersion via Resonant Tunneling in a Single-Channel Transmon”, in review, arXiv:1911.10011 (2019).

D. Sabonis*, O. Erlandsson*, **A. Kringhøj***, T. W. Larsen, I. Petkovic, B. van Heck, P. Krogstrup, K. D. Petersson, and C. M. Marcus, “Little-Parks effect in a semiconductor-based superconducting qubit”, in preparation.

A. Kringhøj, G. W. Winkler, T. W. Larsen, D. Sabonis, O. Erlandsson, P. Krogstrup, B. van Heck, K. D. Petersson, and C. M. Marcus, “Phase-twisted Andreev States in Proximity-Induced Semiconducting Josephson Junctions.”, in preparation.

*These authors contributed equally to this work.

List of Figures

2.1	LC circuit sketch and potential	10
2.2	Josephson circuit sketch and potential	13
2.3	Josephson circuit sketch coupled to voltage gate	14
2.4	Numerical solutions to transmon Hamiltonian	15
2.5	Cooper pair box and transmon circuit sketch	16
2.6	Short junction Josephson potential	21
2.7	Andreev eigenenergies and energy gap at $\phi = \pi$	24
2.8	Numerical solutions to the two-level Hamiltonian	25
2.9	Anharmonicity and charge dispersion as a function of transmission	27
2.10	Numerical solutions showing poisoned charge dispersion spectrum	28
2.11	Coupled qubit-resonator circuit sketch	30
2.12	Bloch sphere	33
3.1	Device overview of gatemon devices	36
3.2	Device packaging	39
3.3	Schematic of the experimental setup 1	42
3.4	Schematic of the experimental setup 2	43
3.5	Examples of common VNA measurements	45
3.6	Reduced schematic of demodulation circuit	47
3.7	Examples of common time domain measurements	50
4.1	Qubit device and Josephson potential	53
4.2	Spectroscopy scans to probe the anharmonicity	56
4.3	Results of the spectroscopy and anharmonicity measurements	58
4.4	Comparison of the anharmonicity data and model	59
5.1	DEP wafer overview	65
5.2	Device overview illustrating the fabrication process	66
5.3	Device overview of the finished DEP qubit device.	67
5.4	Power scans at zero junction gate voltage	68

5.5	Coherence of DEP assembled qubit devices	69
6.1	Device geometry and concept	73
6.2	Comparison of a leaded vs a nonleaded gatemon device	75
6.3	Qubit performance as a function of V_{FET}	76
6.4	Circuit model of the relaxation rate	77
6.5	Comparison of DC and cQED measurements	79
6.6	Schematic of the experimental setup of the DC experiment . . .	82
6.7	Supporting transport measurements	83
7.1	Device geometry and spectroscopy close to pinch-off	87
7.2	Resonant tunneling model	89
7.3	Charge dispersion measurements	91
7.4	Extracted charge dispersion and model result	92
7.5	Charge dispersion of the $0 \rightarrow 2$ transition	94
7.6	Properties of the bound state energy obtained from the resonant level model	98
7.7	Comparison of DC transport and cQED measurements across the two resonances	100
7.8	Examples of charge dispersion extraction	101
7.9	Charge dispersion in open regime	103
8.1	Field compatible device and Little-Parks effect	107
8.2	Damping of the resonator	109
8.3	Measurements of phase-twisted Andreev transitions	110
8.4	Numerical modeling of the flux-dependent Andreev states . .	112
8.5	Time domain measurements of Andreev transitions	114
8.6	Full measurement of the lobe-dependent resonator damping .	115
8.7	Corresponding resonator illustrating the damping effects . .	116
8.8	Comparison of zeroth and first lobe two-tone spectroscopy .	117
8.9	Qubit behavior at low V_Q	118
8.10	Mapping the qubit in the first lobe	118
8.11	Mapping the charge dispersion in the first lobe	120

1

Introduction

Over the last hundred years our understanding of fundamental physics has undergone fascinating and revolutionary progress with the birth and development of quantum mechanics. The first steps of quantum mechanics came in the early 1900 when the unification of electrodynamics had recently been achieved by Maxwell. The understanding of other fundamental laws had led to incredible industrial breakthroughs and some physicists even argued that our overall understanding of the world was complete. However, in the following period, developments in quantum mechanics radically changed the perception of the world with pioneering work revealing the peculiar nature of quantum mechanics. A nature revealing itself with famous examples such as the quantization of light proposed by Max Planck, which was later refined by Einstein to explain the photoelectric effect. Not long after, Bohr explained the stability of atoms via electron orbitals with discrete energies, again applying the concept of quantization, and de Broglie proposed his theory on wave-particle duality. These examples among others were unified by Heisenberg's matrix mechanics and Schrödinger's wave equation, which eventually led to the probabilistic nature of the now widely recognized Copenhagen interpretation. However, due to some of the extraordinary consequences of quantum mechanics, such as entanglement and correlations over a distance [1,2], the completeness of quantum mechanics was heavily debated, famously leading to heated discussions

between Einstein and Bohr [1,3]. In more recent times quantum mechanics has become one of the most effective models and continues to be used to explain and accurately predict the behavior of the world around us. While the development of quantum mechanics led to ground breaking understanding of the fundamental world, it was believed that only ensemble averages could be measured [4]. In a famous quote from 1952 Schrödinger said that experimenting with single particles is as likely as raising "Ichthyosuria*" in the zoo" [5]. In modern days, however, experiments controllably manipulate single isolated particles on a daily basis in laboratories around the world.

Possibly inspired by the developments of quantum mechanics, in 1982 Feynman argued that a computer based on "nature", and the intrinsic quantum mechanics therein, would be the best candidate to simulate nature itself [6]. Following this idea, concrete formulations of quantum computing and specific algorithms were developed [7–10]. Classical computers have completely digitalized parts of modern society since the invention of the transistor in 1947 [11, 12]. Predicted by Moore's law of exponential increase of transistors per unit area [13], computing power has continued to reach new heights. However, as transistors are reaching sizes limited by quantum effects, Moore's law is facing its end, and other approaches are required for a range of complicated simulation problems. For some of the problems still beyond our reach, a quantum computer holds the promise of exponential speed up [10]. The binary nature of the transistor is the foundation of the classical bit, which takes values of 0 or 1, and as a result, computing power scales linearly with the number of transistors. The quantum bit (qubit) is also built from a two-level system, a "quantum transistor", with two eigenstates $|0\rangle$ and $|1\rangle$. Compared to the classical bit, due to the nature of quantum mechanics, a qubit is not confined to only two possible values but rather the state $|\psi\rangle$ of the qubit, which can take any superposition of the two eigenstates, $|\psi\rangle = \alpha|0\rangle + \beta|1\rangle$, where α and β are the two probability amplitudes. Scaling to N entangled qubits allows computation with 2^N states leading to exponential speed up for certain applications, which take advantage of the parallel nature of quantum mechanics [10]. In order to build such a system, highly coherent and controllable qubits are required. This is inherently challenging as any coupling to the environment introduces potential coupling to noise sources. Therefore, one of the most promising paths to a fault tolerant quantum computer relies on quantum

*Ichthyosaurs are extinct marine reptiles.

error correction [10, 14, 15], where multiple faulty physical qubits are used to encode a single logical qubit with lower error rates [16].

Several qubit platforms have shown promising results in meeting the requirements for quantum computing and are being extensively researched, such as trapped ions [17, 18], electrons confined in quantum dots [19, 20], and photonic qubit [21, 22]. Superconducting circuits based on Josephson junctions are leading candidates, demonstrating impressive progress and many of the requirements as a potential architecture [23]. These circuits can be thought of as artificial atoms with energy spacings that are tunable by design. Distinguishable from a harmonic oscillator due to the crucial nonlinearity introduced by the Josephson junction, the two lowest energy levels can be isolated, manipulated and read out, effectively working as a two-level system. Since the first demonstrations of the Cooper pair box [24, 25] the field has seen significant developments [26]. These systems were later embedded in circuit quantum electrodynamics architectures [27, 28], the circuit variant of cavity quantum electrodynamics [29]. Moving to the so-called “transmon” regime [30–32] of large Josephson to charging energy ratio, along with continuous improvements in device processing and control, led to impressive progress. Coherence times of transmon qubits regularly reach several tens of microseconds with two-qubit gate fidelities exceeding 99 % [26], potentially above predicted error correction thresholds for certain geometries [33], and bosonic encoded qubits have demonstrated error corrected logical qubits [34, 35]. With the first demonstrations of quantum speed up [36] and cloud-based quantum processors [37], superconducting qubits are proving to be serious candidates for universal quantum computing. However, there is still a long way to, and challenges including (but not limited to) scaling, control and connectivity continue to pose difficult problems. Therefore, at the moment, it is too early to settle on a single qubit technology, which justifies the continued enthusiastic research into other potential qubit architectures.

The research in this thesis presents an alternative direction for superconducting qubits. Throughout the development of transmon qubit architectures, the Josephson junction has, almost without exception, been based on the insulating tunnel junction, built from a thin layer of aluminium oxide sandwiched between two aluminium electrodes. Due to the insulating nature of this junction, qubits fabricated in this way are either fixed in frequency or only tunable via a magnetic flux. Using magnetic flux pulses to change the qubit frequency

relies on current flowing which potentially introduces scaling problems due to the heat generated by this dissipative current. Recently semiconductor-junction based superconducting qubits (gatemon qubits) in nanowires [38, 39], and other material platforms [40–42] have been demonstrated. In gatemon qubits, the semiconducting junction results in a voltage tunable qubit frequency, removing the use of heat generating current. These new qubits, however, are not yet as mature as conventional transmons in terms of coherence times or device processing, but future improvements may see this type of qubit present a competitive alternative to the conventional transmon. Beyond acting as a gate tunable transmon, this new semiconducting-superconducting hybrid device is a very rich system, which can exhibit radically different qubit behavior. This new qubit behavior is the main focus of this thesis, involving variable transmission properties of the underlying Andreev physics, compatibility with DC transport techniques, and flux dependent coherent Andreev states. In addition, gatemon qubits are compatible with large magnetic fields and may therefore be used to study topological superconductivity [43, 44]. Developing topological materials that are inherently resilient to local noise mechanisms may be a natural direction to fault-tolerant quantum computing [45], reducing the number of error prone physical error corrected qubits required per logical qubit.

1.1 THESIS OUTLINE

This thesis reports research results on gatemon qubits based on proximitized nanowires. The thesis continues with an explanation of the basics of circuit quantum electrodynamics in Chapter 2, providing the reader with the necessary ingredients to understand the experiments described in later chapters. In addition, the specific theories investigated in the experimental chapters are discussed, focussing on the fundamental aspects of the semiconducting Josephson junctions and the consequences of these aspects. Chapter 3 details the device fabrication processes, the experimental setup, and measurement techniques applied in this work. This allows a reader to understand each experimental step from a blank wafer to the results presented in the experimental chapters. The following Chapters 4–8 present the experimental research results and intend to be self-contained with additional details on theory and experimental techniques available in Chapters 2 and 3. Chapter 4 is a systematic

study of gatemon qubit nonlinearity providing valuable information on the transmission distribution and the underlying physics of the semiconducting Josephson junctions. Chapter 5 present a scalable and deterministic approach to nanowire assembly of gatemon qubits. By integrating dielectrophoretic fabrication techniques to the qubit design, we demonstrate successful assembly of a six qubit device, where all qubits yield coherent operation. Chapter 6 demonstrates that gatemon qubits are compatible with DC transport. Here, a strong correlation between DC and qubit measurements is found. This motivates future studies applying both measurement techniques to probe underlying Josephson physics. In addition, the results suggest that this new qubit design does not introduce new relaxation sources. Chapter 7 reports the observation of enhanced suppression of charge dispersion of the superconducting island, which is explained by transmission probabilities of the Andreev processes across the Josephson junction reaching values near unity. This nearly perfect transmission is explained by a resonant level inside the Josephson junction with approximately symmetric barriers. These results establish an experimental validation of the theory of Coulomb oscillations in Josephson junctions in a previously unexplored regime. Chapter 8 presents the final experimental results, where the emergence of a unique subgap spectrum due to an applied magnetic flux is observed. This opens new directions for Andreev qubit research due to the fundamentally different energy spectra. Finally, an outlook is given in Chapter 9. Together this presents a comprehensive investigation into the fundamental aspects of a promising qubit architecture which hopefully will provide a strong foundation for further developments in this exciting field.

2

Circuit Quantum Electrodynamics

Cavity quantum electrodynamics (cavity QED) describes the field of atoms coupled to modes of light, and has a rich history of exploring the fundamental laws of quantum mechanics [29]. Placing atoms in cavities with highly reflective mirrors opened the possibility of coherent experiments at the single atom level. In close resemblance to cavity QED, circuit quantum electrodynamics (cQED) describes the dynamics of artificial atoms coupled to electromagnetic photon modes. These photon modes are usually standing waves in one-dimensional harmonic resonators [28] or the modes of three-dimensional cavities [46]. When superconducting artificial atoms based on anharmonic oscillators are coupled to these modes it is possible to create highly coherent, isolated, and detectable quantum states, the foundation of superconducting qubits.

This chapter presents a simple overview of the basic concepts of cQED, required to understand the measurements presented in Chapters 4–8. First, the superconducting *LC* oscillator is described, which is followed by a discussion on Josephson junction-based anharmonic oscillators and transmon qubits, mainly focussing on the fundamental consequences of building the junction with a semiconductor. Hereafter, the basic concepts of qubit readout and manipulation are discussed. The last section discusses the prospect of combining hybrid transmon qubits and topological superconductivity.

2.1 THE LC OSCILLATOR

Superconductivity is a fascinating phenomenon, where otherwise repulsive electrons partner up in so-called Cooper pairs [47], forming a resistance-less condensate [48, 49]. Due to its remarkable electric properties, superconductivity has been an ongoing research field, since its discovery in 1911 [50], and presents an exciting platform for many applications. One such application is superconducting quantum circuits, described by the degrees of freedom associated with the specific circuit elements. One of the simplest superconducting circuits to consider is the *LC* oscillator consisting of an inductor and a capacitor. The dynamics of this superconducting circuit can be well described by one degree of freedom [51], the dissipationless current flow. Applying the lumped element approximation provides intuition of typical cQED experiments. In this limit, we treat the inductor and capacitor as discrete elements with inductance L and capacitance C , respectively, as sketched in Fig. 2.1(a). The kinetic energy associated with the current flow I through the inductor is given by $LI^2/2 = L\dot{q}^2/2$, where \dot{q} is the time derivative of the charge of one of the capacitor plates q . Similarly, the potential energy associated with charging up the capacitor is given by $\frac{q^2}{2C}$. This allows us to write the Lagrangian,

$$\mathcal{L} = \frac{1}{2}L\dot{q}^2 - \frac{1}{2C}q^2, \quad (2.1)$$

from which the conjugate momentum is derived,

$$\frac{\partial \mathcal{L}}{\partial \dot{q}} = L\dot{q} = LI = \Phi,$$

where Φ is the flux through the inductor. This results in the Hamiltonian,

$$H = \Phi\dot{q} - \mathcal{L} = \frac{\Phi^2}{2L} + \frac{q^2}{2C}, \quad (2.2)$$

which describes a harmonic oscillator with mass L and spring constant $1/C$. We identify the resonance frequency $\omega = 1/\sqrt{LC}$. To treat the system quantum mechanically, we promote the coordinate and conjugate momentum to quantum operators \hat{q} and $\hat{\Phi}$, defined to satisfy the canonical commutation

relation,

$$[\hat{q}, \hat{\Phi}] = i\hbar, \quad (2.3)$$

where \hbar is reduced Planck's constant. By doing so and rewriting Hamiltonian in terms of the cooper pair number operator $\hat{n} = \hat{q}/(-2e)$, and the phase operator $\hat{\phi} = 2\pi\hat{\Phi}/\Phi_0$, where $\Phi_0 = h/(2e)$ is the flux quantum, and e is the electron charge, we obtain,

$$H = \frac{\hat{q}^2}{2C} + \frac{\hat{\Phi}^2}{2L} = 4E_C\hat{n} + \frac{E_L}{2}\hat{\phi}, \quad (2.4)$$

where $E_C = e^2/(2C)$ and $E_L = (\Phi_0/2\pi)^2/L$ is the characteristic inductive energy. This allows rewriting the plasma frequency $\omega = 1/\sqrt{LC} = \sqrt{8E_CE_L}/\hbar$. As always with harmonic oscillators, we can define the raising and lowering operators based on the conjugate variables,

$$\begin{aligned} \hat{a} &= i\frac{1}{\sqrt{2L\hbar\omega}}\hat{\Phi} + \frac{1}{\sqrt{2C\hbar\omega}}\hat{q} \\ \hat{a}^\dagger &= -i\frac{1}{\sqrt{2L\hbar\omega}}\hat{\Phi} + \frac{1}{\sqrt{2C\hbar\omega}}\hat{q}, \end{aligned} \quad (2.5)$$

obeying $[\hat{a}, \hat{a}^\dagger] = 1$. By definition the Hamiltonian can be written,

$$H = \hbar\omega(\hat{a}^\dagger\hat{a} + 1/2). \quad (2.6)$$

As we shall see in Chapters 4 and 7 it is often convenient to operate with the flux as the coordinate, when describing systems involving Josephson junctions. For the derivation of Eq. (2.4), we could have chosen Φ as our coordinate and q as conjugate momentum. In this definition Φ correspond to the flux node, which is the connecting branch between the two lumped elements given by the time integral of the voltage,

$$\begin{aligned} \Phi &= \int^t V(t')dt' \\ V(t) &= \dot{\Phi}. \end{aligned} \quad (2.7)$$

This would of course have led to the same Hamiltonian, but in this case we

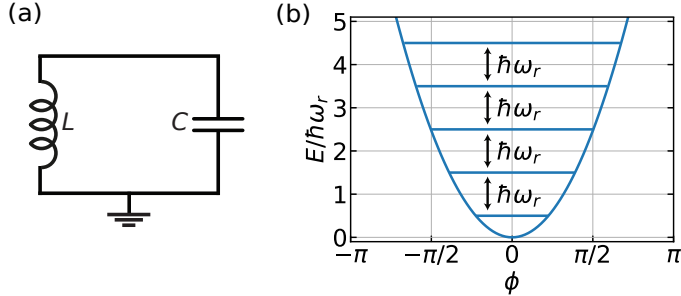


Figure 2.1: LC circuit sketch and potential. (a) Sketch of the circuit of an inductor with inductance L in parallel with a capacitor with capacitance C . (b) Harmonic potential of the LC oscillator and corresponding energy levels and transition energies indicated (arrows). The energy scale is normalized to the harmonic transition energy $\hbar\omega_r = \hbar/\sqrt{LC}$.

would write the energy stored in the inductor as $\Phi^2/2L$, which now acts as potential energy. Similarly, the energy stored in the capacitor is given by $CV^2/2$, where V is the voltage difference across the capacitor. This allows writing the energy associated with the capacitor as $C\dot{\Phi}^2/2$, which takes the form of kinetic energy*, resulting in the Lagrangian,

$$\mathcal{L} = \frac{C}{2}\dot{\Phi}^2 - \frac{1}{2L}\Phi^2, \quad (2.8)$$

again leading to Eq. (2.4),

$$H = \frac{\hat{q}^2}{2C} + \frac{\hat{\Phi}^2}{2L} = 4E_C\hat{n} + \frac{E_L}{2}\hat{\phi}. \quad (2.9)$$

Figure 2.1(b) shows the solutions to Eq. (2.9). With phase as the coordinate, the commutator relation now yields,

$$[\hat{\Phi}, \hat{q}] = i\hbar, \quad (2.10)$$

which has the opposite sign as Eq. (2.3). This means that when choosing Φ as coordinate the charge is defined with opposite sign. As before, we can define raising and lowering. Based on the new choice of conjugate variables, C acting

*With Φ as coordinate, Φ plays the role of the velocity in a mechanical spring system.

as the particle mass and with $1/L$ as spring constant, they are defined,

$$\begin{aligned}\hat{a} &= i \frac{1}{\sqrt{2C\hbar\omega}} \hat{q} + \frac{1}{\sqrt{2L\hbar\omega}} \hat{\Phi} \\ \hat{a}^\dagger &= -i \frac{1}{\sqrt{2C\hbar\omega}} \hat{q} + \frac{1}{\sqrt{2L\hbar\omega}} \hat{\Phi}.\end{aligned}\quad (2.11)$$

These definitions will be useful when studying qubit anharmonicity in Chapter 4.

As we shall see later, *LC* oscillators play a crucial role in cQED acting as the readout resonators for superconducting qubits analogues to cavities in cavity QED. So far we have treated the inductor and capacitor as discrete elements, which allowed deriving its Hamiltonian. However, for all the work presented in this thesis, the readout resonators are distributed elements in the form of coplanar waveguides (CPWs). The resonators are described by a capacitance c and an inductance l per unit length, and are created by boundary conditions introduced as breaks and shorts in transmission lines. Due to the finite length, standing waves will form. These standing waves can be treated as independent harmonic oscillators [51], each with different resonance frequency $\omega_n = v_p/\lambda_n$, where the mode wave velocity $v_p = 1/\sqrt{lc}$ and λ_n is the wavelength of the n th resonator mode. The wavelengths λ_n will depend on the specific boundary conditions of the CPW. For all experiments presented in the thesis, the resonators (see Chapter 3 for additional details) are fabricated with a break in one end and a short in the opposite end, which leads to a voltage anti-node and a voltage node in each end, respectively. For a resonator of length L , the wavelengths are given by $\lambda_n = 4L/(2n + 1)$. Due to $L = \lambda_0/4$ the resonators are often termed $\lambda/4$ resonators. The resulting frequencies are given by $\omega_n = v_p(2n + 1)/4L = \omega_0(2n + 1)$, where ω_0 is the frequency of the 0th mode. As ω_0 is 3 times lower than the frequency of the next mode the higher modes of the resonators can often be ignored, treating the resonator as a single harmonic oscillator, which we do throughout this thesis.

The readout cavities can also be constructed from $\lambda/2$ resonators, where both ends of the CPW have a break and thereby a voltage anti-node, yielding $\lambda_n = 2L/n$ and $\omega_n = nv_p/L = n\omega_0$. As for the $\lambda/4$ resonator, the next mode is much higher in frequency and for most practical purposes it can be viewed as a single harmonic oscillator.

2.2 ANHARMONIC OSCILLATORS

Superconducting harmonic *LC* oscillators are interesting and well-described systems. However, if we are interested in creating a system that can be used as a qubit, harmonic oscillators are not applicable[†], as the energy levels are equally spaced. Therefore, individual energy transitions cannot be addressed required for qubit operations. Instead, constructing a system with nonlinearly spaced energy levels, the two lower levels can be used as the qubit system. In the context of superconducting qubits, Josephson junctions (JJs) [54] provide the required nonlinearity and, crucially, they are also non-dissipative.

A Josephson junction is created by separating two superconducting electrodes with a non-superconducting material. In principle the junction can be created from any material. However, a very common type of junction is the superconductor-insulator-superconductor (SIS) JJ, which almost all conventional superconducting qubits devices are based on [55]. It is well described by a sinusoidal current phase relation (CPR) [56],

$$I_s = I_c \sin \phi, \quad (2.12)$$

where I_s denotes the supercurrent, ϕ denotes the superconducting phase difference across the JJ, and I_c is the critical current, i.e the largest current the system can sustain before turning non-superconducting. This effect is known as the DC Josephson effect [49] and describes how the flow of current across the JJ is modified by ϕ .

If a voltage difference V is provided across the junction the phase difference will evolve by,

$$\frac{d\phi}{dt} = \frac{2eV}{\hbar}. \quad (2.13)$$

This effect is known as the AC Josephson effect [49]. Evaluating the time derivative of I_s and by applying Eq. (2.13), we obtain,

$$\frac{dI_s}{dt} = \frac{d}{dt} I_c \sin(\phi) = I_c \cos(\phi) \frac{d\phi}{dt} = I_c \cos(\phi) \frac{2eV}{\hbar}. \quad (2.14)$$

[†]This is not fully accurate as bosonic qubits encode the information in the harmonic oscillator states of resonators [52, 53]. The resonators are then coupled to transmons to provide the nonlinearity.

By identifying that $\frac{dI_s}{dt}$ takes the same form as the current-voltage (I - V) relation of an inductor with inductance L ,

$$V = -L \frac{dI}{dt}, \quad (2.15)$$

the Josephson junction is often referred to as a nonlinear inductor with inductance,

$$L_J = \frac{\hbar}{2eI_c \cos(\phi)}. \quad (2.16)$$

By observing that L_J depends on the applied current (via the dependence on ϕ), it is clear why a JJ can be thought of as a nonlinear inductor.

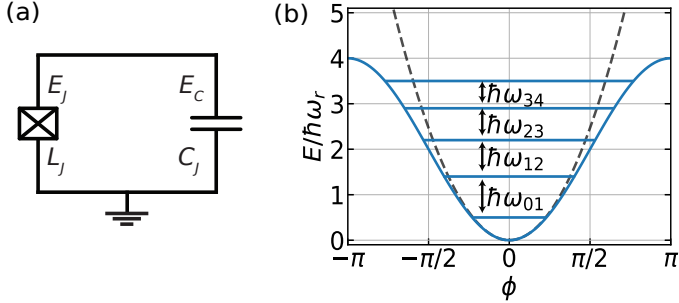


Figure 2.2: Josephson circuit sketch and potential. (a) Sketch of the circuit of a Josephson junction with Josephson tunneling energy E_J in parallel with a capacitor with capacitance C_J . (b) Potential of a insulator-based junction ($\cos(\phi)$ -potential, blue) and corresponding energy levels and transition energies indicated (arrows). The harmonic potential is also plotted (dashed line) to illustrate the difference between the potentials. The energy scale is normalized to the harmonic transition energy $\hbar\omega_r = \hbar/\sqrt{L_J C_J} = \sqrt{8E_J E_C}$.

Josephson junctions are often modeled as an ideal junction in parallel with a capacitance [51]. This circuit is almost an LC circuit, where the Josephson junction has substituted the inductor, see Fig 2.2(a). As with the LC oscillator, this circuit is described by two degrees of freedom associated to two energy scales, the charging energy of the capacitor $E_C = \frac{e^2}{2C_J}$, and the energy associated with the current flow across the JJ. This tunneling energy $E(\phi)$ can be calculated by combining Eqs. (2.12) and (2.13), and by evaluating the time integral of the

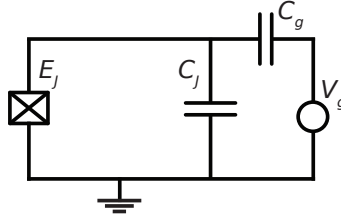


Figure 2.3: Circuit sketch of the anharmonic oscillator coupled to a voltage gate V_g via a capacitance C_g .

power $P = I_s V$,

$$\begin{aligned} E(\phi) &= \int_0^t P dt' = \int_0^t I_s V dt' = \int_0^t I_s \frac{\hbar}{2e} \frac{d\phi}{dt'} dt' = \\ &\int_0^\phi I_c \sin(\phi') \frac{\hbar}{2e} d\phi' = -\frac{\hbar}{2e} \cos(\phi) = -E_J \cos(\phi), \end{aligned} \quad (2.17)$$

where $E_J = \hbar I_c / 2e$ is the characteristic Josephson tunneling energy. Again treating the charging energy term as the kinetic energy, and the Josephson (“inductanc”) energy term as the potential energy, we can write the Lagrangian,

$$\mathcal{L} = \frac{C_J}{2} \dot{\Phi}^2 + E_J \cos\left(2\pi \frac{\Phi}{\Phi_0}\right), \quad (2.18)$$

which results in the Hamiltonian,

$$H = 4E_C \hat{n}^2 - E_J \cos(\hat{\phi}), \quad (2.19)$$

where the potential is plotted in Fig. 2.2(b).

For this system, the energy depends on the offset charge n_g due to the discrete flow of charge across the junction (integer numbers of Cooper pairs). This offset is usually controlled with a gate V_g [Fig. 2.3], and the resulting Hamiltonian is given,

$$H = 4E_C(\hat{n} - n_g)^2 - E_J \cos(\hat{\phi}). \quad (2.20)$$

This Hamiltonian was originally used to describe charge qubits and the Cooper

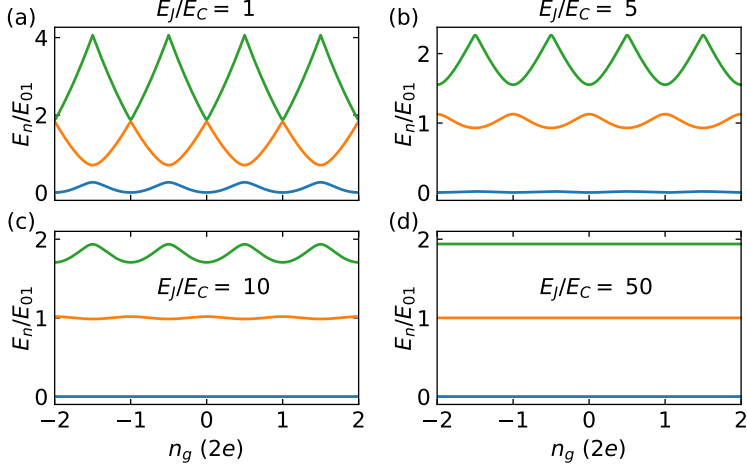


Figure 2.4: Numerical solutions to transmon Hamiltonian. Numerical solutions to Eq. (2.20) for four different E_J/E_C showing the three lowest energy levels, E_0 , E_1 , E_2 (blue, orange, green) as a function of offset charge n_g . As the ratio E_J/E_C is increased in (a)–(d), the charge dispersion, defined as the amplitude of the charge fluctuations in E_n , is substantially reduced. This figure is inspired by Ref. [30]. Energies E_n are normalized to $E_{01}(n_g = 0.25) = E_1(n_g = 0.25) - E_0(n_g = 0.25)$ as opposed to the more commonly chosen $E_{01}(n_g = 0.5)$, which is convenient for the analysis in Chapter 7.

pair box (CPB) qubit [24, 25], and can be solved numerically in the charge basis, described by the charge eigenstates $|n\rangle$. In this basis $\hat{n}|n\rangle = n|n\rangle$, where n is the number of Cooper pairs on the island, and $\cos\hat{\phi} = 1/2 \sum (|n\rangle\langle n+1| + |n+1\rangle\langle n|)$ [51]. Numerical solutions to Eq. (2.20) are shown in Fig. 2.4 for different ratios of E_J/E_C . In order to calculate these solutions the Hamiltonian is written with matrix formalism in a truncated charge space^f. The CPB qubit was originally operated in the $E_J/E_C \lesssim 1$. As seen from Fig. 2.4 the qubit transition energy $E_{01}(n_g) = E_1(n_g) - E_0(n_g)$ has a strong dependence on n_g , leaving the CPB susceptible to charge noise limiting coherence times [57]. By operating the CPB qubit at the sweet spot $n_g = 1/2$, the system is insensitive to charge fluctuations to first order due to $\partial E/\partial n_g = 0$. Despite operating the CPB at the sweet spot the coherence times are still lim-

^fNumerical code to solve the transmon Hamiltonian are found at:
<https://github.com/anderskringhoej/Dispersion>.

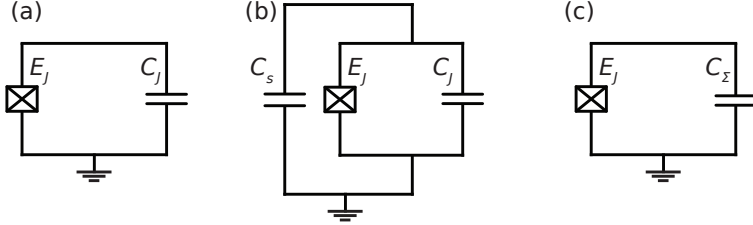


Figure 2.5: Cooper pair box and transmon circuit sketch. (a) Circuit sketch of a single junction in parallel with the junction capacitance C_J . By shunting the circuit with a capacitor C_s the circuit in (b) is realised, which effectively is equivalent to the circuit in (c) with charging energy $E_C = e^2/(2C_\Sigma)$ set by the sum of capacitances $C_\Sigma = C_J + C_s$.

ited by the charge fluctuations. Instead, as originally proposed by Ref. [30], by increasing the ratio E_J/E_C the charge dispersion (the amplitude of the fluctuations in n_g of the energy levels E_n) is exponentially suppressed, as seen from Fig. 2.4. The increase of E_J/E_C is commonly achieved experimentally by shunting the junction with a large capacitor, see Fig. 2.5. In this case the charging energy is now set by the sum of capacitances $E_C = e^2/2(C_J + C_s) = e^2/(2C_\Sigma)$, where C_s is the capacitance of the shunt capacitor. The circuit is still equivalent to a single junction and capacitor in parallel, now with the capacitance given by C_Σ (Fig. 2.5), and thereby still described Eq. (2.20). As C_s is typically much larger than C_J , E_C is effectively set by C_s .

As observed from Fig. 2.4 the anharmonicity, defined as the difference between the two lowest transition energies $\alpha = E_{12} - E_{01}$, is also decreasing as E_J/E_C is increased. However, as α only decrease with a power law [30], it is beneficial to move to the $E_J/E_C \gtrsim 50$ regime. By doing so coherence was drastically increased [58], and impressive improvements has been achieved since [26].

A simple and intuitive way of understanding the suppression of the charge dispersion as E_J/E_C is increased, is to think of the transmon circuit as a rotor with a mass m attached to a rod of length l [30]. In this analogy $E_J \rightarrow mgl$, and $E_C \rightarrow \hbar^2/(8ml^2)$, where g is the gravitational acceleration. Identifying the $E_J/E_C \gg 1$ regime as the regime, where the quantum rotor is experiencing a large gravitational force, the resulting oscillations around $\phi = 0$ are small. We can apply this classical intuition to obtain some understanding of the quantum phase fluctuations of the Josephson phase particle. As phase is

getting localized (smaller quantum fluctuations) it naturally means that the charge, the conjugate coordinate of phase, is getting delocalized. As charge is no longer well defined a gate voltage cannot change the energy of the island. This mechanism results in the decaying charge dispersion amplitudes as E_J/E_C is increased.

Qubit anharmonicity is a crucial parameter determining the maximum speed of qubit operations. This is due to leakage out of the computational space due to overlap with $1 \rightarrow 2$ transition and repulsion between the excited states as the drive is applied [59]. To understand how qubit anharmonicity depends on E_J/E_C , we expand the potential of Eq. (2.20) around $\phi = 0$, valid in the $E_J/E_C \gg 1$ regime,

$$E_J \cos \hat{\phi} = E_J - \frac{E_J}{2} \hat{\phi}^2 + \frac{E_J}{24} \hat{\phi}^4 + O(\hat{\phi}^6). \quad (2.21)$$

If we insert Eq. (2.21) to Eq. (2.19) and omit constant terms we obtain to 4th order,

$$H = 4E_C \hat{n}^2 - E_J \cos \hat{\phi} \approx 4E_C \hat{n}^2 + \frac{E_J}{2} \hat{\phi}^2 - \frac{E_J}{24} \hat{\phi}^4 = H_0 + V'(\hat{\phi}), \quad (2.22)$$

where $H_0 = 4E_C \hat{n}^2 + E_J \hat{\phi}^2/2$ is the Hamiltonian of a harmonic oscillator [see Eq. (2.4)] with plasma frequency $\omega = 1/\sqrt{L_J C} = \sqrt{8E_C E_J}/\hbar$. Treating $V'(\hat{\phi}) = -E_J \hat{\phi}^4/24$ as a perturbation to H_0 allows us to calculate the corrections to the harmonic transition energies. Evaluating the perturbation matrix elements $\langle i | V'(\hat{\phi}) | i \rangle$ for $i = 0, 1, 2$ allows deriving the anharmonicity. This is easiest achieved by expressing \hat{n} and $\hat{\phi}$ in terms of raising and lowering operators \hat{a}^\dagger and \hat{a} ,

$$\begin{aligned} \hat{a} &= 2i\sqrt{\frac{E_C}{\hbar\omega}} \hat{n} + \sqrt{\frac{E_J}{2\hbar\omega}} \hat{\phi} \\ \hat{a}^\dagger &= -2i\sqrt{\frac{E_C}{\hbar\omega}} \hat{n} + \sqrt{\frac{E_J}{2\hbar\omega}} \hat{\phi}. \end{aligned} \quad (2.23)$$

These are the conventional raising and lowering operators of the LC oscillator derived in Eq. (2.11), rewritten in terms of E_C , E_J , \hat{n} , and $\hat{\phi}$ by using $E_C = e^2/2C$, $E_J = (\Phi_0/2\pi)^2/L_J$ (true to lowest order in $\hat{\phi}$), $\hat{q} = -2e\hat{n}$, and $\hat{\phi} = 2\pi\hat{\Phi}/\Phi_0$.

From here we obtain,

$$\begin{aligned}\hat{n} &= \frac{-i}{4} \sqrt{\frac{\hbar\omega}{E_C}} (\hat{a} - \hat{a}^\dagger) = \frac{-i}{2} \left(\frac{E_J}{2E_C} \right)^{1/4} (\hat{a} - \hat{a}^\dagger). \\ \hat{\phi} &= \sqrt{\frac{\hbar\omega}{2E_J}} (\hat{a} + \hat{a}^\dagger) = \left(\frac{2E_C}{E_J} \right)^{1/4} (\hat{a} + \hat{a}^\dagger).\end{aligned}\quad (2.24)$$

Inserting into \hat{H}_0 and $V'(\hat{\phi})$ yields,

$$\hat{H}_0 = \hbar\omega (\hat{a}^\dagger \hat{a} + 1/2), \quad (2.25)$$

by definition, and

$$V'(\hat{\phi}) = -E_J \frac{\hat{\phi}^4}{24} = -\frac{E_C}{12} (\hat{a} + \hat{a}^\dagger)^4. \quad (2.26)$$

Applying the rotating wave approximation, i.e. neglecting terms with different number of raising and lowering operators yields,

$$V'(\hat{\phi}) \approx -\frac{E_C}{2} (\hat{a}^\dagger \hat{a}^\dagger \hat{a} \hat{a} + 2\hat{a}^\dagger \hat{a}). \quad (2.27)$$

We are now ready to evaluate the perturbation matrix elements $\langle i | V'(\hat{\phi}) | i \rangle$ for $i = 0, 1, 2$,

$$\begin{aligned}\langle 0 | V'(\hat{\phi}) | 0 \rangle &= 0 \\ \langle 1 | V'(\hat{\phi}) | 1 \rangle &= -E_C \\ \langle 2 | V'(\hat{\phi}) | 2 \rangle &= -3E_C.\end{aligned}\quad (2.28)$$

This allows calculating the corrections to the two lower transition energies,

$$\begin{aligned}E_{01} &\approx E_1 - E_0 = \sqrt{8E_C E_J} - E_C \\ E_{12} &\approx E_2 - E_1 = \sqrt{8E_C E_J} - 2E_C,\end{aligned}\quad (2.29)$$

yielding the anharmonicity,

$$E_{12} - E_{01} = \alpha \approx -E_C. \quad (2.30)$$

This result illustrates that by moving to the transmon regime, the anharmonicity stays sufficiently large for fast operations while eliminating the charge noise sources by suppressing charge dispersion. For these reasons transmon qubits are usually designed with $E_J/E_C \sim 50$. In practice, qubits are typically operated frequencies $f_{01} \sim 5$ GHz with $E_C = 200\text{--}300$ MHz due to practical considerations such as qubit frequency exceeding the thermal energy, shielding, and common bandwidth of electronic equipment.

2.3 SEMICONDUCTOR-BASED SUPERCONDUCTING QUBITS

Semiconductor-based Josephson junctions have been the key element for the research of this thesis. Recently transmon qubits based on semiconducting junctions has been demonstrated [38, 39]. When substituting the SIS junction with a superconductor-semiconductor-superconductor (S-Sm-S) junction, the carrier density in the junction is gate tunable. As a result the critical current and thereby the qubit frequency is gate tunable. This is in contrast to transmon qubits, where the qubit frequency is either fixed or flux tunable. Except tuning the qubit frequency with gate voltages, the gatemon is otherwise operated as a transmon. Therefore, it is tempting to think of the gatemon as nothing but a gateable transmon qubit. And for some applications this is also true. For instance, in the context of scaling up transmon qubits towards successful quantum error correction schemes [14, 15, 60]. Gatemon qubits would in principle apply equally well as transmon qubits with the potential advantage of not having to worry about large currents running in the cryostat for flux tuning. However, for this to be interesting, gatemon qubits would have to demonstrate the same impressive developments in terms of performance, gate fidelity, and hardware control that has made transmon qubits a leading candidate for universal quantum computing [26, 36]. Although nanowire-based gatemon qubits have shown a promising improvements in coherence [61, 62] since the first realisations [38, 39], the qubits have not consistently proved the same impressive values of coherence times as transmon qubits. Additionally, scaling perspectives of individually placed nanowires does not seem promising. However, promising results on other material platforms as two-dimensional electron gas (2DEG), where gatemon qubits have already been demonstrated [40], or selective area growth [63], where the entire circuit are deterministically defined, suggest that scaling of these qubits

is equally possibly to other lithographically defined qubits. These platforms are, however, currently limited by intrinsic loss mechanisms of the substrates, typically III-IV materials. However, if these platforms are integrated with low loss substrates, there is no reason why gatemon qubits cannot be a serious alternative to transmon qubits.

The main activity of the research of this thesis has been investigating fundamental aspects of the gatemon qubit and the semiconducting Josephson junction, and as a result it is clear that on some key aspects a gatemon fundamentally differs from a transmon. To explain some of these differences of the S-Sm-S junction it is no longer sufficient to consider the sinusoidal CPR of Eq. (2.12), which leads to the sinusoidal energy phase relation $E_J \cos(\phi)$. Instead, we consider a more general model based on the specific distribution of the Andreev modes responsible for Cooper pair transport across the junction. These processes are known as Andreev reflections [64], where electrons are reflected as holes at the junction boundaries generating Cooper pairs in the superconductor. In short junction limit $L \ll \xi$, where L is the junction width and ξ is coherence length of the junction, multiple Andreev reflections result in a pair of Andreev bound states. Each pair has the ground and excited state energies $\pm\Delta\sqrt{1 - T_i \sin^2(\hat{\phi}/2)}$, where Δ is the superconducting gap and T_i is the transmission probability of the Andreev mode. In the case of well-separated ground and excited state energies, summing over all ground state energies yields the Josephson potential,

$$V(\hat{\phi}) = -\Delta \sum_i \sqrt{1 - T_i \sin^2(\hat{\phi}/2)}. \quad (2.31)$$

Neglecting the offset charge, the general gatemon Hamiltonian is given by

$$\hat{H} = 4E_C \hat{n}^2 + V(\hat{\phi}). \quad (2.32)$$

Figure 2.6 shows the potential of Eq. (2.31) in the two limits of $T_i \rightarrow 0$ and T_i compared to the harmonic potential V_{HO} . It is observed that for increasing T_i the potential of Eq. (2.31) is in closer resemblance of V_{HO} . As a consequence it is expected that the anharmonicity is transmission-dependent. To understand this theoretically, we follow the procedure of Section 2.2, where $V(\hat{\phi})$ is

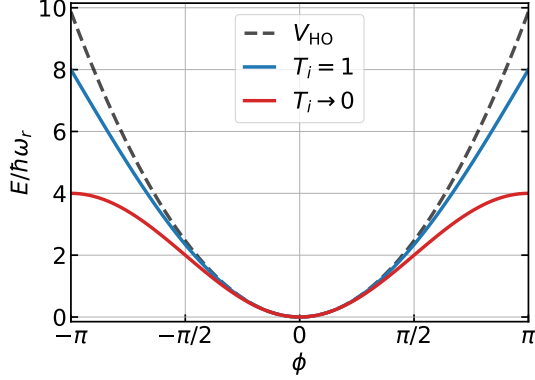


Figure 2.6: Short junction Josephson potential. The potential of Eq. (2.31) as a function of ϕ in the two limits of transmission T_i (red and blue lines). The potentials are normalized to the harmonic resonance frequency ω_r and offset to all equal 0 at $\phi = 0$. A closer resemblance to the harmonic potential V_{HO} (dashed line) is observed as T_i is increased.

expanded to 4th order in $\hat{\phi}$,

$$\begin{aligned}
 V(\hat{\phi}) &\approx \Delta \sum_i \left(\frac{T_i}{8} \hat{\phi}^2 - \left(\frac{T_i^2}{128} - \frac{T_i}{96} \right) \hat{\phi}^4 \right) \\
 &= \frac{\Delta}{4} \sum_i \left(\frac{T_i}{2} \hat{\phi}^2 - \frac{T_i}{24} \left(1 - \frac{3}{4} T_i \right) \hat{\phi}^4 \right) \\
 &= E_J \frac{\hat{\phi}^2}{2} - E_J \left(1 - \frac{3 \sum T_i^2}{4 \sum T_i} \right) \frac{\hat{\phi}^4}{24}, \tag{2.33}
 \end{aligned}$$

where the constant term is omitted and $E_J = \frac{\Delta}{4} \sum T_i$. This expansion is valid for $E_J/E_C \gg 1$, where $\phi \approx 0$. Again, the $\hat{\phi}^2$ -term has the same form as the harmonic potential $V_0(\hat{\phi}) = E_J \frac{\hat{\phi}^2}{2}$. Treating $V'(\hat{\phi}) = -E_J \left(1 - \frac{3 \sum T_i^2}{4 \sum T_i} \right) \frac{\hat{\phi}^4}{24}$ as a perturbation to \hat{H}_0 and evaluating the perturbation matrix elements $\langle i | V'(\hat{\phi}) | i \rangle$ for $i = 0, 1, 2$ allow us to calculate the anharmonicity. By inserting \hat{n} and $\hat{\phi}$

[Eq. (2.24) into $V'(\hat{\phi})$] we obtain,

$$V'(\hat{\phi}) = -E_J \left(1 - \frac{3 \sum T_i^2}{4 \sum T_i}\right) \frac{\hat{\phi}^4}{24} = -\frac{E_C}{12} \left(1 - \frac{3 \sum T_i^2}{4 \sum T_i}\right) (\hat{a} + \hat{a}^\dagger)^4. \quad (2.34)$$

Evaluating the perturbation matrix elements $\langle i | V'(\hat{\phi}) | i \rangle$ for $i = 0, 1, 2$ yields,

$$\begin{aligned} \langle 0 | V'(\hat{\phi}) | 0 \rangle &= 0 \\ \langle 1 | V'(\hat{\phi}) | 1 \rangle &= -E_C \left(1 - \frac{3 \sum T_i^2}{4 \sum T_i}\right) \\ \langle 2 | V'(\hat{\phi}) | 2 \rangle &= -3E_C \left(1 - \frac{3 \sum T_i^2}{4 \sum T_i}\right). \end{aligned} \quad (2.35)$$

(2.36)

The resulting corrections to the two lower transition energies are given by,

$$\begin{aligned} E_{01} &= E_1 - E_0 = \sqrt{8E_C E_J} - E_C \left(1 - \frac{3 \sum T_i^2}{4 \sum T_i}\right) \\ E_{12} &= E_2 - E_1 = \sqrt{8E_C E_J} - 2E_C \left(1 - \frac{3 \sum T_i^2}{4 \sum T_i}\right), \end{aligned} \quad (2.37)$$

yielding the anharmonicity,

$$E_{12} - E_{01} = \alpha \approx -E_C \left(1 - \frac{3 \sum T_i^2}{4 \sum T_i}\right). \quad (2.38)$$

It is noted that in the limit of $T_i \rightarrow 0$ the conventional transmon result is obtained, $\alpha = -E_C$. This is expected as the $\cos(\phi)$ potential is the special case of $V(\hat{\phi}) = -\Delta \sum_i \sqrt{1 - T_i \sin^2(\hat{\phi}/2)}$ for $T_i \rightarrow 0$. This is immediately obvious if

we expand $V(\hat{\phi})$ around $T_i = 0$,

$$\begin{aligned} V(\hat{\phi}) &= -\Delta \sum_i \sqrt{1 - T_i \sin^2(\hat{\phi}/2)} \approx -\Delta \sum_i \left(1 - \frac{T_i \sin^2(\hat{\phi}/2)}{2}\right) \\ &= -\Delta \sum_i \left(1 - \frac{1 - T_i \cos(\hat{\phi})}{4}\right) = -\frac{\Delta}{4} \sum_i T_i \cos(\hat{\phi}) + \text{const.}, \end{aligned} \quad (2.39)$$

using $\sin(x/2) = 1 - \cos(x)$. Ignoring the remaining constant term and identifying $E_J = \frac{\Delta}{4} \sum_i T_i$, we obtain,

$$V(\hat{\phi}) \approx -E_J \cos(\hat{\phi}). \quad (2.40)$$

The gatemon anharmonicity is experimentally studied in great detail in Chapter 4, where it is concluded that the nanowire-based semiconducting junction of a gatemon is dominated by 1–3 transmitting modes with one mode exceeding $T_i = 0.9$ for certain values of gate voltage.

We have seen that a simple expansion valid in the $E_J/E_C \gg 1$ regime yields key information about the properties of Josephson junctions and qubit anharmonicity. To extend this analysis, we consider a Josephson junction with a single channel with transmission T , still applying the short junction limit. The Hamiltonian of this system is given by,

$$\hat{H} = 4E_C \left(i\partial_{\hat{\phi}} - n_g\right)^2 + \hat{H}_J, \quad (2.41a)$$

$$\hat{H}_J = \tilde{\Delta} \begin{bmatrix} \cos(\hat{\phi}/2) & r \sin(\hat{\phi}/2) \\ r \sin(\hat{\phi}/2) & -\cos(\hat{\phi}/2) \end{bmatrix}, \quad (2.41b)$$

where $r = \sqrt{1 - T}$ is the reflection amplitude. This Hamiltonian was originally derived for a superconducting quantum point contact and is valid provided $E_C \ll \Delta$ and that the Andreev states are separated from the continuum [65]. The requirement of separated states from the continuum is less import in the case of no direct phase biasing, and provides information of the charge dispersion. The eigenvalues E of H_J are the bound state energies,

$$E = \pm\Delta \sum_i \sqrt{1 - T \sin^2(\phi/2)}, \quad (2.42)$$

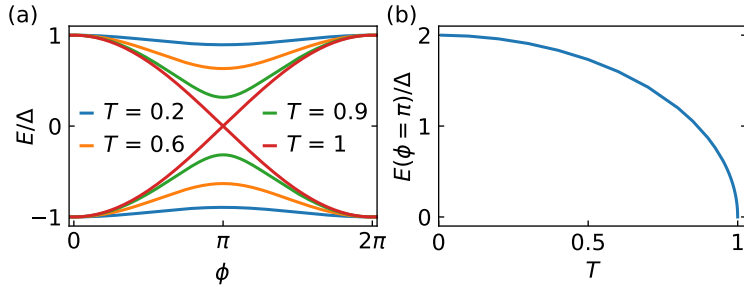


Figure 2.7: Andreev eigenenergies and energy gap at $\phi = \pi$. (a) Eigenenergies $E = \pm\Delta\sqrt{1 - T\sin^2(\phi/2)}$ of H_J as a function of phase ϕ for increasing transmission T (blue to red). It is observed that the two energy branches become less separated for increasing T until the avoided crossing is suppressed at $T = 1$. This illustrates the transition from the adiabatic limit, where the phase particle are always in the ground state, to the opposite diabatic limit. (b) The energy $E(\phi = \pi)$ as a function of T illustrating the decrease in the separation of the energy branches for increasing T .

which are shown in Fig. 2.7(a). This Hamiltonian differs slightly from Eq. (2.32), where we sum over ground state energies. In general summing over quasi-particle ground state energies to obtain the potential is only valid when the ground state energy is well separated from the excited energy branch. For $r \sim (E_C/\Delta)^{1/2}$ the assumption of well separated bound state energy branches is no longer valid as Landau-Zener transitions connect the branches. The Landau-Zener transitions are captured by Eq. (2.41) and not by Eq. (2.32). Figure 2.7(b) shows the separation at $\phi = \pi$ of the Andreev energy branches of Eq. (2.42) for increasing values of T , illustrating the transitioning from well-separated energy branches at low values of T to fully closing at $T = 1$.

In Chapter 4, where Eq. (2.32) is applied to model the anharmonicity, the crossing from the adiabatic to the diabatic limit, where Landau-Zener transitions become important, occurs at,

$$r \sim \left(\frac{E_C}{\Delta} \right)^{1/2} = \left(\frac{240 \text{ MHz}}{45 \text{ GHz}} \right)^{1/2} \Rightarrow T \sim 0.995, \quad (2.43)$$

where the parameters $E_C = 240 \text{ MHz}$ and $\Delta = 45 \text{ GHz}$ are the parameters estimated for the device in Chapter 4. We estimate T_i to likely be lower than

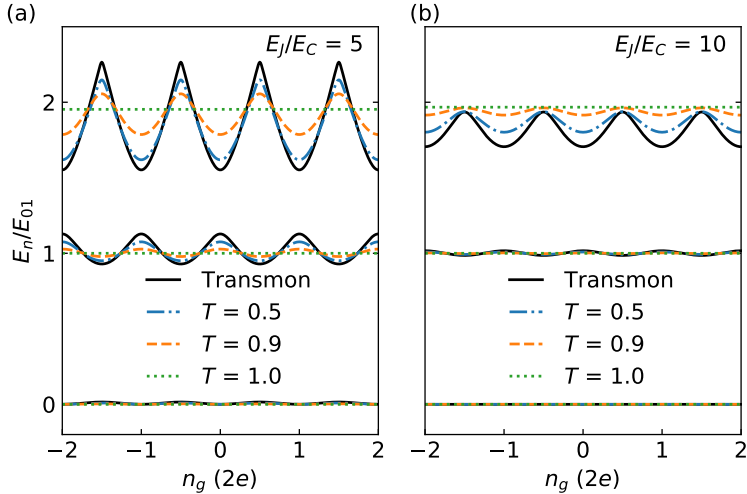


Figure 2.8: Numerical solutions to the two-level Hamiltonian. Numerical solutions to Eq. (2.20) (black) and Eq. (2.41) for the three different transmission probabilities T (blue, orange, green) showing the three lowest energy levels E_n . Solutions for $E_J/E_C = 5$ (a) and $E_J/E_C = 10$ (b) are shown. Energies E_n are normalized to $E_{01}(n_g = 0.25)$.

this value, and in this limit Eq. (2.32) yields the same result as Eq. (2.41). For the measurements discussed in Chapter 7, clear indications of crossing into the diabatic limit are observed, suggesting transmission probabilities exceeding,

$$T \sim 1 - \frac{E_C}{\tilde{\Delta}} = 1 - \frac{540 \text{ MHz}}{25 \text{ GHz}} = 0.98, \quad (2.44)$$

where $\tilde{\Delta}$ is the “effective” gap associated with resonant tunneling (see Chapter 7 and the last paragraph of this section for details on resonant tunneling).

To gain further insights of the influence of varying the transmission probabilities, and in particular the limit of unity transmission, we consider numerical solutions to Eq. (2.41). Figure 2.8 shows numerical solutions to the transmon Hamiltonian Eq. (2.20) and the single-channel model Eq. (2.41) for fixed E_J/E_C [$E_J/E_C = 5$ in (a) and $E_J/E_C = 10$ in (b)]. In order to fix E_J/E_C , $E_J = \Delta T/4$ is kept constant by varying the model value of Δ . The single-channel model for one value of T is equivalent to having N modes, each with transmission T and $\Delta = \Delta'/N$ such that $E_J = \Delta'/4 \times NT$. As T is increased it is observed that

the charge dispersion amplitudes of the energy levels are decreasing. In particular as the transmission reaches unity the energy levels flatten completely. Interestingly, this observation is independent of E_J/E_C . To understand this quenching of the charge dispersion, we can think of a phase particle in the ground state of Fig. 2.7(a). For low T and thereby low tunnel barrier, the phase tunneling probability between $\phi = 0$ of one quasiparticle equilibrium [66] to the next equilibrium at $\phi = 2\pi$ is large [Fig. 2.7(a)]. This results in delocalized phase and as a result charge (conjugate variable of phase) will be localized and the island charge is quantized. When T increases the potential barrier becomes higher resulting in reduced phase tunneling probability. As T approaches unity the tunneling completely vanishes due to the Landau-Zener transitions to the excited Andreev branch. As a result phase is now localized, leaving charge delocalized suppressing charge dispersion. A more intuitive way of understanding the vanishing charge dispersion is by viewing a channel of unity transmission as a "short" to ground. If charges can freely move across the junction, no external charge gate can change the energy of the island. These theoretical concepts inspired a detailed experimental study of the charge dispersion in Chapter 7, where the modeling is also described in detail.

To quantify the influence of increasing T on the anharmonicity and dispersion, we can compute α defined as $\alpha/h = f_{01}(ng = 0.25) - f_{12}(ng = 0.25)$ and the dispersion amplitude of the transition frequency $\delta_{01} = f_{01}(ng = 0) - f_{01}(ng = 0.25)$ as a function of T as shown in Figs. 2.9(a, b). It is noted that $\alpha \rightarrow -E_C/4$ is obtained for $T \rightarrow 1$ even for low E_J/E_C , which was also found with the perturbation method, valid for $\phi \approx 0$. To achieve $\phi \approx 0$, it is usually a requirement to operate in the $E_J/E_C \gg 1$ regime. However, due to the Landau-Zener transitions the $T \rightarrow 1$ regime also results in localized phase and hence the $\phi \approx 0$ approximation is still valid.

In practice when measuring the charge dispersion, quasiparticle poisoning has to be taken into account. A poisoning event shifts the energy levels by $1e$, while otherwise leaving the diagram unchanged, illustrated in Fig. 2.10(a). These levels do not couple to each other because transport across the junction occurs in units of Cooper pairs ($2e$). As the poisoning rate is faster than the measurement rate[§], in a measurement, one would observe the average of

[§]Resolving single quasiparticle tunneling events has been demonstrated [67]. When performing averages over many spectroscopy measurements, however, the poisoning rate is larger than the measurement rate.

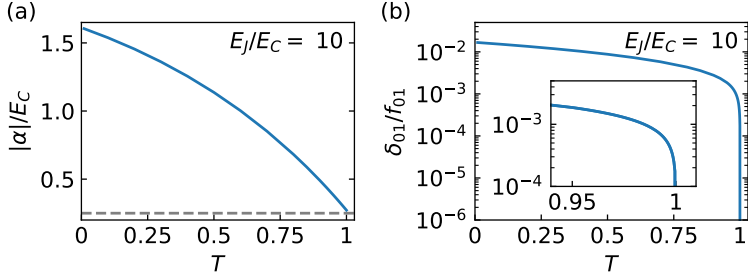


Figure 2.9: Anharmonicity α (a) and dispersion amplitude δ_{01} (b) as a function of transmission T . Qubit frequency f_{01} is defined as $f_{01} = f_{01}(n_g = 0.25)$, which is the qubit frequency at the degeneracy point of the charge dispersion. The $T = 1$ limit $\alpha = -E_C/4$ is indicated in (a) (grey dashed line). Inset: zoom of the region near $T = 1$ in (b) to illustrate the influence of crossing into the diabatic limit at $T \sim 0.99$.

both parity branches [58]. An example of a frequency diagram is shown in Fig. 2.10(b), illustrating the frequency dispersion. The dispersion measurements carried out in Chapters 7 and 8 verify this behavior.

One of the main conclusions of Chapter 7, is the occurrence of resonant tunneling in the junction, which is responsible for the large transmission probability. Resonant tunneling can occur if a quantum dot is formed inside the junction. The theory is explained in detail in Chapter 7, with this paragraph aiming to discuss some of the potential consequences of this new qubit regime. In the resonant regime, the Andreev bound state energy is given as solutions to,

$$2\sqrt{\Delta^2 - E^2} E^2 \Gamma + (\Delta^2 - E^2)(E^2 - \epsilon_r^2 - \Gamma^2) + 4\Delta^2 \Gamma_1 \Gamma_2 \sin^2(\phi/2) = 0, \quad (2.45)$$

where Γ_1 and Γ_2 are the tunnel barriers of the resonant level, ϵ_r is the detuning to the chemical potential, and $\Gamma = \Gamma_1 + \Gamma_2$. Interestingly, these solutions closely resemble the eigenvalues plotted in Fig. 2.7(a), see Section 7.6. However, these solutions are no longer separated by Δ at $\phi = 0$, but rather by an “effective” gap $\tilde{\Delta}$, which can be tuned from 0 to Δ depending on Γ . This new feature provides some interesting new design freedoms. In order to take advantage of the newly discovered quenching of the charge dispersion, one has to take $E_J \geq \Delta/4$ to ensure $\sum T_i > 1$. To obtain as large anharmonicity as possible,

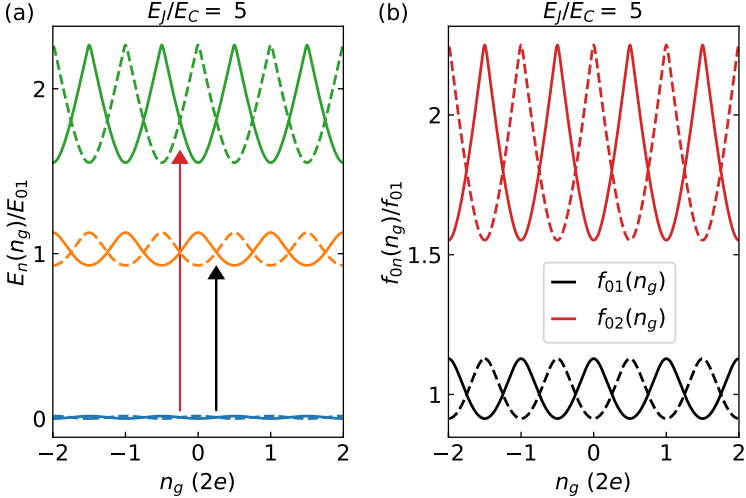


Figure 2.10: Numerical solutions showing poisoned charge dispersion spectrum.
 (a) Numerical solutions to Eq. (2.20) for $E_J/E_C = 5$ showing the three lowest energy levels, E_0 , E_1 , E_2 (blue, orange, green) as a function of offset charge n_g (solid lines). Quasiparticle poisoning shifts n_g by 1e (dashed lines). Energy transitions $0 \rightarrow 1$ (black arrow) and $0 \rightarrow 2$ (red arrow) are indicated. Energies are normalized to the degeneracy transition energy $E_{01} = E_{01}(n_g = 0.25)$. (b) Numerical solutions in (a) converted to transition frequencies $f_{01}(n_g) = [E_1(n_g) - E_0(n_g)]/h$ (black) and $f_{02}(n_g) = [E_2(n_g) - E_0(n_g)]/h$ (red). Numerical solutions (solid lines) and 1e shifted solutions (dashed lines) are plotted. Frequencies are normalized to the degeneracy frequency $f_{01} = f_{01}(n_g = 0.25)$.

it is desired to increase E_C . This, however, puts some constraints on the achievable qubit frequency, which increases with both E_J and E_C (scales with $\sim \sqrt{8E_J E_C}$ in the transmon regime), and one can thereby not freely increase E_C as desired. In the resonant tunneling regime, on the contrary, one only requires $E_J \geq \tilde{\Delta}/4$ to ensure $T > 1$. As $\tilde{\Delta}$ is tunable, it is in principle possible to almost freely choose E_C returning to the CPB regime, while maintaining low charge dispersion, and by doing so increasing anharmonicity substantially compared to conventional transmons. One has to be aware that for $E_J/E_C < 1$, $\hbar\omega_{01} \sim \tilde{\Delta}$. In this regime, two “subgap states” (states within $\tilde{\Delta}$) are expected to be visible, and their influence on the gatemon is not clear. That said, future devices with controllable dot structure and tunnel barriers mark a very

interesting research direction, not only due to potential advantages in terms of transmon parameters, but also in the context of Andreev qubits [68, 69]. In addition, a controllable, near unity transmission channel may be useful in creating protected qubits based on $\cos(2\phi)$ -elements [70, 71], where the potential is more naturally achieved due to the highly transmitting modes.

2.4 QUBIT READOUT AND MANIPULATION

In order to create any useful qubit system, it is of course necessary to be able to manipulate and determine the qubit states. To access information about a qubit system, an effective, non-disruptive method of qubit state readout is required. This section describes some of the basic concepts necessary to understand how the gatemon states are measured and manipulated. The qubit readout and control mechanism described in this Section is derived for a conventional SIS junction-based transmon but everything applies to any transmon qubit regardless of energy phase relation.

2.4.1 QUBIT READOUT

In cQED-based superconducting qubits the states are read out by coupling the qubit circuit to a resonator circuit via a capacitance C_g , see Fig. 2.11. In this case the resonator is a distributed LC oscillator as discussed in Section 2.1, viewed as lumped elements with inductance L_r and capacitance C_r with resulting resonance frequency $\omega_r = 1/\sqrt{L_r C_r}$. This is the lowest mode of the resonator, neglecting the higher modes as they are far away in frequency and effectively do not couple. The coupled system (Fig. 2.11) is described by the following Hamiltonian,

$$H = 4E_C(\hat{n} - n_g)^2 - E_J \cos \phi + \hbar\omega_r \hat{a}^\dagger \hat{a} + 2\beta e V_{\text{rms}}^0 \hat{n}(\hat{a} + \hat{a}^\dagger), \quad (2.46)$$

where $\beta = C_g/C_\Sigma$, and $V_{\text{rms}}^0 = \sqrt{\hbar\omega_r/2C_r}$ is the root mean square voltage of the resonator [30]. In Eq. (2.46) the two first terms are the Hamiltonian of the uncoupled CPB-system already derived [Eq. (2.20)], the third term represents the harmonic oscillator of the resonator, and the last term represents the coupling. We can further rewrite the Hamiltonian in terms of the uncoupled transmon state $|i\rangle$ and the i th transition frequency ω_i to obtain the generalized

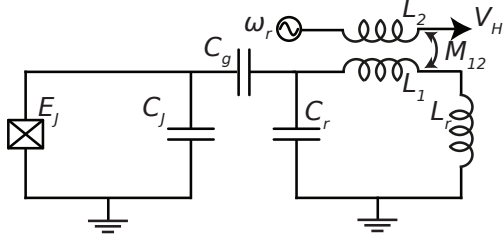


Figure 2.11: Coupled qubit-resonator circuit sketch. Circuit sketch of the combined qubit and resonator system where the qubit is capacitively coupled to the resonator via the capacitance C_g , where the resonator is inductively coupled to a transmission line via the mutual inductance M_{12} . By sending a drive tone with frequency ω_r and measuring the heterodyne demodulated transmission voltage V_H the resonance frequency and thereby the qubit state is determined.

Jaynes-Cummings Hamiltonian [30],

$$H = \hbar\omega_r \hat{a}^\dagger \hat{a} + \hbar \sum_i \omega_i |i\rangle \langle i| + \hbar \sum_{ij} g_{ij} |i\rangle \langle j| (\hat{a} + \hat{a}^\dagger), \quad (2.47)$$

where $g_{ij} = 2\beta eV_{\text{rms}}^0 \langle i| \hat{n} |j\rangle / \hbar$ is the general coupling strength of the i th and j th energy level. In the transmon limit $E_J/E_C \rightarrow \infty$ selection rules yields $\langle i+1| \hat{n} |i\rangle \neq 0$ with all other matrix elements $\rightarrow 0$. Applying this and the rotating wave approximation, i.e. neglecting terms that do not conserve the number of excitations and typically oscillate fast enough to average to zero, we obtain,

$$H = \hbar\omega_r \hat{a}^\dagger \hat{a} + \hbar \sum_i \omega_i |i\rangle \langle i| + \hbar \sum_i g_{i,i+1} (|i\rangle \langle i+1| \hat{a}^\dagger + |i+1\rangle \langle i| \hat{a}). \quad (2.48)$$

Approximating the qubit system as an effective two-level system and rewriting the Hamiltonian in terms of the qubit transition frequency, the spin Pauli operator σ_z , and spin ladder operators σ_+ and σ_- , the original Jaynes-Cummings Hamiltonian is obtained [27,29],

$$H = \hbar\omega_r \hat{a}^\dagger \hat{a} + \frac{\hbar\omega_{01}}{2} \sigma_z + \hbar g (\sigma_+ \hat{a} + \sigma_- \hat{a}^\dagger), \quad (2.49)$$

where $g = g_{01}$.

There are two characteristic regimes of the Jaynes-Cummings Hamiltonian, the resonant regime where $\omega_r = \omega_{01}$ and the dispersive regime where $|\omega_r - \omega_{01}| \gg g$. In the resonant regime the qubit and resonator system hybridize into new states that are superpositions of resonator photon states and qubit excitation states. These new states are split by $2\hbar g$, known as the vacuum-Rabi splitting. In order to observe this effect, the experimental linewidth of the resonator and qubit frequency must be less than g/π . For the devices presented in this thesis typical parameters were $g/(2\pi) \sim 50\text{--}100$ MHz, and qubit and resonator linewidths of around 1 MHz and 5 MHz, respectively.

For the majority of qubit experiments and for all data presented in this thesis, the qubit is operated in the dispersive regime. In order to derive key features in this regime, the generalized Jaynes-Cummings Hamiltonian can be expanded in $g/(\omega_r - \omega_{01})$ valid as $|\omega_r - \omega_{01}| \gg g$. Employing the two-level approximation after the expansion one obtains,

$$H = \hbar(\omega'_r + \chi\sigma_z)\hat{a}^\dagger\hat{a} + \frac{\hbar\omega'_{01}}{2}\sigma_z, \quad (2.50)$$

where $\omega'_r = \omega_r - \chi_{12}/2$ and $\omega'_{01} = \omega_{01} + \chi_{01}$ are the renormalized resonator and qubit frequencies with $\chi_{ij} = \frac{g_{ij}^2}{\omega_{ij} - \omega_r}$ and $\chi = \chi_{01} - \chi_{12}/2$. The key feature of Eq. (2.50) is that the harmonic resonator frequency shifts with $\pm\chi$ depending on the qubit state. All cQED measurements in this thesis rely on this dispersive shift to allow state determination. Using $\omega_{12} = \omega_{01} + \alpha/\hbar$ and $g_{12} = \sqrt{2}g$ [30] we can rewrite χ in terms of α ,

$$\chi = \chi_{01} - \chi_{12}/2 = \frac{g^2}{\Delta_0} - \frac{g^2}{\Delta_0 + \alpha/\hbar}, \quad (2.51)$$

where $\Delta_0 = \omega_r - \omega_{01}$. This highlights the necessity of a finite and preferably large anharmonicity. Importantly, this measurement technique provides a quantum nondemolition (QND) determination of the qubit state, as the state remains in the measured state after readout (neglecting state decay).

Coupling a quantum system to the environment is necessary for access and control, which inevitably introduces decay and decoherence mechanisms. Fortunately, the resonator acts as a filter when detuned from the qubit frequency [27], heavily reducing the dissipative environment experienced by the

qubit [72]. Despite being detuned from the qubit, the spontaneous decay rate of the qubit is still modified due the coupling to the resonator, known as the Purcell effect [32, 73]. The Purcell decay rate γ_κ depends on Δ_0 , g and the decay rate of the resonator κ ,

$$\gamma_\kappa = \kappa \frac{g^2}{\Delta_0^2}. \quad (2.52)$$

Typical parameters for the experiments of this thesis are $g \sim 50\text{--}100$ MHz, $\kappa \sim 30$ MHz (quality factor $Q = \omega_r/\kappa \sim 1000$), and $\Delta_0 \sim 1\text{--}2$ GHz, resulting in lower bounds of the decay rate of $\gamma \sim 0.1 \mu\text{s}^{-1}$. For high fidelity readout, it is of interest to be able to perform fast readout and hence increasing κ . However, this would result in enhanced Purcell decay, and for this reason Purcell filters [74] are often implemented, where the transmission line effectively is a resonator. As this was not crucial for the research in this thesis, this extra complication was omitted.

In summary, this section describes how individual energy states of a transmon qubit systems can be read out by coupling to harmonic resonators. For all measurements in this thesis, the resonance frequency is determined by transmission measurements through an inductively coupled transmission line, as illustrated in Fig. 2.11. For more detailed discussions of the Jaynes-Cummings Hamiltonian and circuit quantum electrodynamics I refer to Refs. [27, 30, 51].

2.4.2 QUBIT MANIPULATION

This subsection describes how the gatemon states are manipulated. By capacitively coupling the qubit to an external voltage source, either directly as shown in Fig. 2.3 or through the resonator as shown in Fig. 2.11, the qubit state can be manipulated by microwave tones. This coupling to a drive modifies the dispersive two-level Hamiltonian of Eq. (2.50), which in the rotating frame of the drive frequency ω_d yields,

$$H = (\hbar\Delta_r + \hbar\chi\sigma_z)\hat{a}^\dagger\hat{a} + \frac{\hbar\Delta_q\hat{\sigma}_z}{2} + \frac{\hbar}{2}(\Omega_R(t)\sigma_x + \Omega_I(t)\sigma_y), \quad (2.53)$$

where $\Delta_r = \omega_r - \omega_d$, $\Delta_q = \omega_{01} - \omega_d$, and $\Omega(t) = \Omega_R(t)\cos(\omega_d t) + \Omega_I(t)\sin(\omega_d t)$ is the Rabi frequency of the drive. See for instance Ref. [60] for a detailed

derivation of the driven dispersive Jaynes-Cummings Hamiltonian. In order

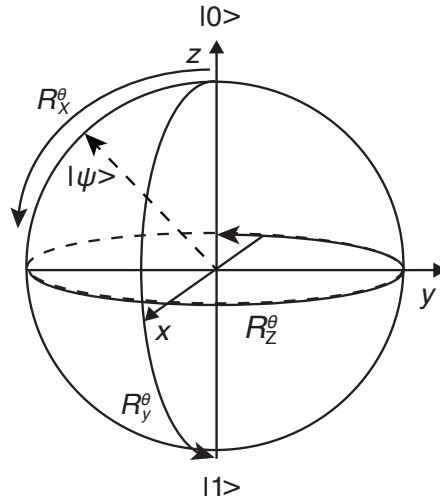


Figure 2.12: The Bloch sphere used to visualize any qubit state $|\psi\rangle$ as a vector anywhere on the sphere. Qubit manipulation can be viewed as rotations R_i^θ around any axis.

to visualize the qubit control we can think of the qubit state as a vector in Bloch sphere, where the two poles are the ground ($|0\rangle$) and excited ($|1\rangle$) state. Any qubit state (up to a global phase) $|\psi\rangle = \alpha|0\rangle + \beta|1\rangle$ can be viewed as a vector in the sphere, and to fully control the state it is required to be able to perform rotations around all three axes, see Fig. 2.12. From Eq. (2.53) is it clear that by choosing the phase and amplitude of the drive, we can perform any rotation around the x - and y -axes. In practice we achieve these rotations by IQ modulation, as discussed in Section 3.4.2, where the modulation pulses $I(t)$ and $Q(t)$ plays the role of Ω_R and Ω_I . Due to the Δ_q -term in Eq. (2.53) the qubit state vector will rotate (in the rotating frame) with Δ_q around the z -axis. This is exactly what is employed when performing a Ramsey measurement in Section 3.4.2, where the drive tone is slightly detuned or interleaved with a gate pulse.

2.5 HYBRID cQED - MAJORANA TRANSMON

Topological materials suggest an exciting platform for quantum computing, where the material is naturally protected against local noise sources [45]. When spin-orbit coupling and Zeeman energy is present in a one-dimensional proximitized nanowire, Majorana zeros modes (MZMs) are predicted to emerge [75, 76], which has been followed by compelling experimental signatures [43, 77–79]. As a step towards a qubit based on Majorana physics, a hybrid design merging cQED and topological superconductivity is proposed in Ref. [44]. In this proposal each superconducting segment (each side of the Josephson junction) of a transmon device host MZMs at the ends. In a simplified picture this gives rise to a $1e$ coherent coupling across the Josephson junction due to the overlap of two MZMs, which modifies the transmon Hamiltonian,

$$H = 4E_C(\hat{n} - n_g)^2 - E_J \cos(\hat{\phi}) + 2iE_M\gamma_2\gamma_3 \cos(\hat{\phi}/2), \quad (2.54)$$

where γ_2 and γ_3 are the Majorana operators of the two modes on each side of the junction satisfying $\gamma_i^\dagger = \gamma_i$, and $\{\gamma_i, \gamma_j\} = \delta_{ij}$. E_M is the energy splitting associated with the overlap of γ_2 and γ_3 , see Ref. [44] for more details. As gatemon qubits are build by similar nanowires, where signatures of MZMs have been observed, it is a natural platform to realize this proposal. This requires operating the gatemon in magnetic fields of the order of 1 T, typically required to enter the topological phase. This challenge has been addressed by promising progress in field compatible resonators [80], and field compatible gatemon qubits presented in Refs. [71, 81] and Chapter 8. If possible to tune the gatemon nanowire to the topological regime, a distinct signature is expected to be visible in the charge dispersion. Figure 2.10 shows a poisoned spectrum, where the two island parity energy branches are visible. These branches are uncoupled as transport across the junction occurs in units of Cooper pairs ($2e$). However, if the E_M -coupling term is realized, the two parity branches will couple, and new states are created, where island parity is no longer well defined. In this regime, depending on the range of E_C , E_J , and E_M avoided crossings are expected to be detectable in the charge dispersion spectrum. In practice this picture is too simplified and one has to take the Andreev spectrum into account, which together with finite junction effects may significantly complicate this experiment and the expected signatures [82]. Despite significant experimental efforts in this thesis, and also in Refs. [71, 81, 83] no clear signatures of Majorana physics in a cQED architecture has been demonstrated.

3

Experimental Methods

This chapter presents a detailed overview of the device fabrication and the experimental setup. While the specific fabrication details of each device depends on the aim of the experiment, many of the fabrication steps are very similar. The general workflow of device fabrication is described in Section 3.1. The exact fabrication recipes for each device are provided in Appendices A and B pointing out the differences between each design. Section 3.2 describes the packaging and mounting of the devices and Section 3.3 gives a detailed description of the experimental setup. Finally, the Chapter is concluded with a general description of the applied measurements techniques along with common examples of their use.

3.1 DEVICE FABRICATION

The process of fabricating nanowire-based gatemon devices relies on several complicated techniques. These processes require professional cleanroom tools and lithography facilities. This section describes each fabrication stage in chronological order. All the devices presented in this thesis was fabricated on high resistive silicon substrates (above $5\text{ k}\Omega\text{cm}$), which freeze out at milliKelvin temperatures). In order to build highly coherent superconducting qubit devices, it is crucial to have a low loss substrate and good material in-

terfaces, which makes silicon an ideal candidate [84]. The substrate was then covered with a thin superconducting film, ~ 100 nm Al for the devices in Chapters 4 and 5, and ~ 20 nm NbTiN for the devices in Chapters 6, 7, and 8. The use of thin NbTiN films was motivated by its higher critical field compared to Al, allowing the use of magnetic field compatible resonators [80].

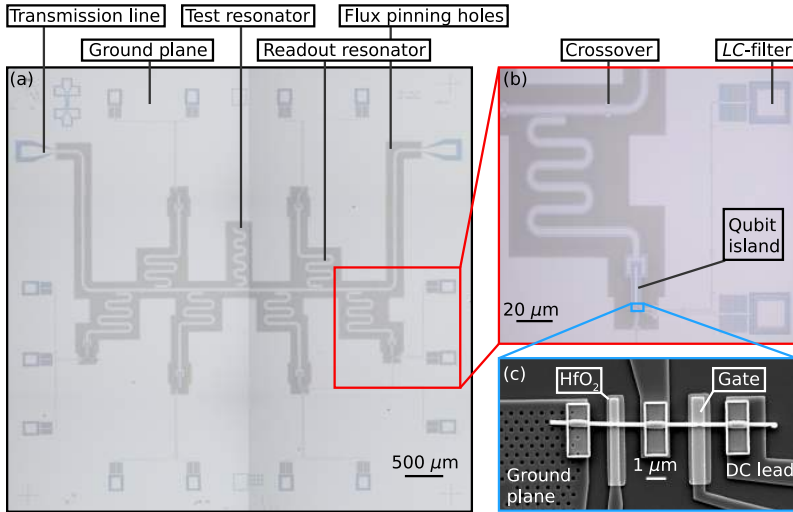


Figure 3.1: Device overview of gatemon devices. (a) Full optical image of a gatemon device. A common transmission line is coupled to six individual readout resonators, and one test resonator. Each of the readout resonators capacitively couple to qubit islands, with one example highlighted (red rectangle). (b) Magnified optical image of the highlighted region in (a). A nanowire is placed at the bottom of each qubit island (blue rectangle). Electrostatic bottom gates control the nanowires, and are connected via the LC-filters. Two of the crossovers connecting the ground plane on each side of the transmission line are visible. (c) Scanning electron micrograph of the nanowire region. Two gateable segments of $\sim 100\text{--}200$ nm were formed, controlled with the bottom gates, which was electrically isolated from the nanowire by a 15 nm HfO_2 dielectric (two bright regions). Flux pinning holes were patterned in the ground plane. This is the device design presented in Chapters 6 and 7, where the gatemon qubit has an additional gateable region to allow DC transport. Traditional gatemon qubits only have one gateable region, as shown in Chapters 4, 5 and 8.

The superconducting circuits were defined by either UV lithography (UVL) or electron-beam lithography (EBL) [85]. Here, the substrate was covered with a resist, often PMMA (polymethyl methacrylate) for EBL or AZ photo resist for

UVL, which was damaged by the exposed beam in a desired pattern. These patterns consist of the individual distributed quarter wavelength ($\lambda/4$) readout resonators, which were inductively coupled to a common transmission line. In the same lithography step, electrostatic gates, on-chip LC-filters [86], nanowire regions, and the qubit islands were defined. The qubit islands serve as the shunt capacitances discussed in Chapter 2 and determine the charging energy E_C . By removing the exposed resist by a solvent-based developer, followed by exposing the device to an etchant, the thin film was removed in the patterned areas, constructing the circuit shown in Fig. 3.1(a). The capacitive coupling g between the qubit islands and readout resonators depends on the capacitance ratio $\beta = C_g/C_\Sigma$, as discussed in Section 2.4. Both the total capacitance C_Σ and the coupling capacitance C_g can be estimated using electrostatic simulations [87], allowing relative precise pre-knowledge of relevant qubit parameters. In similar fashion the inductive coupling to the transmission line was determined by the length of the resonator segment in close vicinity of the transmission line and the distance to it. Desired coupling quality factors were found experimentally by fabricating several devices and extracting their respective quality factors. In addition, a test resonator was incorporated in the qubit design, which allowed extraction of the internal quality factors, usually found to be of the order of 10^5 . Other important design choices included the ratio between the strip line and trench width and film thickness, crucial for matching the characteristic impedance of the resonator [88] with the rest of the $50\ \Omega$ electronic environment. The film thickness only played an important role for NbTiN-based devices due to the large (and thickness dependent) kinetic inductance [84].

In a subsequent lithography step, following the etch, we defined gate- and crossover-dielectric patterns. The dielectric was then deposited with atomic layer deposition techniques in the pre-defined regions. The gate dielectric ensured no leakage current for voltage ranges of around ± 10 V. The crossover dielectric was used to ensure that the crossovers that were deposited in a subsequent EBL-step did not short the control lines to ground. These initial fabrication steps were usually the same for all devices and designs, and were therefore typically performed on a full wafer, allowing having both multiple copies of the same structures, and different designs. Each fabrication step ended with a removal of the resist and a cleaning of the wafer.

The next phase concerned the nanowire processing, which were often

carried out on a subset of the wafer, by first cleaving the wafer into several chips. The epitaxial nanowires [89] were grown on separate wafers by Peter Krogstrup and his team. Nanowires were then placed in the pre-defined nanowire regions. For the device in Chapter 4, this was done with random dry deposition [90], where many nanowires were randomly placed into the region. More recently, and for all other devices* presented in the thesis, the nanowires were placed with a micromanipulator [91], where single nanowires were picked up with a tungsten needle from the nanowire growth chip. The nanowires were then placed on top of the gate dielectric with sub-micrometer precision, see Figs. 3.1b, c. Following the placement, a small segment of a few hundred nanometers (defined by EBL) was etched to form a gateable semiconducting segment, constituting the gatemon Josephson junction. In a final fabrication step, one side of the Josephson junction was connected to the ground plane and the other side was connected to the island, forming the gatemon circuit, see Fig. 3.1(c). At this step the crossovers were also connected, used to tie up the ground plane on each side of any strip line to reduce spurious modes [92].

3.2 MOUNTING THE DEVICE

In order to connect the finalized device to the electronic control equipment, the device chip was mounted in a circuit board, typically glued to the board with a droplet of PMMA or epoxy. A non-conducting epoxy was chosen to avoid introducing new loss mechanisms. Hereafter, all the DC gate and microwave control lines were connected to the individual lines on the circuit board by Al wire bonds. In addition, multiple wire bonds connected the ground plane of the circuit board to the ground plane of the device chip to tie the ground plane together to minimize spurious resonance in the device. Figure. 3.2 show examples of bonded devices mounted to the circuit boards.

Following the wire bonding, the device was mounted in a sample box. The sample packaging plays a crucial role in achieving long qubit coherence times and careful considerations are required. Superconducting qubits are very sensitive to radiation, either radiation at the qubit frequencies or infrared radiation generating quasiparticles [93,94], all leading to enhanced relaxation

*Chapter 5 presents a deterministic alternative to the nanowire assembly based on dielectrophoresis.

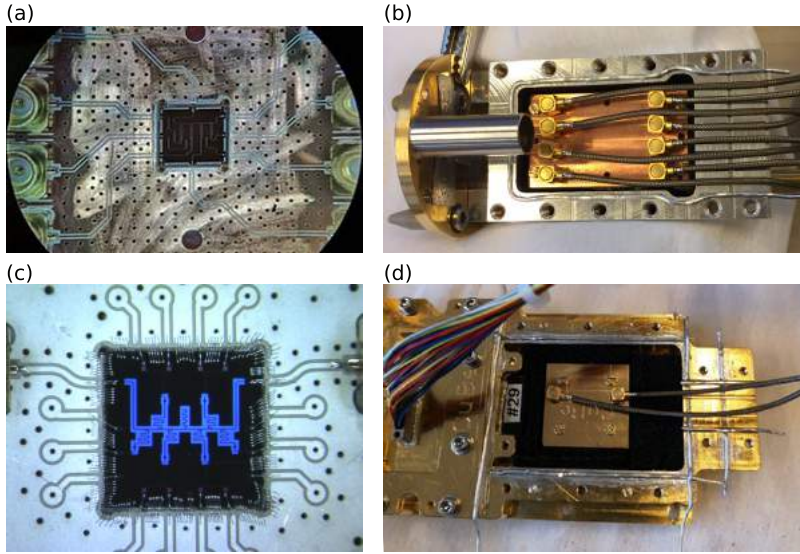


Figure 3.2: Device packaging. (a) Example of a bonded device chip on the circuit boards used in Chapters 4 and 5. Eight striplines were bonded to the sample to connect transmission lines, DC gate lines and microwave drive lines to SMP connectors. The samples were mounted in an indium sealed Al sample box, shown in (b). (c) Example of a bonded device of the same design and circuit board used in Chapters 6, 7, and 8. In this design, the transmission lines were bonded to two striplines, which were connected to SMP connectors. The remaining 14 lines on the board were DC lines connected to the nano-d outlet shown in (d). The samples were mounted in an indium sealed CuBe box, shown in (d) with a second cavity for DC filtering and outlet (left). The sample was shielded with a CuBe lid and Eccosorb foam.

of the qubit devices. Therefore, it is important that the samples are properly shielded. The Al-based samples measured in Chapter 4 were mounted in an Al box. This box was used for the experiments that were carried out at zero applied magnetic fields as the superconducting Al prevented changes in the magnetic field and therefore protected the sample. The box was coated with light absorbing paint to reduce radiation [71]. A Cu lid was placed on top of the chip to avoid any box resonances at the qubit frequencies. Indium wires are placed in the designed trenches [Figs. 3.2(a, b)] to further seal the box. Hereafter, the box was mounted in another Cu box and the microwave and DC lines are connected to the SMP and DC outlets of the Cu box. This box

was then connected to the outlets of the mixing chamber plate, which allowed connection to the wiring inside the cryostat. This allowing addressing the qubit with the room temperature electronic equipment, see Section 3.3.

The NbTiN-based samples measured in Chapters 6, 7, and 8 were designed to be compatible with large magnetic fields, and were operated in cryostats equipped with a vector magnet. Therefore, the packing of these samples was slightly different. The sample was mounted inside a CuBe box, chosen as CuBe has a high thermal conductance and low electric conductance. This minimized the heating from eddy currents when operating in large magnetic fields, while still ensuring good thermalization. Furthermore, these samples by design had more DC electrostatic gate electrodes. To accommodate this, we changed from applying DC signals through the bias tees and coaxial lines [Figs. 3.2(a, b)] to connecting directly to the DC cable assembly in the cryostat via the nano-D connector [Fig. 3.2(d)]. The filtering of the DC lines is very important to avoid introducing a new dominant relaxation source by the coupling to the environment via the voltage gates. Therefore these devices are designed with on-chip LC-filters [86], see Figs. 3.1(a, b). Additionally, just before connecting the device inside the CuBe box, the DC lines were further filtered in an indium sealed box inside a second cavity of the CuBe box, see Fig. 3.2(d). To further limit radiation, the device was surrounded by light absorbing Eccosorb LS-26 foam. The sample box was then mounted in another Cu box for connection to the mixing chamber. This box design was developed after the first measurements of gatemon qubits in magnetic fields. Here, the devices were mounted on a similar circuit board and then mounted directly in the Cu box. In this setup, it was found that the T_1 relaxation times were limited to a few hundred nanoseconds. In a first attempt to improve this, the devices were wrapped in the Eccosorb foam, which increased T_1 and led to the development of the current box design.

3.3 MEASUREMENT SETUP

This section presents a detailed overview of the electronic measurement setup and wiring of the cryostat for all the measurements presented. Figures 3.3 and 3.4 presents schematics of the full setup used in Chapters 4 and 5, and Chapters 6, 7, and 8, respectively. As the two setups were nearly identical it is sufficient to only describe one of them in detail, focussing on the setup in

Fig. 3.4. An input microwave voltage signal was generated, either by a Rohde & Schwartz VNA or a vector signal generator. This room temperature signal was heavily attenuated and filtered to minimize heat and noise at the sample, operated in cryostats with base temperatures of around 10 mK. The return signal coming from the devices passed through an additional low pass filter and two isolators, to minimize reflections to the sample. Before reaching the readout circuit at room temperature, the signal was amplified with a low noise amplifier at 4 K and again at room temperature. Depending on the type of measurements the signal returned to the VNA or the Alazar readout circuit, controlled by the RF switch. In order to drive both the resonator and the qubit frequency, the input signal was a combined signal from two signal generators. These signals were modulated by the arbitrary waveform generator (AWG) to achieve the desired pulse sequences.

The last part of the setup was the DC circuit used to gate the nanowires and to perform transport measurements. To achieve sufficient filtering the DC lines were filtered both at the mixing chamber plate with QDevil filters and inside the sample box. DC voltages were generated by a QDac digital to analog converter [95], which were used to gate the qubit (V_Q) and the FET (V_{FET}), as explained in Chapter 6. A third DC voltage was used to bias the lead (V_B). This DC voltage was combined with an AC voltage generated by the lock-in amplifier via the voltage divider. The returning current I was then amplified and converted to a voltage by the Basel I-to-V converter. This voltage, which contains DC and AC components was then measured by the multimeter (DC) and the lock-in amplifier (AC).

The two setups presented are of similar dilution refrigerator systems, with the setup in Fig. 3.4 equipped with a 6-1-1 vector magnet. Other differences among the setups include removing the cryoperm magnetic shielding, and removing Eccosorb low pass filters for field compatibility. In addition, for the setup in Fig. 3.3 the DC lines were combined with the coaxial lines via home-made bias tees consisting of a 10 k Ω resistor and a 5 nF capacitor. This was necessary as the DC signal would be filtered out by the attenuators connected to the coaxial lines. Additionally, the qubits were not driven via separate microwave drive lines in Fig. 3.4 compared to Fig. 3.3 (green lines), but instead the qubits were driven through the resonators. This change was unrelated to the operation in magnetic fields, but had to do with the scope of the experiments being of more fundamental character, where individual control of the

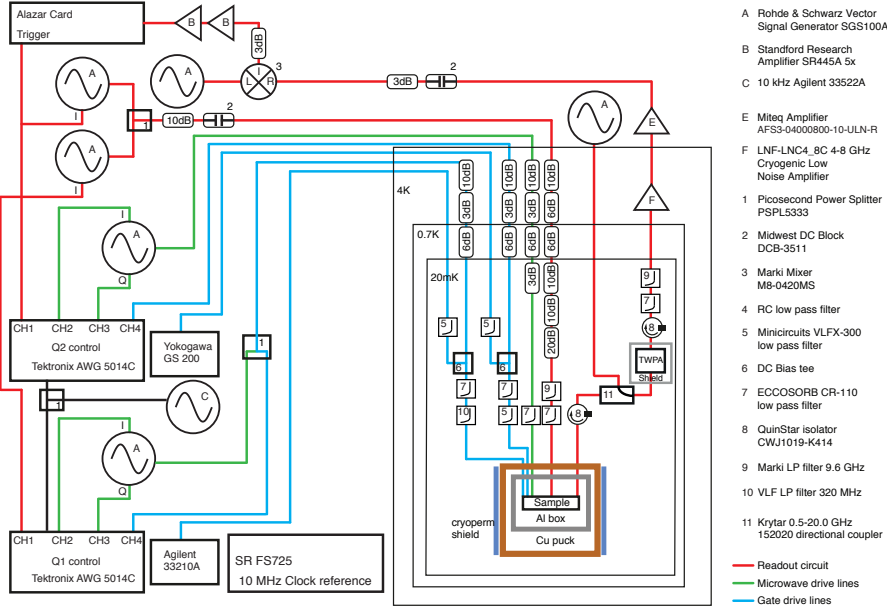


Figure 3.3: Detailed schematic of the measurement setup used in Chapters 4 and 5. The red lines refer to microwave readout lines, the green lines refer to microwave qubit drive lines, and the blue lines refer to DC lines, used for gating the nanowire junctions. All microwave equipment is connected to the 10 MHz clock reference. The figure is adapted from Ref. [96].

qubits were not needed. In order to switch quickly between vector network analyzer (VNA) and pulsed measurements an RF switch was implemented in Fig. 3.4. The setup in Fig. 3.3 had a traveling wave parametric amplifier (TWPA) installed [97]. This allowed the implementation of faster readout and single shot measurements but this was not crucial to the experiments using the setup of Fig. 3.4. Other measurements (not shown) were carried out in a setup with both a magnet and a TWPA. Finally, the equipment used for transport measurements (blue lines in Fig. 3.4) was not compatible with the devices in Chapter 4.

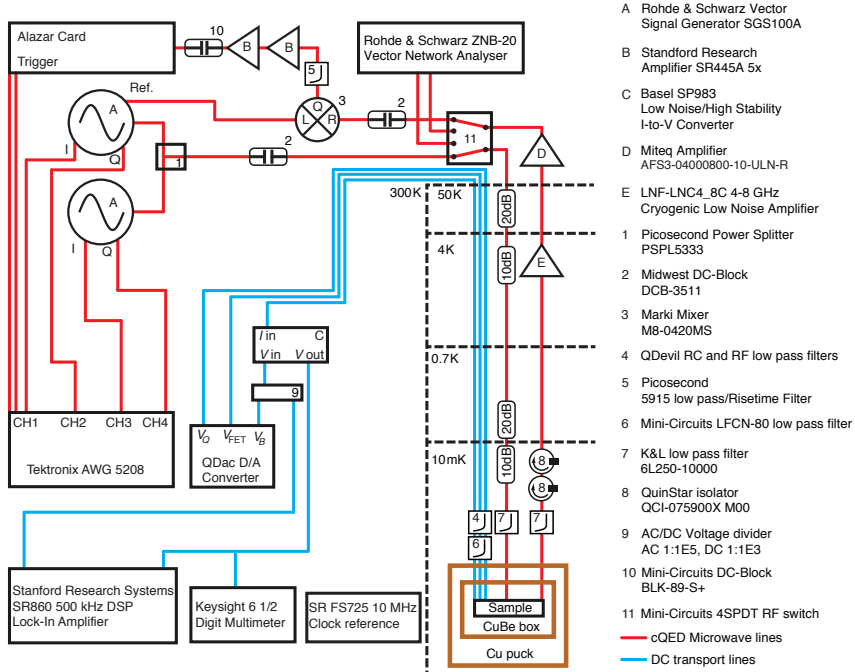


Figure 3.4: Detailed schematic of the measurement setup used in Chapters 6–8. The red lines refer to microwave readout and control lines. The blue lines refer to DC lines for transport measurement and gating of the nanowire. All microwave equipment is connected to the 10 MHz clock reference. The dilution refrigerator is equipped with a 6-1-1 vector magnet. The figure is adapted from Ref. [98].

3.4 MEASUREMENT TECHNIQUES

Measurements of gatemon qubit devices are typically based on microwave transmission measurements, which determines the resonance frequency of the readout resonator f_{res} . As discussed in Chapter 2, from determining f_{res} one can infer the state of the qubit, when operated in the dispersive regime. The microwave measurements of this work is based on two measurement techniques, measurements with a VNA, and pulsed AWG-based time domain measurements, based on mixing of input signals and demodulation of output signals. Recently, we have demonstrated the compatibility of DC/AC transport measurements and gatemon qubits, as discussed in Chapter 6 and Ref. [98].

These measurements were based on DC current and voltage measurements, and AC lock-in measurements.

Despite these three measurement techniques being different, they all rely on the same feature, the mixing of the transmitted signal with a reference tone. Filtering out the high frequency component, the magnitude and phase of the return signal from the sample are extracted. This process takes place in both the VNA and in the homebuilt demodulation circuit. The lock-in amplifier relies on the same principle but with much lower frequencies, typically 10–100 MHz. Throughout this thesis the current to ground was measured. As the capacitance to ground is finite the measured resistance is frequency dependent for high frequencies, due to the decreasing impedance. As a consequence measurements were performed with signal frequencies of tens of hertz.

3.4.1 FREQUENCY DOMAIN MEASUREMENTS

Continuous one-tone RF transmission measurements have been key in this thesis. These measurements were often acquired with a VNA. The VNA can measure the transmission through a sample fast and has a large dynamic range. Therefore, it is an ideal tool for initial measurements. Furthermore, the VNA automatically demodulates the incoming signal with a reference tone reducing the amount of additional circuit elements when the VNA is used for probing the qubit and resonator characteristics. These measurements were mostly used to probe the resonator, where continuous one-tone measurements are a very valuable characterization tool. Such measurements are often used in the first characterization of a new device. For instance, probing the power dependence of f_{res} is a simple measurement, which provides valuable information of the qubit. Figure 3.5(a) shows a transmission measurement for varying resonator drive frequency f_r , performed at two different powers. It is observed that f_{res} shifts to a lower frequency value at low powers (-120 dBm). This is expected due to the hybridization of the qubit and resonator, which is saturated at high power (-60 dBm), where the uncoupled f_{res} is obtained [27]. From this measurement, according to the theory presented in Chapter 2, we can infer an interaction between the gatemon and the resonator circuit. Additionally, we can conclude that the qubit frequency f_{01} is larger than f_{res} at the particular junction gate $V_Q = 0$ V, due to the negative Lamb shift $\chi_{01} = g^2 / (\omega_{\text{res}} - \omega_{01})$. In particular, as g is estimated from the device design (discussed in Section 3.1),

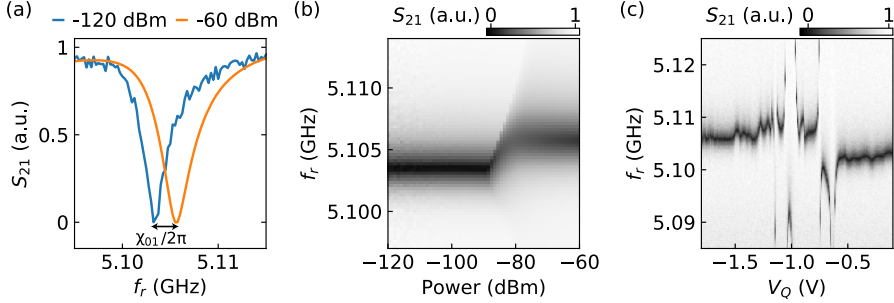


Figure 3.5: Examples of common VNA measurements. (a) Transmission amplitude S_{21} measurement as a function of resonator drive frequency f_r at drive power = -120 dBm (blue) and -60 dBm (orange). The Lamb shift χ_{01} is indicated (arrow). The scan is taken at junction gate $V_Q = 0$ V. (b) S_{21} as a function of drive power and f_r . A shift in the resonance frequency f_{res} is observed as the power is decreased, again associated with χ_{01} . (c) S_{21} as a function of V_Q and f_r . Multiple avoided crossings associated with the qubit frequency f_{01} and f_{res} are equal. As V_Q is increased f_{res} varies from being above the bare value to below, indicating that f_{01} changes from being below f_{res} at low V_Q to being above at larger V_Q .

such a measurement allows relative precise estimation of f_{01} . Figure 3.5(b) shows a full power scan demonstrating the gradual hybridization as the drive power is decreased. Similarly, measuring f_{res} as function of V_Q [Fig. 3.5(c)] provides direct information of how f_{01} depends on V_Q with a simple and fast measurement. We can identify that for $V_Q < -1.5$ V and for $V_Q > -0.5$, f_{01} is significantly lower and larger than f_{res} , respectively. We infer this due to the vanishing Lamb shift, leaving f_{res} nearly gate independent in those regimes. In the intermediate regime, we observe a highly gate-dependent spectrum and multiple avoided crossing, indicating that the qubit is being tuned in and out of resonance with the resonator. This nonmonotonic dependence on V_Q is typical for gatemon qubits and is discussed further in Chapters 4 and 6.

3.4.2 TIME DOMAIN MEASUREMENTS

To directly probe the state of the qubit and its coherence, time domain measurements are required. These measurements allow manipulation of the qubit for a given time, followed by state readout. To perform such pulsed measurements, an output microwave signal is required with a frequency of 1-10 GHz

for pulse durations as short as few nanoseconds. To achieve this, we modulate the microwave signal of the signal generators with an AWG-generated envelope, using the IQ mixer ports of the signal generators, see Fig. 3.4. Here I and Q represent the real and imaginary part of the signal, also sometimes referred to as the in-phase and quadrature component, respectively. The IQ mixer consist of two mixers and a 90° hybrid coupler. When an incoming signal $\cos(\omega t)$ goes through the hybrid coupler a phase shifted signal $\sin(\omega t)$ is generated, and the two signals goes to the I and Q mixer, respectively. When the signal passes the two mixers each component is multiplied by the AWG input of the I and Q channels, resulting in a modulated signal,

$$V = I(t) \cos(\omega t) + Q(t) \sin(\omega t), \quad (3.1)$$

where $I(t)$ and $Q(t)$ are time dependent and takes any shape generated by the AWG. For most of the measurements in this thesis, square pulses are applied to create the measurement pulses. This is sufficient as high fidelity operation and readout has not been a target of this thesis, rather the experiments presented have been of “*proof-of-principle*” character. For high fidelity gate operation, pulse shaping plays a crucial role. Here, Gaussian pulses and derivatives of Gaussian pulses (DRAG) are commonly used [59].

In order to perform the actual measurements, a modulated drive pulse was applied to the qubit, either through external drive lines (Fig. 3.3) or through the common transmission line (Fig. 3.4). Following the qubit drive pulse, a second pulse of frequency ω_r was applied to probe the readout resonator. The transmitted signal was then first mixed with a reference signal with frequency ω_{LO} , where ω_{LO} was usually chosen such that $(\omega_r - \omega_{\text{LO}})/(2\pi) \sim 10\text{--}100 \text{ MHz}$. As a consequence, the mixed signal V_m has two frequency components and is given by,

$$\begin{aligned} V_m &= A_r \cos(\omega_r t + \phi) A_{\text{LO}} \cos(\omega_{\text{LO}} t) \\ &= \frac{A_r A_{\text{LO}}}{2} (\cos[(\omega_r - \omega_{\text{LO}})t + \phi] + \cos[(\omega_r + \omega_{\text{LO}})t + \phi]). \end{aligned} \quad (3.2)$$

Here, ϕ is the phase difference between the reference and the transmitted signal, and A_r and A_{LO} are the amplitudes of the reference and local oscillator drive, respectively. By filtering the high frequency component away, and by further digital down-conversion in software by the Alazar card, we can ex-

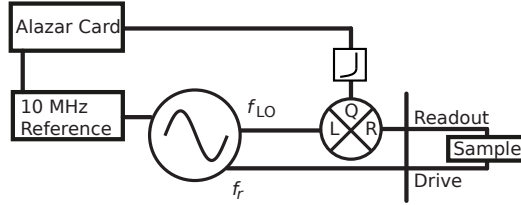


Figure 3.6: Schematic illustrating the concept of the demodulation circuit. Two microwave signals are generated, the drive tone with frequency f_r , and a reference signal f_{LO} . The drive tone is applied to the sample and the transmitted signal is mixed with the reference signal, resulting in a low and high frequency component. By filtering the high frequency component away with a low pass filter, the low frequency signal is measured with the Alazar card. All microwave equipment is connected to a reference for synchronization.

tract both the amplitude and phase of the returned signal. Figure 3.6 shows a reduced circuit illustrating the fundamental concepts of the heterodyne demodulation circuit. Here, heterodyne refers to the fact that the reference and input signal have different frequencies. This allows for parallel measurements of multiple readout resonators, which are probed at different detuning frequencies.

An important aspect of this setup is the use of single side band (SSB) modulation, where a carrier frequency is shifted by a certain frequency ω_s [88, 99]. This, for instance, allows the reference signal to be generated by the same RF source as the input signal. The main frequency is moved by $\omega_s/(2\pi) \sim 10\text{--}100\text{ MHz}$, while the reference signal remains unchanged. This is achieved by applying two modulation pulses $I(t) = \cos(\omega_s t)$ and $Q(t) = \mp \sin(\omega_s t)$ for the desired pulse duration. The resulting signal yields,

$$\begin{aligned} V(t) &= I(t) \cos(\omega t) + Q(t) \sin(\omega t) \\ &= \cos(\omega_s t) \cos(\omega t) \mp \sin(\omega_s t) \sin(\omega t) \\ &= \cos[(\omega \pm \omega_s)t], \end{aligned} \quad (3.3)$$

which allows choosing an input signal of a desired frequency. As the input and reference signals are generated by the same source, phase drift errors are circumvented, see Ref. [71] for more details.

We also apply SSB modulation to vary the qubit drive frequency when

performing two-tone spectroscopy measurements. Here, a pulsed drive tone at varying frequency f_d is applied [Fig. 3.7(a)], followed by a readout tone to extract the demodulated transmission voltage V_H . The drive tone is applied for a time comparable to the relaxation time T_1 , to ensure finite excited state population. In order to vary f_d , one could step the carrier frequency of the RF source after each measurement cycle. This is a slow process that increases acquisition time. Instead, we SSB modulate the carrier frequency by a sequence of pre-defined waveforms from the AWG. This significantly speeds up the acquisition time and this is how the measurement in Fig. 3.7(a) was performed. This measurement technique is central for the anharmonicity measurements in Chapter 4, the mapping of qubit frequency in Chapter 6, the dispersion measurements in Chapter 7, and is also used to probe the qubit behaviour in a magnetic field in Chapter 8.

Other very commonly used time domain measurements are Rabi measurements, where a drive tone is applied at f_{01} for a variable time τ . As τ varies the qubit state rotates around the equator of the Bloch sphere. The average of V_H indicates the qubit state probability (note that the mapping is not one to one), which is observed to oscillate between the ground and excited state, see Fig. 3.7(b). The Rabi measurement is then used to define the π -pulse, which is the pulse that rotates the qubit an angle of π from the ground to the excited state. Modulating the drive with either the $I(t)$ or $Q(t)$ determines whether the state is driven around the x - or y -axis of the Bloch sphere. The π -pulse is extracted by fits to a damped sinusoid, $V_H(\tau) = A \exp(-\tau/T^2) \sin(\omega\tau + \phi) + B$, where T denotes the characteristic Rabi decay time. This allows characterizing the T_1 times of a device by exciting the qubit with a π -pulse, followed by a variable wait time τ between the π -pulse and readout tone. As τ increases the qubit decays into the ground state with a characteristic exponential time scale T_1 . Fits to a decaying exponential allow extraction of T_1 , as shown in Fig. 3.7(c). To characterize decoherence mechanisms a Ramsey measurement is commonly used, where the qubit is brought to the equator of the Bloch sphere by a $\pi/2$ -pulse. Applying this pulse slightly detuned from f_{01} will result in a rotating state vector at this detuning frequency (in the rotating frame as discussed in Chapter 2). By varying the wait time τ before applying a second $\pi/2$ -pulse the probability of the projected qubit oscillates, see Fig. 3.7(d). Due to dephasing, the state probability decays with an envelope described by the decoherence time T_2^* . We extract T_2^* from fits to $V_H(\tau) = A \exp[-(\tau/T_2^*)^2] \sin(\omega\tau + \phi) + B$.

The Ramsey measurement is an example of controlled driving around the z -axis. Driving around the z -axis is often achieved by interleaving optimised $\pi/2$ -pulses with a gate pulse (or a flux pulse for conventional transmons), or by using so-called virtual- Z gates, where changing the phase of the drive is utilized to generate z -rotations [59, 100].

The time domain measurements in Figs. 3.7(b)–(d) also take advantage of the sequence mode of the AWG, where all waveforms are uploaded and running in a continuously. To automatically assign each data point to the corresponding waveform, two triggers are applied, one for each measurement cycle, and one for each sequence start, see Fig. 3.4. This is opposed to manually stepping between each waveform in a sequence, which introduces significant overlay.

3.4.3 DC TRANSPORT MEASUREMENTS

Traditionally DC transport has not been part of transmon or gatemon qubit measurements. However, as demonstrated in Chapter 6 and Ref. [98], by adding a second gateable segment to a gatemon, the compatibility with DC transport measurements is achieved. The transport measurements in this thesis are mainly based on two-probe voltage bias measurements. We apply a DC bias voltage V_B together with a much smaller AC voltage (usually of amplitude $dV_B \sim 10\text{--}100 \mu\text{V}$ and frequency of tens of Hertz). The resulting current I_B will contain both an AC and DC component. We amplify and convert I_B to a voltage, and measure the DC and AC components. The DC component is measured with a voltage meter. The AC component is measured with the lock-in amplifier, which works much like the demodulation circuit. The incoming signal is mixed with a reference signal of same frequency and phase as the outgoing voltage. Mixing the measured signal results in a DC component and a component of twice the lock-in frequency. With a low pass filter the high frequency component is filtered out as described in Section 3.4.2. As before this allows us to extract the magnitude of the incoming AC current dI_B , and its phase (or real and imaginary components). From this we can construct the differential conductance dI_B/dV_B . Typical transport measurements involve obtaining pinch-off curves of gateable junction segments, the induced superconducting gap by tunnel spectroscopy, and switching current measurements. These measurements are described and applied in Chapter 6.

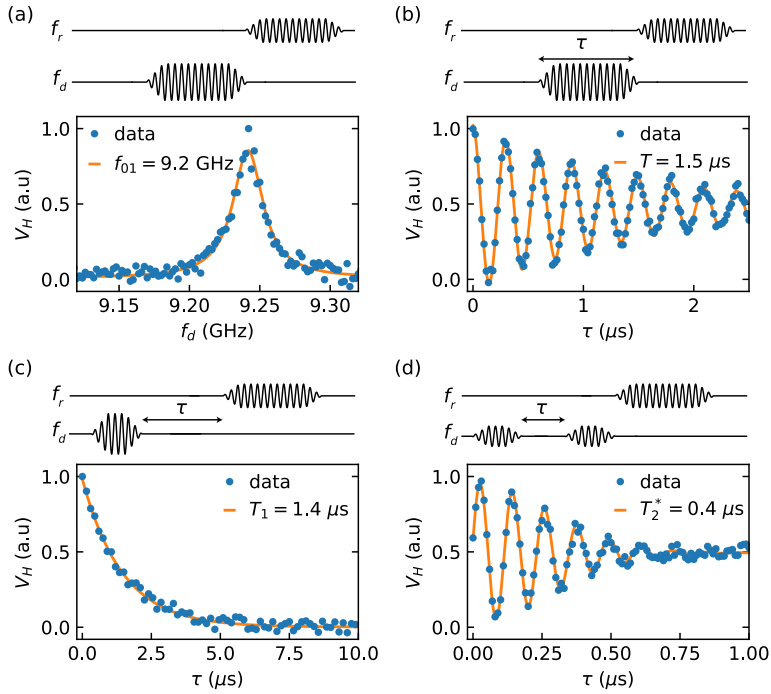


Figure 3.7: Representative examples of common time domain measurements. (a) Two-tone spectroscopy measurement (bottom) and the applied pulse sequence (top). A broad pulse is applied at a variable drive frequency f_d , followed by a readout pulse at f_r . Due to the dispersive shift, the measured transmission voltage V_H (blue data points) changes when the qubit is excited, resulting in the observed peak. Qubit frequency f_{01} is extracted by fits to a Lorentzian line shape (orange line). (b) Rabi measurement (bottom) and corresponding pulse sequence (top). The qubit transition is driven for a variable pulse width τ . Measurements of V_H (blue data points) reflects the state probability when averaged over many data points. It is noted that V_H is normalized in all panels and does not map directly to the probability. A characteristic Rabi decay time T is extracted by fits to exponentially damped sinusoids (orange line). (c) Example of an T_1 lifetime measurement. The qubit is excited by a π -pulse with variable wait time τ before the readout pulse (blue data points). The excited state probability decays with characteristic time T_1 , extracted by fits to a damped exponential. (d) Example of Ramsey measurement to extract dephasing time T_2^* . The qubit state is brought to the equator by a $\pi/2$ -pulse with a variable wait time τ before a second $\pi/2$ -pulse, which projects the state back to the measurement axis, followed by a readout tone. T_2^* can be extracted by fits to $V_H(\tau) = A \exp[-(\tau/T_2^*)^2] \sin(\omega\tau + \phi) + B$ (orange line).

4

Anharmonicity of a Superconducting Qubit with a Few-Mode Josephson Junction

Coherent operation of gate-voltage-controlled hybrid transmon qubits (gatemons) based on semiconductor nanowires was recently demonstrated. Here we experimentally investigate the anharmonicity in epitaxial InAs-Al Josephson junctions, a key parameter for their use as a qubit. Anharmonicity is found to be reduced by roughly a factor of two compared to conventional metallic junctions, and dependent on gate voltage. Experimental results are consistent with a theoretical model, indicating that Josephson coupling is mediated by a small number of highly transmitting modes in the semiconductor junction.

This chapter is adapted from Ref. [101]. Chapter 2 provides a more detailed derivation of the anharmonicity formula and a comparison to the two-level model used in Chapter 7. Additional information on the device fabrication and the measurement setup is found in Chapter 3.

This work was done in collaboration with L. Casparis, M. Hell, T. W. Larsen, F. Kuemmeth, M. Leijnse, K. Flensberg, P. Krogstrup, J. Nygård, K. D. Petersson, and C. M. Marcus. The presented device was part of Ref. [96]. The analysis, modeling, and writing were done as part of this thesis.

4.1 INTRODUCTION

The transmon qubit is an anharmonic oscillator where the Josephson junction (JJ) provides a nonlinear inductance that allows for the lowest two energy levels to be selectively addressed [30,32,55]. The anharmonicity $\alpha = E_{12} - E_{01}$, where E_{ij} is the energy difference between energy states j and i , is a critical qubit design parameter, determining, for instance, the minimum pulse duration $\sim \hbar/|\alpha|$ needed to avoid leakage into noncomputational states. Transmons have recently demonstrated one- and two-qubit gate fidelities exceeding 0.99 in multi qubit devices [102–104].

Almost without exception, transmon qubits are based on superconductor-insulator-superconductor (SIS) junctions that use a thin insulating barrier (typically Al_2O_3) between metallic superconducting leads [46]. SIS junctions are well described by a nonquadratic (cosine) energy-phase relation $V_{SIS} = -E_J \cos(\phi)$, where E_J is the Josephson coupling energy and ϕ is the phase difference across the junction [51]. The inverse inductance correspondingly depends on phase, $L_{SIS}^{-1} = (2e/\hbar)^2 d^2 V_{SIS}/d\phi^2 = (2e/\hbar)^2 E_J \cos(\phi)$. Other types of JJs with weak links separating superconducting electrodes made from narrow superconducting constrictions, normal metal, or a semiconductor [56,105,106] have energy-phase relations that differ from the cosine form. Coherent operation of one- and two-qubit circuits using superconductor-semiconductor-superconductor (S-Sm-S) junctions—called gatemons due to their gate-voltage controlled E_J —were recently demonstrated using an InAs nanowire (NW) with epitaxial Al [38,61]. In those experiments, it was noted that $|\alpha|$ was roughly a factor of two smaller than what one would expect for an SIS junction with the same operating parameters, but the origin and parameter dependence of this discrepancy were not investigated.

Other experiments have investigated an S-Sm-SJJ in a two-junction loop [39]. Near one-half flux quantum through the loop, the anharmonic spectrum revealed signatures of a noncosinusoidal energy-phase relation in the S-Sm-S junction. More recently, nonsinusoidal current-phase relations of nanowire S-Sm-S junctions were directly measured from the diamagnetic response of mesoscopic rings interrupted by single S-Sm-S junctions [107].

In this Chapter, we investigate anharmonicity as well as departure from the standard (SIS) cosine energy-phase relation in a nanowire-based gatemon qubit. We observe that anharmonicity depends on gate voltage and is lower

than the corresponding SIS junction with comparable E_J . Comparing anharmonicity data to a model of Josephson junctions with few conduction channels, we find our data are consistent with 1–3 dominating conducting channels contributing to the Josephson current. These results are broadly relevant to superconducting qubits based on novel junction materials.

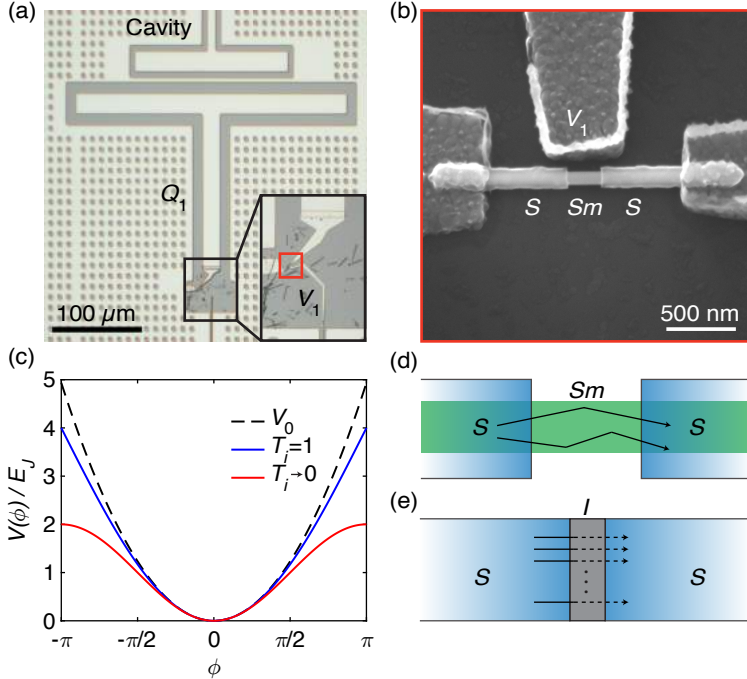


Figure 4.1: Qubit device and Josephson potential. (a) Optical micrograph of one of the qubits, Q_1 , in the two qubit device. The inset shows a zoom in of the junction region. Each qubit consists of a T-shaped island shunted to ground via an InAs/Al NW JJ. The two qubits are designed to be nominally identical and are both coupled to individual readout resonators. (b) Scanning electron micrograph of the S-Sm-S JJ for Q_1 . The JJ features an InAs NW with high transparency epitaxial Al contacts. The voltage V_1 on the side gate modulates the density of carriers in the NW, allowing the Josephson potential to be modified. (c) The normalized Josephson potential $V(\phi)$ in the limits of $T_i = 1$ (blue solid curve) and $T_i \rightarrow 0$ (red solid curve). For comparison, a harmonic potential V_0 is also shown (black dashed curve). (d) Sketch illustrating a NW S-Sm-S JJ with a few highly transmitting channels in a quasiballistic regime as expected in the NW. (e) Sketch of the conventional SIS tunnel junction with many low transmitting channels.

4.2 THEORY

The gatemon qubit consists of a superconducting island with charging energy E_C , connected to ground via a single JJ made from a $L \sim 200\text{-nm}$ segment of bare InAs NW with superconducting leads proximitized by a full shell of epitaxial Al [89, 108] (details below). We consider transport in the so-called short-junction limit $L \ll \xi$, where ξ is the junction coherence length [56]. In the short-junction regime, originally considered by Beenakker for the case of a metal junction, multiple conduction channels are characterized by their transmission eigenvalues $\{T_i\}$ [109]. Within this model, charge transport across the junction occurs via Andreev processes at each S-Sm interface. For each transmission channel, multiple Andreev reflections between the two interfaces result in a pair of discrete subgap states or Andreev bound states, each with ground state energy $-\Delta\sqrt{1 - T_i \sin^2(\phi/2)}$, where Δ is the induced superconducting gap in the leads [68, 105, 110]. Summing over all conduction channels gives the Josephson potential

$$V(\hat{\phi}) = -\Delta \sum_i \sqrt{1 - T_i \sin^2(\hat{\phi}/2)},$$

where $\hat{\phi}$ is the superconducting phase-difference operator.

The gatemon qubit is operated in the transmon regime, $E_J/E_C \gg 1$, where sensitivity to offset charge of the island is exponentially suppressed [30]. Omitting the offset charge, the effective Hamiltonian is given by

$$\hat{H} = 4E_C \hat{n}^2 + V(\hat{\phi}),$$

where \hat{n} is the island Cooper pair number operator, conjugate to $\hat{\phi}$. The qubit transition frequency is given by the Josephson plasma frequency, $f_{01} \approx \sqrt{8E_C E_J}/h$.

To examine how anharmonicity α depends on the channel transmission probabilities, we derive an expression for α by expanding $V(\hat{\phi})$ to 4th order

in $\hat{\phi}$,

$$\begin{aligned} V(\hat{\phi}) &\approx \frac{\Delta}{4} \sum_i \left(\frac{T_i}{2} \hat{\phi}^2 - \frac{T_i}{24} (1 - \frac{3}{4} T_i) \hat{\phi}^4 \right) \\ &= E_J \frac{\hat{\phi}^2}{2} - E_J \left(1 - \frac{3 \sum T_i^2}{4 \sum T_i} \right) \frac{\hat{\phi}^4}{24}, \end{aligned}$$

where the constant term has been omitted and $E_J = \frac{\Delta}{4} \sum T_i$ [30,51,60]. Here, the $\hat{\phi}^2$ -term has the same form as the potential $V_0(\hat{\phi}) = E_J \frac{\hat{\phi}^2}{2}$ in the harmonic oscillator Hamiltonian $\hat{H}_0 = 4E_C \hat{n}^2 + V_0(\hat{\phi})$. Treating $V'(\hat{\phi}) = -E_J \left(1 - \frac{3 \sum T_i^2}{4 \sum T_i} \right) \frac{\hat{\phi}^4}{24}$ as a perturbation to \hat{H}_0 allows us to calculate the corrections to the harmonic transition energies. Evaluating the perturbation matrix elements $\langle i | V'(\hat{\phi}) | i \rangle$ for $i = 0, 1, 2$ leads to

$$\alpha \approx -E_C \left(1 - \frac{3 \sum T_i^2}{4 \sum T_i} \right).$$

In the limit of $T_i \rightarrow 0$ for all i , $\alpha \approx -E_C$ as is the case for transmons with SIS JJs [30]. For $T_i = 1$, $\alpha \approx -E_C/4$, giving a reduced qubit nonlinearity compared to the SIS JJ case. For a detailed derivation of transmon and gate mon anharmonicity I refer to Sections 2.2 and 2.3.

Measurements of InAs NWs give a typical mean free path $l \sim 100$ nm [111] and Fermi velocity $v_F \sim 10^8$ cm/s [112]. From measurements of similar NWs with epitaxial Al, $\Delta \sim 190$ μ eV [108], giving a superconducting coherence length of $\xi_0 = \hbar v_F / \pi \Delta \sim 1100$ nm for the proximitized InAs leads. These estimates give a junction coherence length $\xi = \sqrt{\xi_0 l} \sim 300$ nm, suggesting an intermediate regime, $L \sim \xi$, that would give corrections to the short junction model taken above [109]. Nonetheless, a number of recent experiments using very similar nanowire S-Sm-S JJs have shown good agreement with theory in the short junction limit and we assume this model here [107,110,113].

Figure 4.1(c) illustrates the connection between channel transmissions and anharmonicity by comparing the Josephson potential in two limiting cases, $T_i = 1$ and $T_i \rightarrow 0$, to a harmonic potential ($\alpha = 0$). The case $T_i \rightarrow 0$ yields a $-\cos(\phi)$ potential, corresponding to an SIS tunnel barrier with many low-transmission channels [Fig. 4.1(e)]. The ballistic case $T_i = 1$ yields a $-\cos(\phi/2)$

potential, which more closely resembles a harmonic potential. For NW S-Sm-S JJs with quasiballistic transport dominated by a few channels [Fig. 4.1(d)], one expects and observes behavior between these two limits.

4.3 ANHARMONICITY MEASURMENTS

Experiments were carried out using a two-qubit device, fabricated in the same way as the device in Ref. [61] (The detailed fabrication recipe is provided in Appendix A). Figures 4.1(a, b) show one of the qubits and its NW JJ. Control lines and qubit islands are lithographically defined on a 100 nm thick Al film evaporated on a high resistivity Si substrate. The JJ is constructed from a NW with a ~ 75 nm diameter InAs core and a ~ 30 nm thick epitaxial Al shell [89], where a $L \sim 200$ nm segment of the shell is removed by wet etching [38, 61].

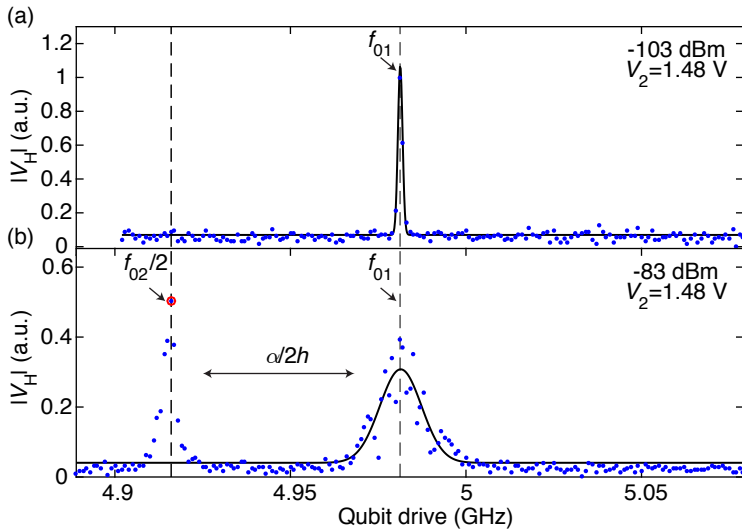


Figure 4.2: Spectroscopy scans to probe the anharmonicity. (a) The qubit is driven by a -103 dBm microwave pulse, which excites the qubit at the transition frequency f_{01} . By measuring the qubit-state-dependent demodulated cavity response $|V_H|$, f_{01} can be determined. The data points (blue) are fitted to a Gaussian (solid black curve) to locate f_{01} . (b) After identifying f_{01} , the two photon $|0\rangle \rightarrow |2\rangle$ transition frequency $f_{02}/2$ is probed in a spectroscopy scan at -83 dBm. f_{01} is extracted by fitting a Gaussian around the value found in (a) and $f_{02}/2$ is identified as the maximum value of the second peak as labeled in red. $\alpha/2h = f_{02}/2 - f_{01}$ is indicated with the horizontal arrow.

E_J of the JJ is voltage controlled with a side gate labelled V_1 in Figs. 4.1(a, b). The two qubits, denoted Q_1 and Q_2 , are coupled with strength $g/2\pi \sim 80$ MHz to individual superconducting $\lambda/4$ resonators with resonance frequencies $f_{C1} \approx 7.66$ GHz, $f_{C2} \approx 7.72$ GHz. These measurements were performed at 20 mK in a dilution refrigerator with a similar setup as in Ref. [61]. Multiplexed dispersive readout is performed through a common transmission line [114], using a superconducting travelling wave parametric amplifier to improve the signal-to-noise and reduce the acquisition time [97]. Coherence measurements show qubit lifetimes and inhomogeneous dephasing times, $T_1, T_2^* \sim 1\text{--}2 \mu\text{s}$. Both quasi-two-dimensional and fully three-dimensional electrostatic simulations [87, 115] yield $E_C/h = 240$ MHz, taking Si permittivity $\epsilon = 11.7$.

Anharmonicity is measured by first locating the qubit transition frequency f_{01} in a low-power scan (typically ~ -100 dBm at the sample). This is performed by applying a microwave excitation with a pulse length of $1 \mu\text{s}$ through a control line capacitively coupled to the qubit island. The microwave pulse excites the qubit into a mixed state when applied at f_{01} , directly detectable in the demodulated cavity response $|V_H|$, as shown in Fig. 4.2(a). Repeating the scan at higher power (~ -80 dBm) allows both f_{01} and the two-photon $|0\rangle \rightarrow |2\rangle$ transition frequency $f_{02}/2$ to be measured simultaneously, as shown in Fig. 4.2(b). Frequency f_{01} is extracted from a Gaussian fit to the $|0\rangle \rightarrow |1\rangle$ transition peak, whereas $f_{02}/2$ is taken to be the maximum value of the $|0\rangle \rightarrow |2\rangle$ peak. Anharmonicity is then given by $\alpha = 2h(f_{02}/2 - f_{01})$.

Tunability of the junction allows f_{01} and α to be measured for different sets of channel transmissions $\{T_i\}$ by performing spectroscopy at different gate voltages, as shown in Fig. 4.3. The right axes in Figs. 4.3(a, b) show $\sum T_i = (hf_{01})^2/2\Delta E_C$, taking E_C from electrostatic modeling and $\Delta = 190 \mu\text{eV}$ [108]. Nonmonotonic gate dependence presumably reflects standing waves in the junction due to disorder, as discussed previously [38, 61]. Figures 4.3(c, d) show anharmonicity α as a function of gate voltages. Both qubits show reduced anharmonicity compared to the corresponding SIS value of $|\alpha| = E_C = 240$ MHz $\times h$ with sizable fluctuations with gate voltage. Comparing Figs. 4.3(a)-(d), we observe that fluctuations in α are more pronounced than those in f_{01} . The larger fluctuations in α may reflect that whereas f_{01} only depends on $\sum T_i$, α is determined by both $\sum T_i$ and $\sum T_i^2$, that is, it depends on both the total transmission and the variance of the transmission coefficients. Recent work from Goffman *et al.* [113], has extracted transmission coefficients for similar

semiconductor NW JJs by fitting current-voltage characteristics to multiple Andreev reflection theories. In this work, it was observed that individual channel transmissions can show far more variation compared to the total transmission, which may further account for the pronounced fluctuations in α observed here.

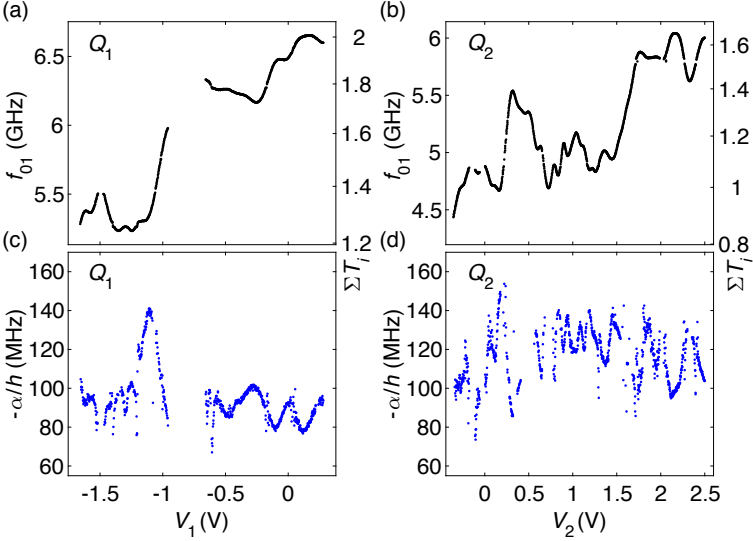


Figure 4.3: Results of the spectroscopy and anharmonicity measurements. (a) and (b) Results of spectroscopy measurements of f_{01} for varying gate voltage V_1 (V_2) on Q_1 (Q_2). The right axis indicates the total transmission $\sum T_i$ as converted from f_{01} (see text). (c) and (d) Results for α/h measured for Q_1 (Q_2) as a function of gate voltage, V_1 (V_2).

4.4 ANHARMONICITY ANALYSIS

Spectroscopy data along with model calculations for several different distributions for $\{T_i\}$ are shown in Fig. 4.4, as functions of both gate voltage and total transmission, $\sum T_i$, extracted from Figs. 4.3(a, b). Theoretical plots show the model for three cases of equal transmission probability T in each channel, $\alpha = -E_C \left(1 - \frac{3}{4}T\right) = -E_C \left(1 - \frac{3E_J}{\Delta N}\right)$ for different numbers of participating channels, $N = 2, 3$, and ∞ . A fourth model (“Ideal QPC”) assumes that the $\{T_i\}$

are maximally packed for a given total transmission, that is, channels are filled in a staircase with at most one partially transmitting channel, setting a lower bound on anharmonicity.

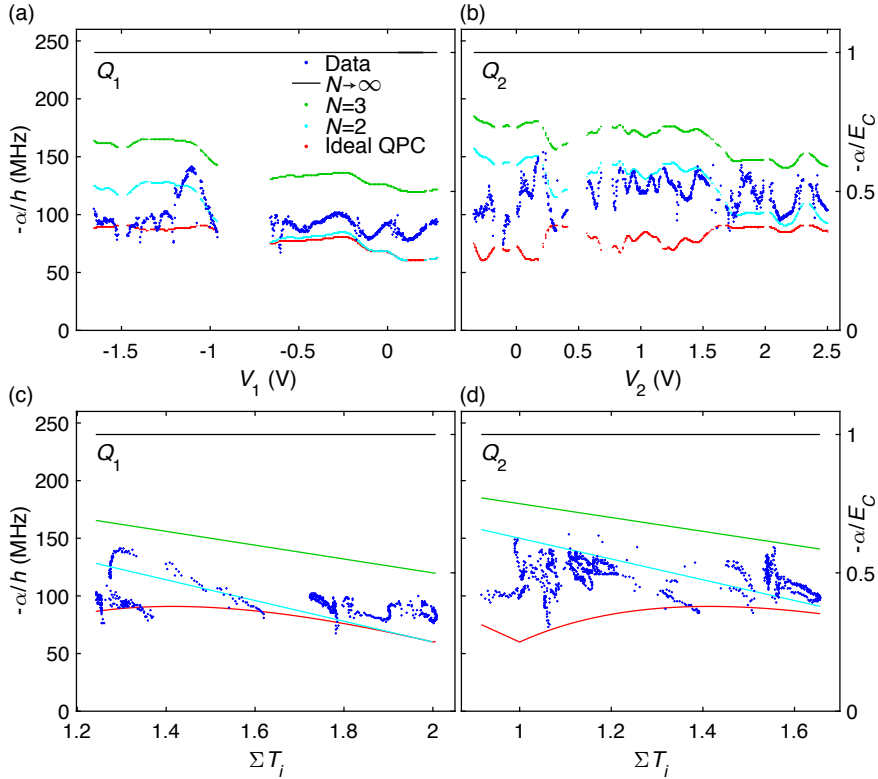


Figure 4.4: Comparison of the anharmonicity data and model. Comparison of the anharmonicity data (dark blue) to our model with four different channel transmission distributions for the JJ. Three of the distributions assume N equally distributed channels plotted for $N = 2$ (light blue), $N = 3$ (green) and $N \rightarrow \infty$ (black). The fourth model data set (red) is for an “Ideal QPC” distribution (see main text for further details). (a) and (b) α as a function of V_1 (V_2) compared with the different models. (c) [(d)] α plotted parametrically against $\sum T_i$ for Q_1 (Q_2), as determined from Figs. 4.3(a, b). The right axes are normalized to E_C highlighting the departure from the conventional transmon result, $\alpha \approx -E_C$.

Anharmonicity data yield information about both the number and the transmission of participating modes. In particular, data above a given N -equal-distribution line indicates that at least $N + 1$ modes are participating, whereas data below a given N -equal-distribution line place a lower bound, $T_{\min} > \sum T_i / N$, on the most transmissive of the participating modes. For example, for the data in Fig. 4.4, we conclude that transport is dominated by 1-3 modes and T_{\min} is in the range of 0.4 to 0.9, depending on gate voltage.

4.5 CONCLUSIONS

Measured values of anharmonicity for the gatemon are reduced by a factor of ~ 2 compared to corresponding transmons with SIS junctions. As a consequence, control pulses must be a factor of ~ 2 slower for the gatemon to avoid state leakage. SIS-based transmons are typically designed with $E_C/h = 200 - 300$ MHz to allow for fast control pulses in the few-nanosecond regime, while maintaining $E_J/E_C \gg 1$ to ensure dephasing due to charge noise and quasiparticle poisoning is suppressed [58]. This regime may not be optimal for the gatemon, however, and it may be possible to increase E_C to allow faster control while remaining insensitive to charge fluctuations in the island. This is because when any channel transmission approaches unity, energy dispersion with charge is predicted to vanish [116]. Similarly, recent experiments with a normal metal island have shown the quenching of charging quantization in the limit of a ballistic channel [117]. In future work we will look to better understand and demonstrate the optimal E_J/E_C ratio for gatemons, potentially exploiting this reduced (and in principle vanishing) dispersion^{*}.

In summary, we have measured anharmonicity of a gatemon qubit, yielding information about the set of transmissions of the few participating channels in the semiconductor junction. Our results indicate that three or fewer channels significantly participate in transport, depending on gate voltage, consistent with a noncosinusoidal energy-phase relation. We note that one may further exploit higher harmonic terms in the noncosine form of the energy-phase relations to create novel superconducting elements. For two NW JJs in parallel in a superconducting loop, tuning the applied flux and junction gate voltages should allow any $\cos(\phi)$ term to be strongly suppressed while still

*This was experimentally verified in subsequent experiments, which are reported in Chapter 7 and Ref. [118].

having a significant $\cos(2\phi)$ coupling [39]. Such $\cos(2\phi)$ junction elements have been proposed as the basis for new types of qubits that are intrinsically protected against sources of decoherence [70, 119].

5

Deterministic Dielectrophoretic Assisted Assembly of Nanowire-based Gatemon Qubits

In this chapter, we demonstrate deterministically assembled nanowire-based multi-qubit gatemon devices by integrating dielectrophoretic fabrication techniques into existing qubit designs. This is achieved by applying an AC voltage to the qubit circuit covered with a suspension of nanowires in a diluted isopropyl alcohol solution. In doing so, nanowires can be made to align in predefined regions, allowing automation of further nanowire fabrication. We present measurements of a six qubit device, where all six nanowires successfully align, allowing for automated fabrication. All six qubits demonstrate coherent operation and relaxation times of 1–5 μ s.

Additional information on the device fabrication and the measurement setup is provided in Chapter 3. Apart from the dielectrophoretic assisted nanowire assembly the specific fabrication recipe is nominally identical to the recipe presented in Appendix A.

The dielectrophoresis setup was developed by Robert McNeil. The automatic gate- and contact design-software was developed by Karl Petersson. Devices were fabricated in collaboration with Robert and Karl. Measurements were performed in collaboration with Natalie Pearson.

5.1 INTRODUCTION

Gate-controlled gatemon qubits have shown promising progress in terms of two-qubit operation [61] and improved coherence times [62], since the first realizations [38, 39]. In addition, gatemons feature a unique compatibility with quantum dot physics [118, 120], and may potentially be combined with topological materials due to their field compatibility [71, 80]. Building a multi-qubit gatemon device has so far required individual placement of nanowires. This placement can be achieved with sub-micron precision with a micromanipulator (see Section 3.1) or the nanowires may be distributed randomly in a lithographically defined region of several microns. Each technique has advantages and disadvantages, but common to both techniques is the need for post-deposition inspection and custom design for each individual nanowire. This custom strategy allows reliable fabrication of few-qubit devices. However, scaling to many qubits is not feasible while relying on individual nanowire placement, although image recognition software [62] may relax the need for individual inspection and custom design. More scalable platforms such as two-dimensional electron gas [40] or selectively grown patterned structures [63] have either already been used to demonstrate gatemon qubits or show promising prospects of doing so. These platforms, however, suffer from dielectric losses due to the growth substrate typically a piezoelectric III-IV material, which limits coherence times [40]. An alternative direction is deterministic assembly of nanowire devices using dielectrophoresis (DEP) [121, 122], which has already shown the capability of building electrically functional devices [123, 124].

5.2 NANOWIRE ASSEMBLY

Devices were fabricated on high resistivity silicon substrates, covered with a ~ 100 nm thin Al film. The superconducting circuit is patterned with electron-beam lithography (EBL) and reactive ion etching techniques (as described in Chapter 3). The circuit includes transmission lines, individual distributed readout resonators and qubit islands. To integrate the DEP techniques, one end of the transmission line of each device was connected to large electrodes (16 devices visible in Fig. 5.1), where each transmission line is shorted to all readout resonators and qubit islands on each device. This allowed connection

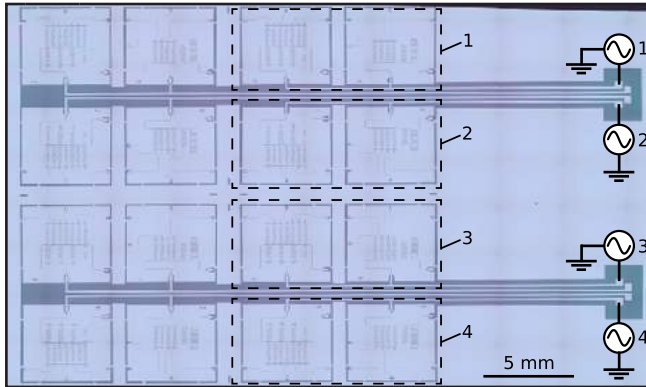


Figure 5.1: DEP wafer overview. Optical image of the DEP device wafer. 16 qubit chips were patterned on the wafer, where one end of each of the transmission line of the qubit devices was connected to the large electrodes (labeled on the right hand side). Each electrode was connected to an AC voltage source (four out of eight electrodes labeled). This allowed sending an AC voltage to each pair of qubit chips (dashed rectangles).

to a voltage source, which provided an AC voltage difference between the qubit islands and the ground plane [Fig. 5.2(a)], which were key in integrating dielectrophoretic techniques with cQED resonator designs. Small openings in a protective resist mask for nanowires were defined with EBL leaving the rest of the substrate protected, see Fig. 5.2(b). The wafer was then covered with a suspension of nanowires in an isopropyl alcohol (IPA)/water solution. Due to the oscillating electric fields generated by the voltage source, nanowires preferentially align in the resist windows [121, 122]. This process did not occur with perfect yield, both with failure modes of multiple wires getting trapped or none at all. However, having six copies [Fig. 5.2(b)] of the nanowire windows ensured that each island site had a sufficiently large probability of having a nanowire aligned that all qubit islands had at least one suitably aligned nanowire, see Fig. 5.2(c).

At this point, the fabrication process continues with the normal workflow of gatemons (as described in Chapter 3). A small segment of a few hundred nanometers was removed by an etchant from the Al shell of each nanowire, forming a gateable region, which acts as the gatemon Josephson junction. In this fabrication step, the connections between the transmission line, readout

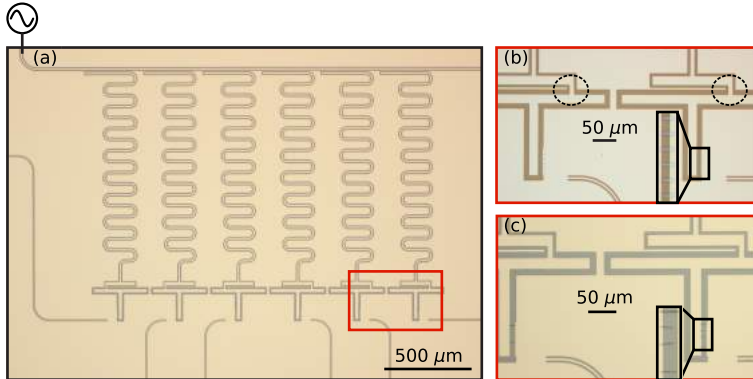


Figure 5.2: Device overview illustrating the fabrication process. (a) Optical image of a device chip during the nanowire placement process. By applying an AC voltage to the transmission, an oscillating field between the ground plane and the qubit island is created. (b) Magnified view of two of the qubit island highlighted in (a) (red rectangle). The transmission line is shorted to each qubit island via each readout resonator (dashed circles). Six small resist windows are defined at the bottom of the qubit islands, with one qubit region highlighted in the zoom-in. These windows are defined by electron-beam lithography. At this point the nanowire solution is applied to the wafer and nanowires align in these windows. (c) Same view as (b) but after applying the nanowire solution and the DEP assisted alignment. At both qubit islands a few nanowires are aligned as desired after the resist has been removed, with one qubit region highlighted in the zoom-in.

resonators and qubit island were also etched away [Figs. 5.3(a)–(c)]. Hereafter, the substrates are loaded into a scanning electron microscope. Automated images were acquired at each predefined nanowire site, as defined by the lithography design file. The images were then automatically loaded into a Python-based design software, which automatically designed the contacts for the desired nanowire. By removing the native oxide with argon milling and evaporating Al, the contacts to the qubit island and ground plane were finalized, see Fig. 5.3(d). In the same fabrication step, the breaks in the ground plane, created when removing the shorts, were also connected, as seen from Figs. 5.3(a)–(c).

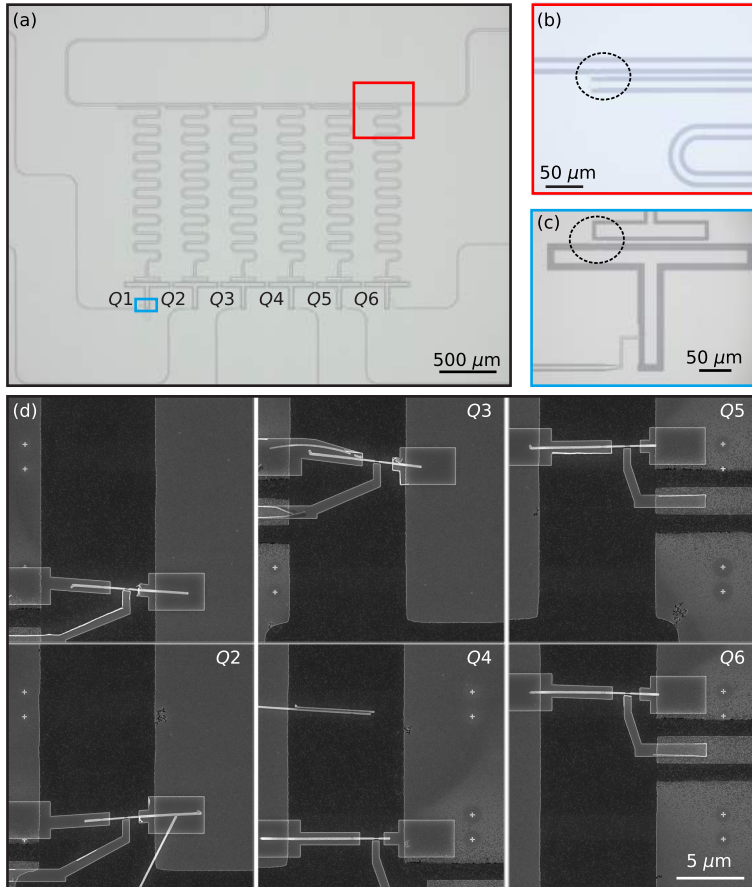


Figure 5.3: Device overview of the finished DEP qubit device. (a) Optical image of a device chip after the nanowire fabrication process. Josephson junctions were formed by etching a segment of the Al shell of each nanowire. In the etching step, the connection shorting the transmission line and the readout resonators was removed, with one example highlighted [red rectangle magnified in (b), dashed circle]. Similarly, the connection between the islands and the resonators was removed, with one example highlighted [blue rectangle magnified in (c), dashed circle]. (d) Scanning electron micrographs of the six nanowires used to form Josephson junction. After etching the Al shell, each side of the junction was connected to the ground plane and qubit island, respectively, which finalized the qubit circuit. In this step, the side gates were also defined. Q1–Q6 refers to the qubits from left to right in (a).

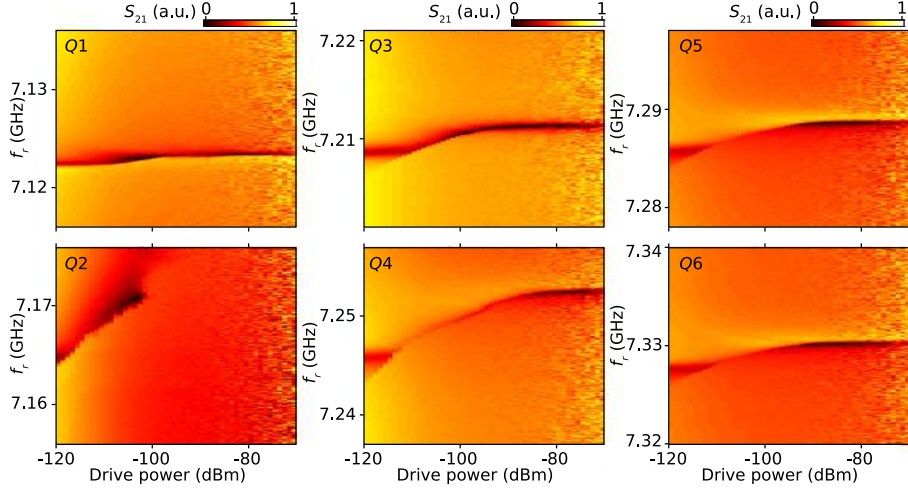


Figure 5.4: Power scans at zero junction gate V_Q . Transmission amplitude S_{21} as a function of resonator drive frequency f_r and drive power. All six qubits Q1–Q6 show a dispersive shift, indicating the desired gatemon qubit behavior.

5.3 QUBIT MEASUREMENTS

Measurements were performed by probing each of the six readout resonators by transmission measurements. We investigated the power dependence of each resonator, as shown in Fig. 5.4. Here, we observe that each resonator shows a dispersive shift for reducing powers, as expected for a coupled qubit-resonator cQED system according to the theory discussed in Chapter 2. Therefore, we can conclude that all six qubits were successfully fabricated, and behaves like usual gatemons. To further investigate the performance of these qubits, we performed time domain measurements. The qubits are driven by the six individual gate lines, which are shown in Fig. 5.3(a). These lines are also used to tune the DC voltage, and thereby to change the qubit frequency. We locate all the qubits in frequency space with two-tone spectroscopy, where a drive tone is applied via the individual gate lines. Following the drive tone a second readout tone is applied to the transmission line, probing the resonator frequency, from which we infer the qubit state. By varying the junction gate voltage V_Q , we move all qubits to frequencies of around 5.5 GHz (not simultaneously as they are coupled). Here, we perform T_1 lifetime measurements.

By applying a π -pulse, followed by a variable wait time τ , we observe the characteristic exponential population decay from the excited to the ground state (top row of Fig. 5.5). Fits to a decaying exponent allow extraction of the characteristic decay times T_1 , yielding values of 1–5 μs , which is comparable to typical values obtained from traditional gatemon devices.

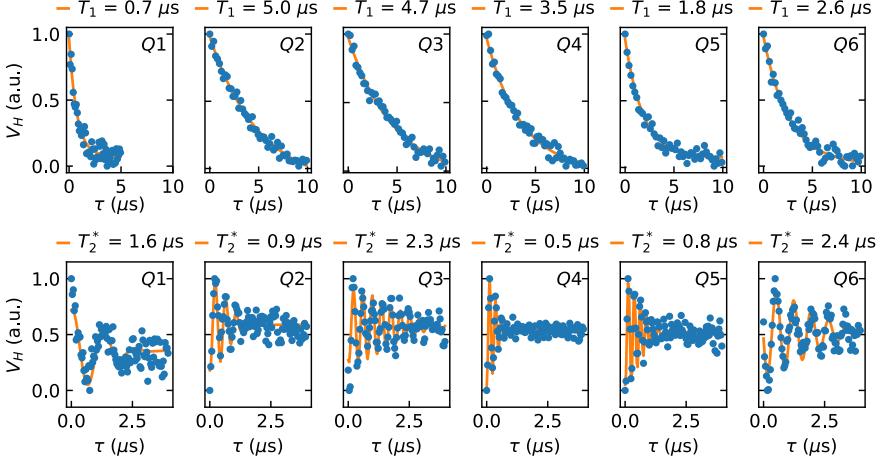


Figure 5.5: Coherence of DEP assembled qubit devices. Top row: T_1 lifetime measurements of Q1–Q6 performed by varying the wait time τ after applying a π -pulse. The V_H measurements (blue data points) are fitted to a decaying exponent (orange curve) to extract the relaxation time T_1 . Bottom row: T_2^* Ramsey measurements of Q1–Q6 performed by varying the wait time τ between two $\pi/2$ -pulses. The V_H measurements (blue data points) are fitted to a exponentially decaying sinusoid (orange curve) to extract the decoherence time T_2^* .

We next probe the coherence times T_2^* of the devices by performing Ramsey measurements. Here, a slightly detuned $\pi/2$ -pulse is applied, which brings the qubit state to the equator of the Bloch sphere. Due to the slight detuning, the state vector processes with this detuned frequency (as discussed in Section 2.4). Due to decoherence, the state probability will oscillate within a decaying envelope. These measurements are shown in the bottom row of Fig. 5.5. Fits to an exponential decaying sinusoid ($V_H(\tau) = A \exp(-(\tau/T_2^*)^2) \sin(\omega\tau + \phi) + B$) allow extraction of T_2^* ranging from 0.5–2.5 μs , similar to usual gatemon experiments.

5.4 CONCLUSIONS

In summary, we have demonstrated the successful fabrication of gatemon multi-qubit devices by deterministic dielectrophoretic assembly. Each qubit of our six qubit devices yield comparable characteristics and performance as previous gatemon devices. In addition, this technique may scale to larger multi-qubit devices without additional complexity. Future work improving the nanowire placement yield at the individual sites and the integration of image recognition techniques may see this process becoming fully automatic.

6

Controlled DC Monitoring of a Superconducting Qubit

Creating a transmon qubit using semiconductor-superconductor hybrid materials not only provides electrostatic control of the qubit frequency, it also allows parts of the circuit to be electrically connected and disconnected *in situ* by operating a semiconductor region of the device as a field-effect transistor. Here, we exploit this feature to compare *in the same device* characteristics of the qubit, such as frequency and relaxation time, with related transport properties such as critical supercurrent and normal-state resistance. Gradually opening the field-effect transistor to the monitoring circuit allows the influence of weak-to-strong DC monitoring of a “live” qubit to be measured. A model of this influence yields excellent agreement with experiment, demonstrating a relaxation rate mediated by a gate-controlled environmental coupling.

This chapter is adapted from Ref. [98]. Additional information on the device fabrication and the measurement setup is provided in Chapter 3.

This work was done in collaboration with T. W. Larsen, B. van Heck, D. Sabonis, O. Erlandsson, I. Petkovic, D. I. Pikulin, P. Krogstrup, K. D. Petersson, and C. M. Marcus.

6.1 INTRODUCTION

Josephson junctions (JJs) serve as key elements in a wide range of quantum systems of interest for fundamental explorations and technological applications. JJs, which provide the nonlinearity essential for superconducting qubits [55], are typically fabricated using insulating tunnel junctions between superconducting metals [46]. Alternative realizations using atomic contacts [105] or superconductor-semiconductor-superconductor (S-Sm-S) junctions [38, 39, 106] are receiving growing attention. Hybrid S-Sm-S JJs host a rich spectrum of new phenomena, including a modified current-phase relation (CPR) [56, 107] different from the sinusoidal CPR of metal-insulator-metal tunnel junctions. Other electrostatically tunable parameters include the sub-gap density of states (DOS), shunt resistance [49], spin-orbit coupling [125], and critical current [126].

In this Chapter, we investigate a modified S-Sm-S JJ design of a gatemon qubit that combines DC transport and coherent cQED qubit measurements. The device is realized in an InAs nanowire with a fully surrounding epitaxial Al shell by removing the Al layer in a second region (besides the JJ itself) allowing that region to function as a field-effect transistor (FET). By switching the FET between being conducting (“on”) or depleted (“off”) using a gate voltage, we are able to implement a controlled transition between the transport and cQED measurement configurations. We demonstrate that the additional tunability does not compromise the quality of the qubit in the cQED configuration, where the FET is off. We further demonstrate control of the qubit relaxation as the FET is turned on, continuously increasing the coupling of the junction to the environment, in agreement with a simple circuit model. Finally, we demonstrate strong correlation between cQED and transport data by comparing the measured qubit frequency spectrum with the switching current directly measured *in situ*.

Devices were fabricated on a high resistivity silicon substrate covered with a 20 nm NbTiN film. The nanowire region, qubit-capacitor island, electrostatic gates, on-chip gate filters, readout resonator, and transmission line were patterned by electron-beam lithography and defined by reactive-ion etching techniques, see Fig. 6.1(a). The full-shell InAs/Al epitaxial hybrid nanowire is placed at the bottom of the qubit island, see Fig. 6.1(b) [89]. Two gateable regions are formed by selective wet etching of the Al in two ~ 150 nm seg-

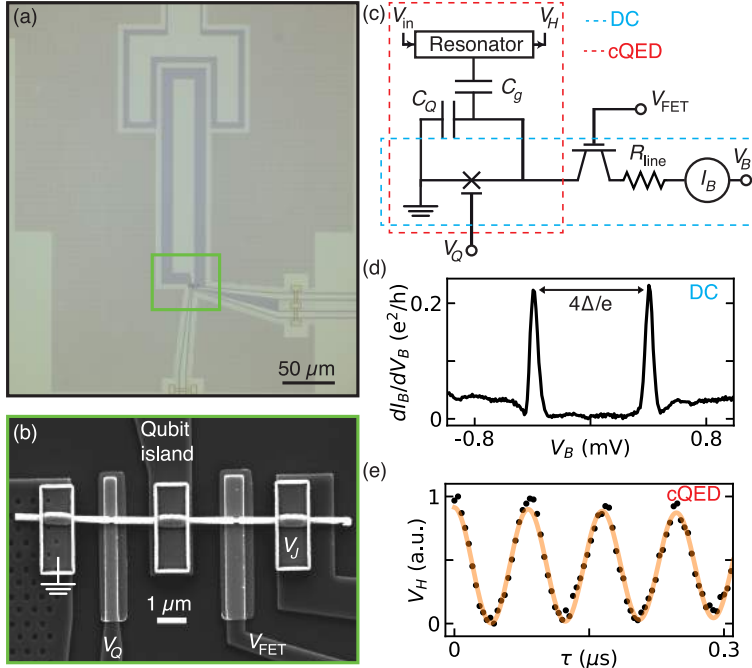


Figure 6.1: Device geometry and concept. (a) Optical micrograph of the modified gatemon qubit device showing the bottom of the readout resonator capacitively coupled to the qubit island. The island is contacted to a nanowire placed in the highlighted green square. (b) Scanning electron micrograph (SEM) of the nanowire in the green rectangle in (a). Two removed segments of the Al shell form the qubit JJ (125 nm) and the FET (175 nm), controlled by gates V_Q and V_{FET} . The bias voltage across the nanowire is indicated V_J . (c) Device circuit with FET off for cQED (dashed red box), and FET on allowing transport (dashed blue box). The bias voltage V_B refers to the total voltage drop across both the nanowire and line resistance R_{line} . (d) Differential conductance dI_B/dV_B as a function of bias voltage V_B shows the superconducting gap Δ of the qubit JJ, with $V_{\text{FET}} = +4$ V and $V_Q = -2.9$ V. (e) Rabi oscillations of the qubit seen in resonator output V_H as a function of drive time τ at $V_{\text{FET}} = -3$ V and $V_Q = -2.5$ V, with exponentially damped sinusoid (orange).

ments defined by electron-beam lithography, aligned with two independent bottom gates, which are separated from the nanowire by a 15-nm-thick HfO_2 dielectric. The three superconducting segments—ground, qubit island with capacitance C_Q , and DC bias V_J —are then contacted with ~ 200 nm sputtered

NbTiN, see Fig. 6.1(b). In this circuit, when the FET is on, DC current or voltage measurements are available [blue box in Fig. 6.1(c)]. Depleting the FET allows the device to operate as a qubit, where measurements of the heterodyne demodulated transmission V_H allow qubit state determination and V_Q allows tuning the qubit frequency f_{01} over several gigahertz [red box in Fig. 6.1(c)].

Setting the voltage on the FET gate to $V_{\text{FET}} = +4$ V, which turned the FET fully conducting, and the voltage on the qubit JJ to $V_Q = -2.9$ V makes the voltage drop predominantly across the qubit JJ. In this configuration, the differential conductance dI_B/dV_B , probes the convolution of the DOS on each side of the JJ, see Fig. 6.1(d). Keeping in mind a simple model of JJ spectroscopy [49], we interpret the distance between the two peaks in dI_B/dV_B as $4\Delta/e = 4 \times 190 \mu\text{V}$, where Δ is the induced superconducting gap. In the cQED configuration, with $V_{\text{FET}} = -3$ V and $V_Q = -2.5$ V, coherent Rabi oscillations are observed by varying the duration τ of the qubit drive tone at the qubit frequency $f_{01} = 4.6$ GHz. Following the drive tone, a second tone was applied at the readout resonator frequency, $f_R \sim 5.3$ GHz, to perform dispersive readout where V_H is measured, see Fig. 6.1(e). These experiments are carried out in a dilution refrigerator with a base temperature of ~ 10 mK using standard lock-in and DC techniques for the transport measurements and using heterodyne readout and demodulation techniques for the cQED measurements, see Section 6.5.

6.2 RELAXATION OF LEADED GATEMON QUBITS

Having demonstrated the ability to probe the qubit JJ with both transport and cQED techniques, we next compare performance to a nominally identical gatemon without the FET and extra DC lead. Scanning electron micrographs of the two devices are shown in Figs. 6.2(a, b). The measured relaxation times T_1 are shown for a range of qubit frequencies f_{01} , controlled by V_Q , in Fig. 6.2(c). Relaxation times T_1 were measured by applying a π -pulse, calibrated by a Rabi experiment at f_{01} , followed by a variable wait time τ before readout, see Fig. 6.2(c), inset. $T_1(V_Q)$ were then extracted by fitting $V_H(\tau)$ to a decaying exponential. We observe no systematic difference in T_1 between the devices, demonstrating that the addition of a transport lead does not compromise the performance in the cQED configuration.

We next monitored dI_B/dV_B , f_{01} , and T_1 as V_{FET} was varied from off

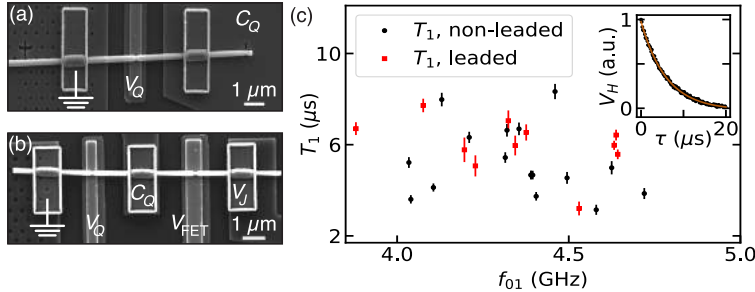


Figure 6.2: Comparison of a leaded vs a nonleaded gatemon device. (a) Scanning electron micrograph of a gatemon without transport lead. C_Q is the capacitance of the qubit island. (b) Same as (a) for gatemon with transport lead, with voltage bias V_J . (c) Qubit relaxation times T_1 of the gatemons as a function of qubit frequency, f_{01} . Both leaded (black circle) and nonleaded (red square) devices show similar T_1 times between 3–8 μ s, with comparable mean and standard deviation values. Inset: Relaxation time T_1 (black points) at $f_{01} = 4.6$ GHz for the leaded device as a function of wait time τ , with exponential fit (orange curve) yielding $T_1 = 6 \mu$ s. Error bars are estimated from fit uncertainties.

(cQED regime) to on (transport regime). Measurements of dI_B/dV_B [Fig. 6.3(a)] illustrate how the FET was turned conducting as V_{FET} was increased. Qubit frequency f_{01} was measured by two-tone spectroscopy, where a drive tone with varying frequency f_d was applied for 2 μ s, followed by a readout tone at f_R . A Lorentzian fit is used for each V_{FET} to extract f_{01} , see Fig. 6.3(b), insets. We attribute the weak dependence of f_{01} on V_{FET} to cross talk between the two gates.

Following each spectroscopy measurement, a T_1 measurement was immediately carried out, see Fig. 6.3(c), yielding a nearly gate independent $T_1 \sim 6 \mu$ s for $V_{FET} < -2$ V. At $V_{FET} \sim -2$ V, we observe a sudden drop in T_1 , followed by a short revival at $V_{FET} \sim -1.8$ V. We associate the revival in T_1 with the corresponding drop in dI_B/dV_B observed in Fig. 6.3(a). We attribute this non-monotonicity to the formation of quantum dots in the FET, which is commonly observed in nanowire JJs near the pinch-off values [108]. For $V_{FET} > -1.5$ V, f_{01} and T_1 can no longer be resolved, consistent with increasing dI_B/dV_B . We note that the dI_B/dV_B curve in Fig. 6.3(a) was shifted horizontally by a small amount (0.1 V) to align features in dI_B/dV_B with corresponding features in T_1 . This was done to account for gate drift, as the cQED and transport measurements

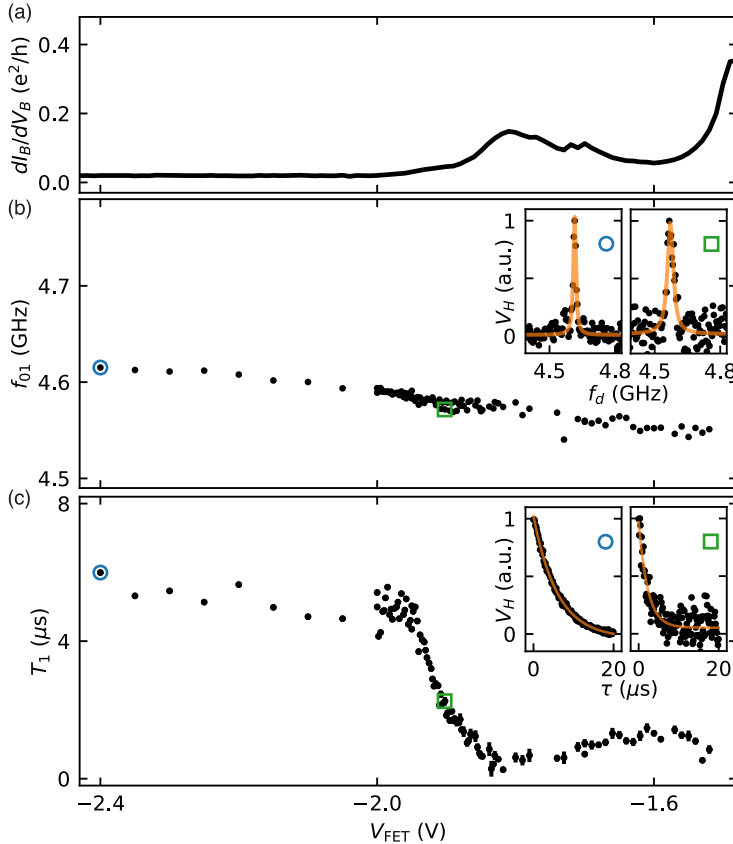


Figure 6.3: Qubit performance as a function of V_{FET} . (a) Differential conductance dI_B/dV_B as a function of FET gate voltage V_{FET} at high bias $V_B = 1.0$ mV, to approximate normal-state resistance. (b) Qubit frequency f_{01} as a function of V_{FET} using two-tone spectroscopy. Insets: Lorentzian fits (orange) to data points in the main panel as indicated by the corresponding markers (blue circle, green square). From each V_H we subtract the background and normalize to the maximal value. (c) Similar to (b) relaxation times T_1 from exponential fits (insets). Error bars are estimated from fit errors.

were performed sequentially over the course of several days.

We develop a circuit model of qubit relaxation in the leaded device. Within the model, the qubit circuit is coupled through the FET to a series resistance

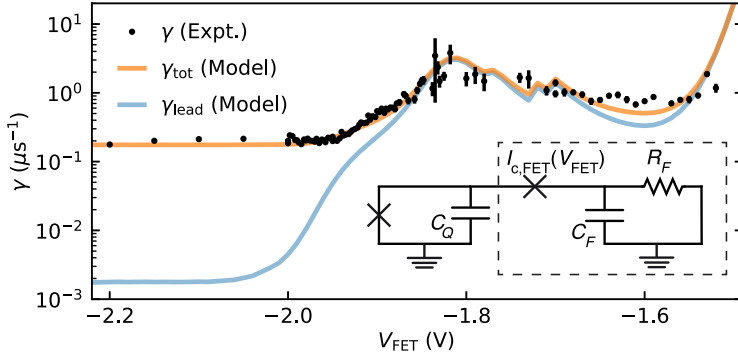


Figure 6.4: Circuit model of the relaxation rate. Relaxation rate $\gamma = 1/T_1$ (black circles) as a function of FET voltage, V_{FET} , by inverting the experimental data from Fig. 6.3(c). Model relaxation rates γ_{lead} due only to the transport lead (blue) and γ_{tot} (orange) including lead and nonlead contributions (see text). The circuit model is sketched in the inset where the qubit is coupled to the environment by an effective impedance, $Z_{\text{env}} = i\omega L_{\text{FET}} + (1/R_F + i\omega C_F)^{-1}$. The dashed rectangle indicates the environment circuit.

R_F and a parallel capacitance C_F representing an on-chip filter on the lead [86]. The coupling to the environment via the (superconducting) FET junction is modeled as a gate tunable Josephson inductance L_{FET} , giving a total environment impedance $Z_{\text{env}} = i\omega L_{\text{FET}} + (1/R_F + i\omega C_F)^{-1}$. This impedance can be viewed as a single dissipative element with resistance given by

$$R_{\text{env}} = 1/\text{Re}[Y_{\text{env}}] = L_{\text{FET}}^2 \left(R_F^2 C_F^2 \omega^4 + \omega^2 \right) / R_F + R_F \left(1 - 2L_{\text{FET}} C_F \omega^2 \right), \quad (6.1)$$

with admittance $Y_{\text{env}} = 1/Z_{\text{env}}$ [72]. The relaxation rate associated with the lead is given by $\gamma_{\text{lead}} = 1/R_{\text{env}} C_Q$, yielding a total decay rate $\gamma_{\text{tot}} = \gamma_{\text{nonleaded}} + \gamma_{\text{lead}}$, where $\gamma_{\text{nonleaded}}$ is the decay rate associated with relaxation unrelated to the lead.

We estimate $L_{\text{FET}} = \hbar/2eI_{c,\text{FET}}$ [51], where $I_{c,\text{FET}}$ is the critical current of the FET, which we in turn relate to the normal-state resistance $R_{n,\text{FET}}$ via the relation $I_{c,\text{FET}}R_{n,\text{FET}} = \pi\Delta/2e$ [127], yielding

$$L_{\text{FET}} = \hbar R_{n,\text{FET}} / \pi\Delta. \quad (6.2)$$

$R_{n,\text{FET}}$ can be found from dI_B/dV_B in Fig. 6.3(a) by subtracting the voltage drop across the line resistance, $R_{\text{line}} = 57 \text{ k}\Omega$, and assuming no voltage drop across the qubit JJ, justified by $I_{c,\text{FET}} < I_c$, where I_c is the critical current of the qubit JJ. From electrostatic simulations we estimate $C_Q = 38 \text{ fF}$ [87]. We take $\omega = 2\pi\overline{f_{01}}$, where $\overline{f_{01}} = 4.6 \text{ GHz}$ is the average f_{01} in Fig. 6.3(b), and $\Delta = 190 \mu\text{eV}$ from Fig. 6.1(d). Combining Eqs. (6.1) and (6.2) with the measured $1/T_1$ yields the γ_{lead} in Fig. 6.4 using $R_F = R_{\text{line}}$ and $C_F = 0.1 \text{ pF}$ as the best fit parameter. We note that electrostatic simulations give $C_F \sim 0.5 \text{ pF}$, in reasonable agreement with the best fit value. We define $\gamma_{\text{nonleaded}} = 1/T_1^{\text{mean}}$, where $T_1^{\text{mean}} = 5.8 \mu\text{s}$ is the mean value of the T_1 at $V_{\text{FET}} < -2 \text{ V}$. Using this estimate for $\gamma_{\text{nonleaded}}$, we calculate the total relaxation time based on the transport data (orange line in Fig. 6.4), showing excellent agreement with the measured values. The T_1 limit based on the contribution of the lead saturates at $T_1^{\text{lead}} = 1/\gamma_{\text{lead}} \sim 1 \text{ ms}$, indicating that leaded gatemon devices can accommodate large improvements in gatemon relaxation times. We mainly attribute the current level of relaxation times to dielectric losses. This is based on measurements of test resonators from the same substrates yielding quality factors of $Q \sim 10^5$, with $T_1 \sim Q/(2\pi f_{01})$ being roughly consistent with the observed T_1 . Although optimizing the qubit lifetime is beyond the scope of this experiment, we are optimistic that these devices can reach similar coherence times as conventional superconducting qubits based on recent experiments of similar devices reaching T_1 times of $\sim 20 \mu\text{s}$ [62] and the promising upper limit on T_1 of the model in Fig. 6.4.

6.3 CORRELATION OF DC AND cQED MEASUREMENTS

Combining transport and cQED measurements allows for the correlation between critical current $I_c(V_Q)$ and $f_{01}(V_Q)$ to be observed directly [128]. The critical current I_c is extracted from dI_B/dV_B and I_B while sweeping V_B and V_Q . We extract the voltage drop and differential resistance across the qubit junction, V_J and dV_J/dI_B , by inverting dI_B/dV_B and subtracting R_{line} . In doing this, we assume that there is no voltage drop across the FET junction, since $I_c < I_{c,\text{FET}}$. The qubit resonance f_{01} is measured over the same V_Q range using two-tone spectroscopy, see Fig. 6.5(b). We note that the two-photon transition to the next harmonic is also observed for some V_Q , visible at a slightly lower frequency than f_{01} , given by the anharmonicity.

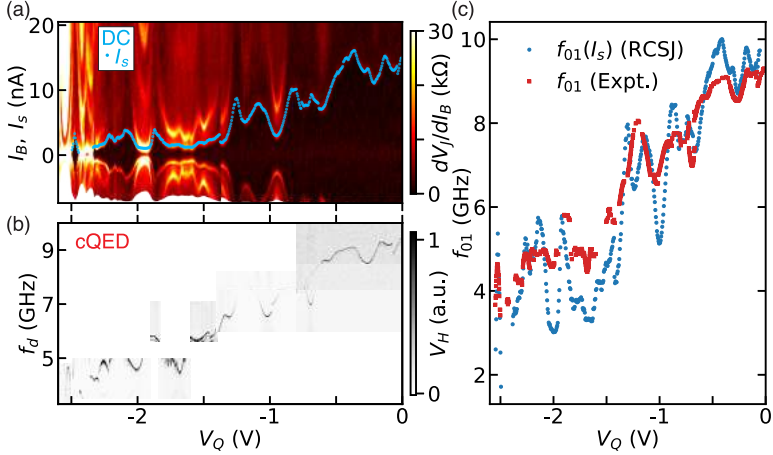


Figure 6.5: Comparison of DC and cQED measurements. (a) Differential resistance of the qubit JJ, dV_J/dI_B , as a function of current bias I_B and qubit gate voltage V_Q . Switching current I_s (blue points) from the edge of the zero-resistance state for increasing sweep at $V_{\text{FET}} = +4$ V to turn the FET conducting. (b) Qubit frequency f_{01} from two-tone spectroscopy as a function of V_Q , acquired at $V_{\text{FET}} = -3$ V to deplete the FET. The area of missing data at 5.0–5.6 GHz is due to f_{01} crossing the resonator frequency, f_R . (c) Correlation between transport and cQED data. f_{01} from (b) (red) extracted as in Fig. 6.3(b), inset. f_{01} from I_c (blue) extracted by applying an RCSJ model to the data in (a) (see text).

The relation between the two measurements is shown in Fig. 6.5(c). In order to estimate $I_c(V_Q)$, we first extract the switching current $I_s(V_Q)$ from the data, taken as the I_B at which dV_J/dI_B is maximal, while sweeping I_B from negative to positive values [blue dots in Fig. 6.5(a)]. Bright features at high bias ($I_B > I_s$) are likely associated with multiple Andreev reflection [129]. To extract I_c from the measured I_s , we model the qubit as an underdamped RCSJ (resistively and capacitively shunted junction) Josephson junction with a sinusoidal current-phase relation $I = I_c \sin \phi$. Furthermore, we note the small difference between the return current I_r (same definition as I_s at negative I_B) is slightly smaller than I_s , see Section 6.6. In this case, I_s corresponds to the current of equal stability between the resistive and nonresistive state [130]. Under this condition, and for large quality factors, $Q \gg 1$, the ratio I_s/I_c

depends on quality factor $Q = R\sqrt{2eI_cC_Q/\hbar}$ as

$$I_s/I_c = (2 + 4/\pi)Q^{-1} + (2 + \pi)Q^{-2}, \quad (6.3)$$

where $R = (1/R_J + 1/R_{\text{line}})^{-1}$ and R_J is the shunt resistance [130]. In RCSJ theory R_J is proportional to the normal-state resistance of the junction R_N [49] with the proportionality depending on both the size of and DOS inside the proximitized superconducting gap and temperature. As these parameters are not simultaneously accessible in our setup, we take the proportionality as a fit parameter. By doing so, we find R_J to be equal to R_N . We then apply the Ambegaokar-Baratoff relation $I_cR_J = \pi\Delta/2e$ [127], which allows us to extract I_c by inverting Eq. (6.3) numerically*. The extracted I_c , in turn, yield values for Q in the range 10–20, consistent with our initial assumptions. For these values of Q , the RCSJ model takes the electron temperature to be $> 50 \text{ mK}$ to account for the weak asymmetry in I_s and I_r , see Section 6.6. Finally, we relate I_c to f_{01} by using the numerical solution of the standard transmon Hamiltonian, $H = 4E_C(n - n_g)^2 - E_J \cos(\phi)$ [30], with $E_J = \hbar I_c/2e$ and $E_C/h = e^2/2hC_Q = 512 \text{ MHz}$, at the charge degeneracy point with offset charge $n_g = 0.5$.

A comparison of the measured and estimated f_{01} is shown in Fig. 6.5(c). The model (RCSJ) curve is shifted horizontally by 0.05 V to align the features at $\sim -2.5 \text{ V}$ and can be attributed to cross talk between the two gates as V_{FET} is varied from the DC to the cQED configuration, consistent with independent calibration measurements. A clear correlation is observed between the two measurement techniques, especially evident from the matching of local minima and maxima of both spectra and the overall agreement of the absolute values. We attribute the residual quantitative discrepancy to the simplifying assumptions used to determine the shunt resistance of the RCSJ model, which likely do not capture the possible gate dependence of the subgap DOS of the qubit JJ. In addition, the assumption of sinusoidal CPR will break down as the qubit JJ is opened due to increasing mode transmission in the semiconductor junction, leading to small overshoots of the model as perhaps seen around $V_Q \sim 0 \text{ V}$.

*Numerical code and data accompanying the analysis of Fig. 6.5(c) is found at:
https://github.com/anderskringhoej/dc_qubit.

6.4 CONCLUSIONS

In summary, we have demonstrated the compatibility of DC transport and cQED measurement techniques in gatemon qubits. This method may extend to other material platforms such as two-dimensional electron gases [40] or graphene [41, 42, 128]. Furthermore, we achieve a controllable relaxation rate potentially relevant for a range of qubit applications such as tunable coupling schemes [131, 132] and controlled qubit relaxation and reset protocols [133, 134]. In addition, we have demonstrated clear correlation between DC transport and cQED measurements motivating future extensions, such as studying CPRs [107] or probing channel transmissions by studying multiple Andreev reflections [113] combined with cQED experiments [69, 101, 125]. Combining well-established transport techniques in quantum dot physics with qubit geometries may also be an interesting research direction [135]. Potentially, this geometry is also a promising platform to coherently probe Majorana zero modes in cQED measurements [44], as transport signatures have been demonstrated, both in half-shell nanowires [43] and full-shell wires [136, 137].

6.5 EXPERIMENTAL SETUP

The measurements presented in this Chapter are conducted in a cryogen-free dilution refrigerator with a base temperature of $\sim 10\text{ mK}$. A detailed schematic of the electronic setup is shown in Fig. 6.6. The sample is mounted to a Cu circuit board located in a indium sealed CuBe box mounted inside another Cu box, which is thermally attached to the mixing chamber plate. DC lines (blue lines in Fig. 6.6) connect to the sample through a loom heavily filtered at frequencies above 80 MHz via both the QDevil and the LFCN-80 low pass filters. For transport measurements we measure a small AC current using the SR860 lock-in amplifier while also measuring the DC current to ground with the Keysight multimeter. Both current signals are amplified and converted to a voltage by the Basel SP983 I-to-V converter.

Two microwave coaxial drive lines connect to the sample (red lines in Fig. 6.6). The combined input signal is generated by two RF sources and is heavily attenuated and filtered above 10 GHz with a K&L low pass filter. These two signals are used for qubit drive and readout drive, respectively. The output signal is again filtered and amplified at the 4 K stage with a cryogenic

low noise amplifier with a bandwidth of 4–8 GHz with further amplification at room temperature using the Miteq amplifier. The output signal is down converted to an intermediate frequency by mixing with a local oscillator and filtering of the high frequency component. After another amplification stage using the SR445A amplifier, the intermediate frequency signal is digitized and digitally down converted in order to extract the in-phase and quadrature components of the readout signal.

The SR FS725 10 MHz clock reference is connected to the Alazar card, signal generators and the AWG for synchronisation of the microwave signals. Further experimental details are found in Chapter 3.

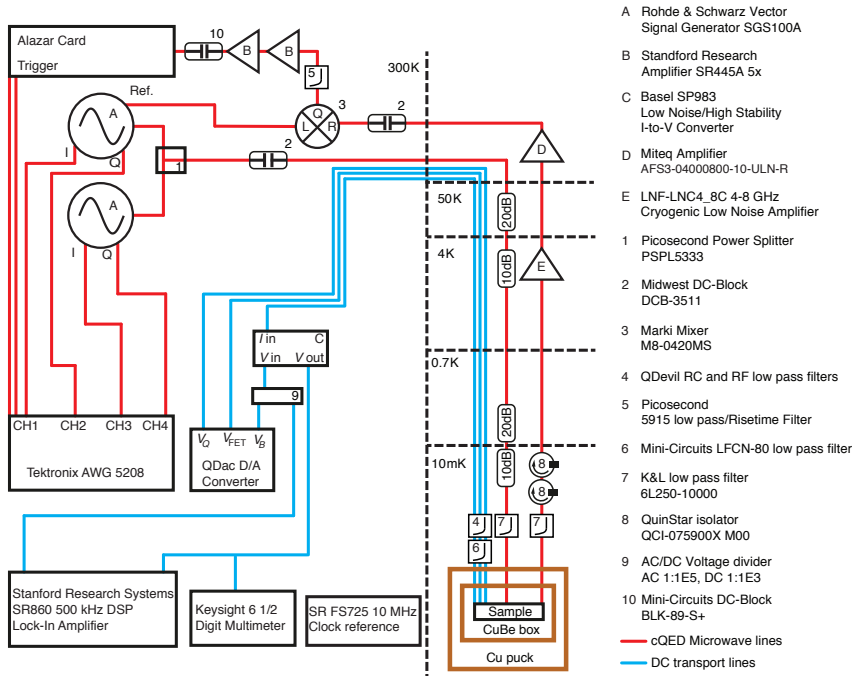


Figure 6.6: Schematic of the setup. Blue lines refer to lines used for the DC transport and red lines are the microwave drive lines used for qubit manipulation and readout. The signal generators, AWG, and Alazar card are all connected to the SR FS725 10 MHz clock reference for synchronisation.

6.6 RCSJ MODELLING DETAILS AND ADDITIONAL TRANSPORT DATA

To supplement the data and the analysis presented in Fig. 6.5, we measured dV_J/dI_B as a function of I_B and V_Q for a I_B -range where we were able to extract both I_s and I_r for the entire V_Q -range, see Fig. 6.7(a). This dataset shows quantitatively almost the same features as the dataset in Fig. 6.5(a). However, due to a larger amount of drift, possibly due to longer acquisition time, we use the dataset in Fig. 6.5(a) to perform the modelling in Fig. 6.5(c). From the measurement shown in Fig. 6.7(a) we are able to extract both I_s and I_r , see Fig. 6.7(b). Here we observe a weak asymmetry between I_r and I_s for the full V_Q -range, which justifies the use of the RCSJ model applied in the analysis of Fig. 6.5(c).

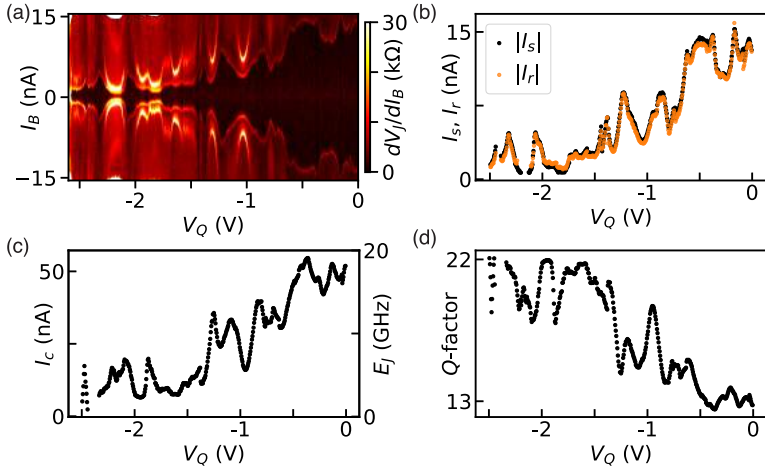


Figure 6.7: Supporting transport measurements. (a) DC transport measurement of dV_J/dI_B as a function of I_B and V_Q , acquired in the same way as the data presented in Fig. 6.5(a). In this measurement, both the transition to a non-resistive state at negative I_B -values and the transition to the resistive state at positive I_B -values are observed. (b) Absolute values of the extracted return current I_r and switching current as a function of V_Q , illustrating the weak asymmetry in their values. (c) Extracted critical current I_c (left y-axis, converted to $E_J = \hbar I_c / 2e$ on the right y-axis). (d) Extracted quality factor Q from the numerical solutions to Eq. 3.

In addition, we compute the extracted critical current I_c and $E_J = \hbar I_c / 2e$ used in our RCSJ analysis, as shown in Fig. 6.7(c). Based on these E_J -values we estimate the electron temperature T to be $> 50\text{mK}$, such that the $k_B T/E_J$ -ratios

account for the weak asymmetry between I_r and I_s [130]. To further justify the application of the $Q \gg 1$ limit, we numerically extract the Q -values, as shown in Fig. 6.7(d).

7

Suppressed Charge Dispersion via Resonant Tunneling in a Single-Channel Transmon

We demonstrate strong suppression of charge dispersion in a semiconductor-based transmon qubit across Josephson resonances associated with a quantum dot in the junction. On resonance, dispersion is drastically reduced compared to conventional transmons with corresponding Josephson and charging energies. We develop a model of qubit dispersion for a single-channel resonance, which is in quantitative agreement with experimental data.

This chapter is adapted from Ref. [118]. The published content is supplemented with an additional discussion of the applied model in Chapter 2. Additional information on the device fabrication and the measurement setup is provided in Chapter 3.

This work was done in collaboration with B. van Heck, T. W. Larsen, O. Erlandsson, D. Sabonis, P. Krogstrup, L. Casparis, K. D. Petersson, and C. M. Marcus.

7.1 INTRODUCTION

Superconducting circuits based on nonlinear Josephson junctions (JJ) form the basis of a broad array of coherent quantum devices used in applications ranging from radiation detectors to magnetometers to qubits [51, 138]. An important application is the transmon qubit, a variant of the Cooper pair box qubit [24] where the Josephson energy, E_J , of the junction exceeds the charging energy, $E_C = e^2/2C$, of the shunting capacitor with capacitance C . Designing qubits with ratio E_J/E_C considerably greater than unity exponentially suppresses its charge character, correspondingly reducing its sensitivity to voltage noise and dramatically extending coherence [30, 58]. The trade-off with increasing E_J/E_C is reduced anharmonicity, which determines the minimal operation time due to leakage out of computational states [59].

The JJs used in superconducting qubits are almost exclusively based on superconductor-insulator-superconductor (SIS) tunnel junctions [46], well described by a sinusoidal current-phase relation (CPR) [56]. More recently, gate-voltage-tunable transmon qubits (gatemons) have been realized using superconductor-semiconductor-superconductor (S-Sm-S) JJs, where the Sm weak link was either a nanowire [38, 39], a two-dimensional electron gas [40] or graphene [41, 42]. Such Sm weak links are typically quasiballistic, and, with Andreev processes [109] across the junction dominated by a small number of highly transmitting channels [101, 107, 113]. In this regime, the CPR is no longer sinusoidal, and anharmonicity deviates from the usual relations and tradeoffs involving E_J and E_C [101].

An expected consequence of large transmission among a few Andreev modes in the JJ is a suppression of the quantization of island charge, which vanishes entirely when the transmission of any mode reaches unity [139–141]. Suppression of charge quantization in non-superconducting quantum dots has been well investigated experimentally [142, 143], including a recent detailed study in a semiconductor quantum dot with vanishing level spacing due to an internal normal-metal contact [117]. In a similar fashion, charge quantization on a JJ-coupled superconducting island is expected to be suppressed for highly transmissive modes and vanish for unity transmission of a mode [66], irrespective of the ratio E_J/E_C , though to our knowledge this has not been previously investigated experimentally.

In this Chapter, we investigate the charge dispersion in a nanowire-based

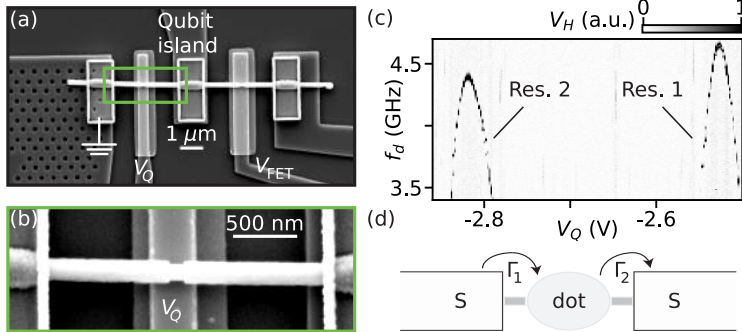


Figure 7.1: Device geometry and spectroscopy close to pinch-off. (a) Scanning electron micrograph (SEM) of the nanowire region of the qubit device. Two etched regions were formed (qubit junction and FET) controlled with bottom gates V_Q and V_{FET} . (b) SEM of the qubit region highlighted (green square) in (a). (c) Two-tone spectroscopy measurements of the heterodyne transmission voltage V_H at values of qubit gate voltage V_Q just above complete depletion of the qubit junction and varying drive frequency f_d , yielding two resonances (Res. 1 and Res. 2) in the qubit frequency spectrum. (d) Sketch illustrating the principle of tunneling on and off a resonant dot level inside a Josephson junction connected to the superconducting leads by two tunnel barriers, characterized by tunnel rates Γ_1 and Γ_2 .

gatemon qubit which shows strong suppression compared to a conventional metallic transmon qubit, when operated across resonances in the junction. As discussed below, resonances in the semiconductor JJ effectively bring the Andreev transmission of a single mode close to unity. A comparison of experimental data to a simple model describing resonant Cooper pair transport across a single-mode junction [56, 144–146] yields striking agreement, supporting both the general feature of suppressed charge quantization at large transmission, and the additional feature that a dot resonance acts to provide an effective near-unity transmission of a single mode in a semiconductor JJ.

Measurements were performed on a gatemon qubit based on an InAs nanowire fully covered by 30 nm epitaxial Al [89], as described previously [98]. Two ~ 150 nm segments of the Al shell were etched, forming gateable regions, as shown in Fig. 7.1(a), one serving as the qubit junction, controlled by gate voltage V_Q , and the other as a field-effect transistor (FET), allowing *in-situ* DC transport, controlled by V_{FET} [98]. All cQED measurements were carried out with the FET fully depleted ($V_{\text{FET}} = -3$ V), so that the gatemon circuit

consisted of one side of the qubit junction contacted to ground and the other to the capacitor island [Fig. 7.1(b)]. The island capacitance was designed to yield $E_C/h \sim 500$ MHz, allowing operation at intermediate $E_J/E_C \sim 10\text{--}20$ so that charge dispersion was easily resolved.

Near the pinch-off voltage of the qubit junction ($V_Q \sim -3$ V), the first visible features to appear in two-tone spectroscopy as V_Q was tuned more positive were two narrow peaks in the qubit frequency, as shown in Fig. 7.1(c). We attribute these features to resonant tunneling of Cooper pairs through an accidental quantum dot formed in the junction [Fig. 7.1(d)], a common occurrence near full depletion [108, 147]. Corresponding resonant features were also observed in DC transport (FET opened) at similar values of V_Q , see Section 7.7.

7.2 RESONANT TUNNELING MODEL

To model the junction resonance, we consider a single spin-degenerate level at energy ϵ_r , weakly coupled to the two superconducting leads via tunneling rates Γ_1 and Γ_2 [Fig. 7.2(a)], and a Breit-Wigner form for the transmission [148], $T = 4\Gamma_1\Gamma_2/(\epsilon_r^2 + \Gamma^2)$, where $\Gamma = \Gamma_1 + \Gamma_2$. Transmission is maximal on resonance, $\epsilon_r = 0$, where it reaches unity for symmetric barriers, $\Gamma_1 = \Gamma_2$ [Fig. 7.2(b)]. In the superconducting state, a pair of spin-degenerate Andreev bound states reside in the junction at energy E , given by [56, 145]

$$\begin{aligned} 2\sqrt{\Delta^2 - E^2}E^2\Gamma + (\Delta^2 - E^2)(E^2 - \epsilon_r^2 - \Gamma^2) \\ + 4\Delta^2\Gamma_1\Gamma_2\sin^2(\phi/2) = 0 \end{aligned} \quad (7.1)$$

where Δ the superconducting gap and ϕ the phase difference across the junction, as plotted in Fig. 7.2(c), see Section 7.6.

The Andreev level spectrum consists of a spin-degenerate, phase-dependent bound state plus a continuum of quasiparticle states above the gap. At $\phi = 0$, the bound state energy $E(0) = \tilde{\Delta}$, varies between ϵ_r and Δ as Γ increases, see Section 7.6. The energy gap at $\phi = \pi$ is proportional to the reflection amplitude $r = \sqrt{1 - T}$ and thus vanishes at perfect transmission, yielding two decoupled 4π -periodic branches.

We model the charging-energy-induced quantum fluctuations in ϕ via the

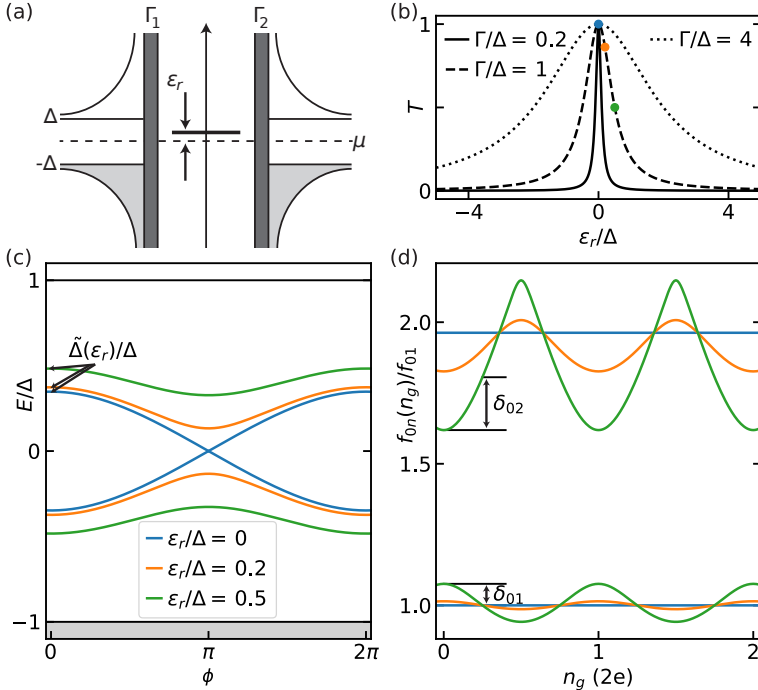


Figure 7.2: Resonant tunneling model. (a) Sketch of the energy density of states of a superconductor-dot-superconductor system. The superconductors are described by a standard BCS density of states with gap Δ . A spin-degenerate level is located inside the JJ, detuned by ϵ_r from the Fermi level (dashed line). (b) Normal state transmission through the junction, T , as a function of ϵ_r for three different Γ for $\Gamma_1 = \Gamma_2$. Note that $T = 1$ occurs for $\epsilon_r = 0$ for all Γ . (c) Numerical solutions to Eq. (7.1) describing resonant tunneling for three different ϵ_r [coloured dots in (a)] and $\Gamma/\Delta = 1$. The effective gap $\tilde{\Delta}(\epsilon_r) = E(0)$ (arrows) and continuum at $\pm E/\Delta = 1$ (grey and white region) are indicated. (d) Numerical solutions to Eq. (7.2) showing two lowest transition frequencies $f_{01}(n_g)$ and $f_{02}(n_g)$ as a function of offset charge n_g . The frequencies are normalized to the $0 \rightarrow 1$ degeneracy transition frequency $f_{01}(0.25) = f_{01}$ with dispersion amplitudes $\delta_{01} = f_{01}(0) - f_{01}(0.25)$ and $\delta_{02} = f_{02}(0.25) - f_{02}(0)$ indicated (arrows).

Hamiltonian [65, 149, 150],

$$H = 4E_C (i\partial_\phi - n_g)^2 + H_J, \quad (7.2a)$$

$$H_J = \tilde{\Delta} \begin{bmatrix} \cos(\phi/2) & r \sin(\phi/2) \\ r \sin(\phi/2) & -\cos(\phi/2) \end{bmatrix}, \quad (7.2b)$$

where n_g is the charge induced on the island in units of $2e$. The model above was originally derived for a superconducting quantum point contact [65], and it is valid provided $E_C \ll \Delta$ and that the Andreev energies are well separated from the continuum. The eigenvalues of H_J ,

$$E = \pm \tilde{\Delta} [1 - T \sin^2(\phi/2)]^{1/2}, \quad (7.3)$$

closely approximate the solutions of Eq. (7.1), see Section 7.6. We solve Eq. (7.2) numerically (Section 7.6) to obtain the qubit energy levels E_n as well as the associated transition frequencies $f_{nm}(n_g) = (E_m(n_g) - E_n(n_g))/\hbar$ [Fig. 7.2(d)].

A key feature of Eq. (7.2) is that it captures the Landau-Zener dynamics across the avoided crossing at $\phi = \pi$, which has a dramatic effect on charge dispersion of the qubit energy levels [66]. Indeed, the charge dispersion is determined by the 2π -tunneling amplitude of the phase below the Josephson potential energy barrier, which is suppressed by the probability of a diabatic passage to the excited branch of the Andreev spectrum. This probability becomes large near perfect transmission, when $r \ll (E_C/\tilde{\Delta})^{1/2}$. At $r = 0$, the 2π -tunneling processes become forbidden, and the charge dispersion reaches a minimal value given by the amplitude for 4π -tunneling*. The remarkable flattening of the energy levels in this diabatic regime is illustrated in Fig. 7.2(d).

7.3 CHARGE DISPERSION MEASUREMENTS

Measurements of charge dispersion across Res. 1 in Fig. 7.1(c) were carried out by finely sweeping V_Q while performing two-tone spectroscopy using a rastered drive tone f_d followed by a readout tone at $f_R \sim 5.3$ GHz [Fig. 7.3(a)]. The fine sweep of V_Q served two purposes; it both tuned the junction across the resonance and incremented the charge n_g on the superconducting island, resulting in an oscillating pattern within a resonant envelope, appearing in the demodulated transmission voltage V_H [Fig. 7.3(a)]. The two counter-oscillating branches reflect fast quasiparticle poisoning of the island, which shifts the energy spectrum in Fig. 7.2(d) by half a period ($1e$) [58].

Qubit frequencies for both parity branches were extracted from the raw V_H data using double Lorentzian fits for each V_Q , allowing determination of the

*Due to the large area below the potential barrier for 4π -tunneling at perfect transmission, this residual dispersion can be estimated to be well below the experimentally achieved linewidth.

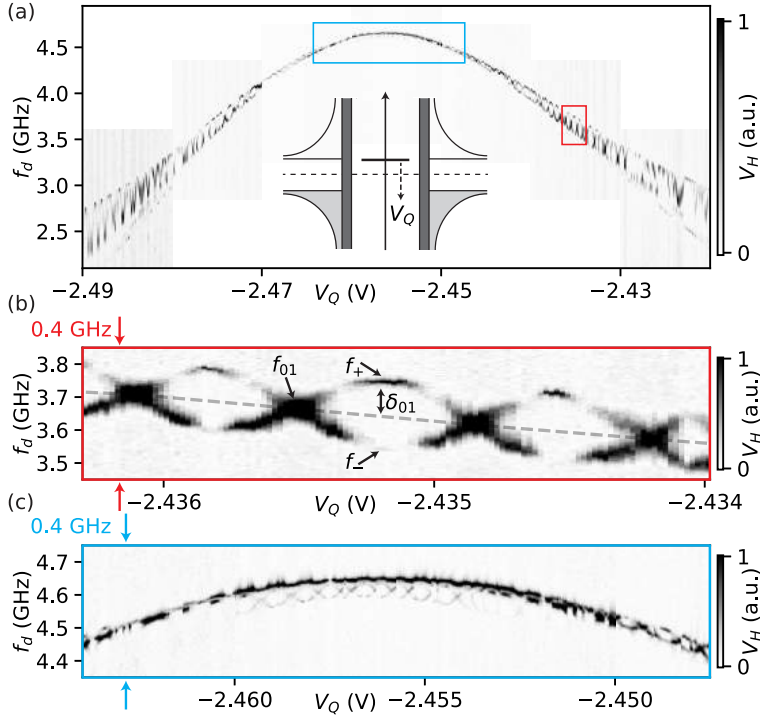


Figure 7.3: Charge dispersion measurements. (a) Measurement of the heterodyne transmission voltage V_H as a function of V_Q and a varying qubit drive f_d across one of two resonances (Res. 1). (Inset) Sketch of the energy density of states to illustrate the interpretation that ϵ_r is varied by V_Q . (b, c) Zoom at the red (blue) region in (a) at the slope (peak) of the resonance spectrum. Note the same f_d scale of 0.4 GHz in both panels. Examples of maximal upper (f_+), minimal lower (f_-), and charge degeneracy (f_{01}) frequencies are indicated in (b) (single arrows). An example of the maximal charge dispersion amplitude $\delta_{01} = f_+ - f_{01}$ is indicated (double arrow). Interpolated f_{01} as a function of V_Q is shown in (b) (grey dashed line).

maximal upper (f_+) and minimal lower (f_-) branch frequencies. At the charge degeneracy points a single Lorentzian fit was used to find f_{01} . The charge dispersion amplitude, here defined $\delta_{01} = f_+ - f_{01}$, was then extracted using an interpolated f_{01} to determine f_+ and f_{01} at corresponding V_Q , as shown in Fig. 7.3(b). Near the top of the resonance, the two-photon transition frequency $f_{02}(n_g)/2$ was visible in the spectrum and overlaps with the lower frequency

branch of the f_{01} transition [Fig. 7.3(c)]. As δ_{01} becomes comparable to the linewidth here we use the observed $f_{02}(n_g)/2$ to identify the V_Q associated with charge degeneracy and maximal dispersion amplitude.

Measurements of charge dispersion across Res. 2 were done in a slightly different way. Rather than using V_Q to span the resonance and vary n_g , for Res. 2, n_g was varied by sweeping V_{FET} (in the depleted regime) at fixed V_Q giving roughly independent control of ϵ_r and n_g , see Section 7.8. The observed behavior of Res. 1 and Res. 2 was the same.

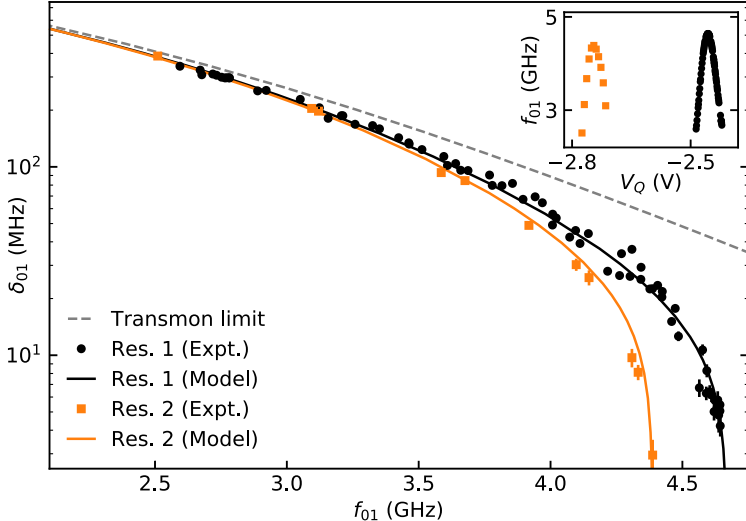


Figure 7.4: Extracted charge dispersion and model result. Extracted maximal dispersion amplitudes (black and orange data points) and fit results (black and orange curves) of the $0 \rightarrow 1$ transition for both resonances (Res. 1 and Res. 2) as a function of qubit frequency f_{01} . The theory curves are fits of numerical solutions to Eq. (7.2) with fit parameters $E_C/h = 539$ MHz and $\Gamma/h = 72$ (60) GHz for Res. 1 (2). Numerical δ_{01} (grey dashed line) for the standard transmon model with $E_C/h = 539$ MHz. Error bars are estimated from fit errors. (Inset) Extracted f_{01} as a function of V_Q for Res. 1 (black) and Res. 2 (orange).

Figure 7.4 shows a parametric plot of dispersion δ_{01} as a function of f_{01} for both resonances, with the original dependence of f_{01} on V_Q shown in the inset. As expected for transmons in general, δ_{01} decreases when f_{01} increases due to an increase in E_J . In the $f_{01} \lesssim 3.5$ GHz range, corresponding to the tails of the two resonances, δ_{01} decays approximately exponentially as f_{01} is increased.

However, for the $f_{01} \gtrsim 4\text{GHz}$ range, near the top of the two resonances, we observe the onset of a sharper decrease towards vanishing δ_{01} , strongly deviating from the exponential suppression expected in standard transmon qubits.

7.4 CHARGE DISPERSION ANALYSIS

To quantitatively compare the observed charge dispersion across the resonances to the model, Eq. (7.2), we first fix $\Delta = 190\text{ }\mu\text{eV}$ based on tunneling spectroscopy measurements at $V_{\text{FET}} = +4\text{ V}$, where the FET is open [98]. For simplicity we take the tunnel barriers to be symmetric and only allow V_Q to tune ϵ_r . We then fit E_C (the same for both resonances) and Γ (allowed to be different for each resonance). Results are shown in Fig. 7.4, with $E_C/h = 539\text{ MHz}$ (comparable to the electrostatic model [87] value 512 MHz) and $\Gamma/h = 72\text{ GHz}$ for Res. 1, and $\Gamma/h = 60\text{ GHz}$ for Res. 2.

Comparing δ_{01} to the prediction for a conventional transmon model based on the Hamiltonian $H_T = 4E_C(n - n_g)^2 - E_J \cos \phi$, for $E_C/h = 539\text{ MHz}$, highlights the suppressed dispersion observed experimentally and in the resonance model. The conventional model agrees with the experimental data and with the resonant level model only at low values of f_{01} , as expected for a decreasing transmission coefficient, where the sinusoidal CPR is recovered and the Landau-Zener dynamics becomes irrelevant.

When V_Q is turned more positive, we no longer observed narrow, symmetric resonances associated with resonant tunneling. Instead, we observe a non-monotonic spectrum much less susceptible to changes in V_Q . In this regime, we also observe a deviation in the charge dispersion compared to the value predicted by H_T , see Section 7.9. However, the suppression is not as pronounced as observed across the two resonances. We interpret this as crossing to a regime where the Andreev processes are no longer mediated by a resonant level and instead is described by a few gate tunable transmission coefficients [101, 106, 107, 113], not reaching values similarly close to unity.

We also examine charge dispersion for the two-photon ($0 \rightarrow 2$) transition frequencies of Res. 2. By increasing the power and repeating the scans used to extract δ_{01} we both excite the $0 \rightarrow 1$ and the $0 \rightarrow 2$ transitions. We define the $0 \rightarrow 2$ charge dispersion amplitude $\delta_{02} = f_{02} - f_{02,-}$, where $f_{02,-}$ and f_{02} are the minimal lower branch and degeneracy frequency, respectively. This operative

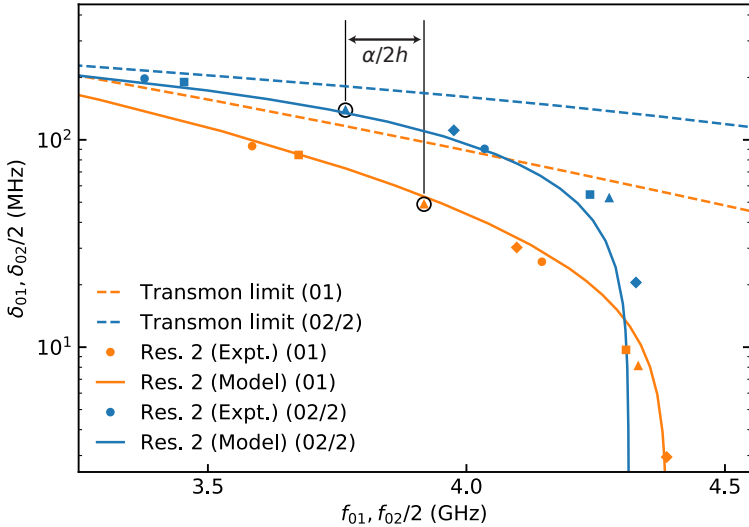


Figure 7.5: Charge dispersion of the $0 \rightarrow 2$ transition. Extracted maximal dispersion amplitudes (orange and blue data points) and fit result (orange and blue curves) of the $0 \rightarrow 1$ and $0 \rightarrow 2$ transitions of Res. 2, respectively. The theory curves correspond to numerical solutions to Eq. (7.2) with $E_C/h = 539$ MHz and $\Gamma/h = 60$ GHz. Numerical δ_{01} (orange dashed line) and $\delta_{02}/2$ (blue dashed line) based on H_T with $E_C/h = 539$ MHz. The frequency differences between corresponding pairs of data points taken at same V_Q (matching shapes) are equal to $\alpha/2$, with one example indicated.

definition is chosen as the upper branch of the $0 \rightarrow 2$ transition interferes with the lower branch of that of $0 \rightarrow 1$. Results for both δ_{01} and $\delta_{02}/2$ are shown in Fig. 7.5. Both theory curves are obtained by solving Eq. (7.2) for the same parameters as in Fig. 7.4, again showing striking agreement between theory and experiment. We also compare the measured $\delta_{02}/2$ with numerical solutions to H_T , again yielding roughly an order of magnitude deviation at resonance[†]. Finally, we emphasize that the finite frequency difference between the pairs of data points is equal to half the anharmonicity α , as $f_{02}/2 - f_{01} = 1/2(f_{12} - f_{01}) = \alpha/2h$. This illustrates that $\delta_{0i} \rightarrow 0$ can be achieved without $\alpha \rightarrow 0$ and in principle for much larger α .

Minor deviations between experiment and model may be attributed to

[†]Numerical code and data accompanying the analysis of Figs. 7.4 and 7.5 are found at: <https://github.com/anderskringhoej/Dispersion>.

effects of electron-electron interactions in the quantum dot, which are not included in the model [147, 151, 152] as well as fluctuations in the ratio Γ_1/Γ_2 as a function of V_Q .

7.5 CONCLUSIONS

In summary, we have observed and modeled the strong suppression of the charge dispersion in a single-channel transmon across a junction resonance, obtaining excellent agreement between experiment and theory. Our results suggest that charge dispersion can be suppressed without the necessity of large E_J/E_C ratios. Future implementation of controlled dot structures or QPC junctions to controllably achieve transmissions near unity may be a path to engineer superconducting qubits with vanishing charge dispersion and large anharmonicity. Additionally a controllable near-unity junction would allow for deterministic tuning of the spectrum in Andreev qubits [68, 69]. Similar results are presented in Ref. [120], in coordination with results reported here.

7.6 EXTENDED THEORY

This section gives an extended derivation of the applied theory. The theory is developed by Bernard van Heck, who also wrote the original version of this section.

7.6.1 DERIVATION OF THE BOUND STATE EQUATION

The bound state equation, Eq. (7.1), has been previously derived within a scattering matrix formalism [145]. For completeness, we present here an alternative derivation based on the tunneling Hamiltonian. Namely, we consider the following model of a Josephson junction with a resonant level coupling two s -wave superconductors,

$$H = H_0 + H_{\text{tunn}} , \quad (7.4a)$$

$$H_0 = \epsilon_r \sum_{\sigma} d_{\sigma}^{\dagger} d_{\sigma} + \sum_{\alpha n \sigma} E_{\alpha n} \Gamma_{\alpha n \sigma}^{\dagger} \Gamma_{\alpha n \sigma} , \quad (7.4b)$$

$$H_{\text{tunn}} = \sum_{\alpha} e^{-i\phi_{\alpha}/2} t_{\alpha} \sum_{n \sigma} [u_{\alpha n} d_{\sigma}^{\dagger} \Gamma_{\alpha n \sigma} + \sigma v_{\alpha n} d_{\sigma}^{\dagger} \Gamma_{\alpha n \bar{\sigma}}^{\dagger}] + \text{h.c.} \quad (7.4c)$$

Here, H_0 is the Hamiltonian in the absence of tunneling between the dot and the leads and H_{tunn} is the tunneling Hamiltonian; ϵ_r is the energy of the resonant level; $\alpha = 1, 2$ labels the two leads; n labels the orbitals in the two leads; σ labels spin; $\bar{\sigma} = -\sigma$; ϕ_α is the superconducting phase in lead α ; t_α is the tunneling strength between the dot and the lead α ; $u_{\alpha n}$ and $v_{\alpha n}$ are the BCS coherence factors for the quasiparticle states in the leads. We have assumed for simplicity that the tunneling strength is identical for every quasiparticle state in each lead, and that spin is a good quantum number.

The single-particle excitation energies of the Hamiltonian H are the positive energy solutions of the Bogoliubov-de Gennes equations $H_{\text{BdG}}\Psi = E\Psi$, derived by rewriting the Hamiltonian in Nambu (particle/hole) space. Here, $\Psi = (\Phi, \tilde{\Phi})$ is a Nambu wave function, and both Φ and $\tilde{\Phi}$ have components on the resonant level (which we will denote by $\Phi_0, \tilde{\Phi}_0$) as well as on the quasiparticle levels (which we will denote by $\Phi_{\alpha n}, \tilde{\Phi}_{\alpha n}$). The Bogoliubov-de Gennes equations are explicitly given by

$$\sum_{\alpha n} u_{\alpha n} t_\alpha e^{-i\phi_\alpha/2} \Phi_{\alpha n} + \sum_{\alpha n} v_{\alpha n} t_\alpha e^{-i\phi_\alpha/2} \tilde{\Phi}_{\alpha n} = (E - \epsilon_r) \Phi_0 \quad (7.5a)$$

$$u_{\alpha n} t_\alpha e^{i\phi_\alpha/2} \Phi_0 + v_{\alpha n} t_\alpha e^{-i\phi_\alpha/2} \tilde{\Phi}_0 = (E - \epsilon_r) \Phi_{\alpha n} \quad (7.5b)$$

$$-\sum_{\alpha n} u_{\alpha n} t_\alpha e^{i\phi_\alpha/2} \tilde{\Phi}_{\alpha n} + \sum_{\alpha n} v_{\alpha n} t_\alpha e^{i\phi_\alpha/2} \Phi_{\alpha n} = (E + \epsilon_r) \tilde{\Phi}_0 \quad (7.5c)$$

$$-u_{\alpha n} t_\alpha e^{-i\phi_\alpha/2} \tilde{\Phi}_0 + v_{\alpha n} t_\alpha e^{i\phi_\alpha/2} \Phi_0 = (E + \epsilon_r) \tilde{\Phi}_{\alpha n}. \quad (7.5d)$$

Note that the spin indices σ have been suppressed since they play a trivial role because spin is conserved by H . From Eq. (7.5b) and Eq. (7.5d), we can express the quasiparticle components in terms of $\Phi_0, \tilde{\Phi}_0$,

$$\Phi_{\alpha n} = \frac{u_{\alpha n} t_\alpha e^{i\phi_\alpha/2}}{E - E_{\alpha n}} \Phi_0 + \frac{v_{\alpha n} t_\alpha e^{-i\phi_\alpha/2}}{E - E_{\alpha n}} \tilde{\Phi}_0 \quad (7.6a)$$

$$\tilde{\Phi}_{\alpha n} = \frac{v_{\alpha n} t_\alpha e^{i\phi_\alpha/2}}{E + E_{\alpha n}} \Phi_0 - \frac{u_{\alpha n} t_\alpha e^{-i\phi_\alpha/2}}{E + E_{\alpha n}} \tilde{\Phi}_0. \quad (7.6b)$$

We can now insert Eq. (7.6a) and Eq. (7.6b) into Eq. (7.5a) and Eq. (7.5c), which

results in a 2×2 system of linear equations that only involves Φ_0 and $\tilde{\Phi}_0$.

$$A(E)\Phi_0 + B(E)\tilde{\Phi}_0 = (E - \epsilon_r)\Phi_0 \quad (7.7a)$$

$$B^*(E)\Phi_0 + A(E)\tilde{\Phi}_0 = (E + \epsilon_r)\tilde{\Phi}_0. \quad (7.7b)$$

The coefficients are energy-dependent:

$$A(E) = - \sum_{\alpha} \Gamma_{\alpha} \frac{E}{\sqrt{\Delta^2 - E^2}} \quad (7.8a)$$

$$B(E) = - \sum_{\alpha} \Gamma_{\alpha} e^{-i\phi_{\alpha}} \frac{\Delta}{\sqrt{\Delta^2 - E^2}}. \quad (7.8b)$$

They can be derived using the expressions for $u_{\alpha n}$ and $v_{\alpha n}$, namely $u_n^2 = \frac{1}{2}(1 + \xi_n/\epsilon_n)$ and $v_n^2 = \frac{1}{2}(1 - \xi_n/\epsilon_n)$ with $\epsilon_n = \sqrt{\xi_n^2 + \Delta^2}$ and by performing the sums over n in the continuum limit (the resulting integrals converge for $E < \Delta$). In the above equation we have introduced the tunneling rates

$$\Gamma_{\alpha} = \frac{\pi t_{\alpha}^2}{\delta_{\alpha}}. \quad (7.9)$$

The 2×2 system of equations (7.7) has a solution if

$$[A(E) - (E - \epsilon_r)][D(E) - (E + \epsilon_r)] - |B(E)|^2 = 0. \quad (7.10)$$

This amounts to the bound state equation quoted in Eq. (7.1),

$$2\sqrt{\Delta^2 - E^2}E^2\Gamma + (\Delta^2 - E^2)(E^2 - \epsilon_r^2 - \Gamma^2) + 4\Delta^2\Gamma_1\Gamma_2 \sin^2(\phi/2) = 0, \quad (7.11)$$

where $\Gamma = \Gamma_1 + \Gamma_2$ and $\phi = \phi_2 - \phi_1$. This equation is equal to the one reported in Refs. [56, 145], up to the fact that Γ_{α} are defined here without a factor of two associated with spin degeneracy.

7.6.2 PROPERTIES OF THE BOUND STATE ENERGY

Here we discuss the properties of the solutions of Eq. (7.11); see also Ref. [56]. Introducing the Breit-Wigner transmission through the resonant level at $E = 0$, $T = 4\Gamma_1\Gamma_2/(\epsilon_r^2 + \Gamma^2)$, the bound state equation can be written in the convenient

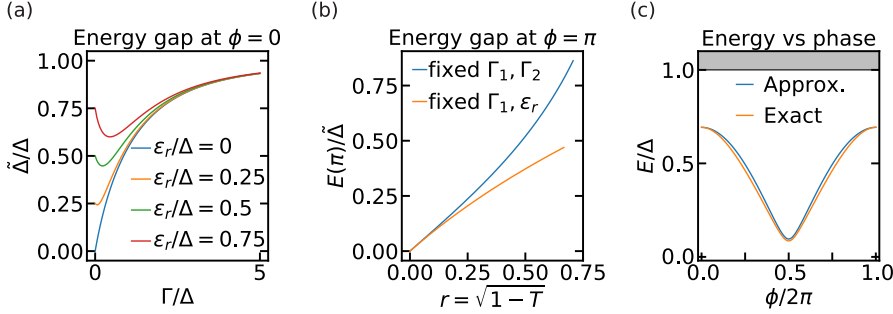


Figure 7.6: Properties of the bound state energy obtained from the resonant level model. (a) Energy gap at $\phi = 0$ ($\tilde{\Delta}$) for different values of the coupling $\Gamma = \Gamma_1 + \Gamma_2$ and the resonant level energy ϵ_r . (b) Parametric plot of the energy gap at $\phi = \pi$ for increasing values of the reflection amplitude r . Both quantities were computed by either varying ϵ_r for a fixed symmetric coupling $\Gamma_1 = \Gamma_2 = \frac{1}{2}\Delta$, or by varying Γ_2 at fixed $\epsilon_r = 0$, $\Gamma_1 = \frac{1}{2}\Delta$. (c) Phase dependence of the bound state energy for the couplings used in the fit for Res. 1 in Fig. 7.4, $\Delta/h = 45$ GHz and $\Gamma/2h = \Gamma_1/h = \Gamma_2/h = 36$ GHz. We fixed ϵ_r/h to a representative value of 10 GHz. The exact solution is a numerical solution of Eq. (7.11). The approximate solution is given by $E = \tilde{\Delta}\sqrt{1 - T \sin^2(\phi/2)}$.

form

$$E^2 [1 + f(E)] = \Delta^2 (1 - T \sin^2 \phi/2) \quad (7.12)$$

with

$$f(E) = \frac{2\Gamma\sqrt{\Delta^2 - E^2}}{\epsilon_r^2 + \Gamma^2} + \frac{\Delta^2 - E^2}{\epsilon_r^2 + \Gamma^2}, \quad (7.13)$$

a dimensionless positive function, defined in the interval $0 \leq E < \Delta$, which decreases monotonously from a value $f(0) = (\Delta^2 + 2\Gamma\Delta)/(\epsilon_r^2 + \Gamma^2)$ to $f(\Delta) = 0$.

We have defined the bound state energy at zero phase difference as $\tilde{\Delta}$. It can be seen easily that $\tilde{\Delta}$ only depends on the total coupling Γ and is thus insensitive to coupling asymmetry. It is determined by the equation $\tilde{\Delta}^2[1 + f(\tilde{\Delta})] = \Delta^2$, which has approximate solutions $\tilde{\Delta} \approx \Gamma$ for $\Gamma \ll \Delta$ and $\tilde{\Delta} \approx \Delta$ for $\Gamma \gg \Delta$. The complete behavior of $\tilde{\Delta}$ as a function of Γ and ϵ_r , obtained from a numerical solution of the bound state equation, is illustrated in Fig. 7.6(a).

The minimum bound state energy is always achieved at $\phi = \pi$, when the right hand side of Eq. (7.12) is minimized. In particular, Eq. (7.12) shows that $E(\pi) = 0$ for $T = 1$ independent of the value of other parameters, and that

$E(\pi) \approx \tilde{\Delta}\sqrt{1-T}$ for $\sqrt{1-T} \ll 1$. The behavior of $E(\pi)$ as a function of T is shown Fig. 7.6(b), obtained by varying either the asymmetry between the couplings ($\Gamma_1 - \Gamma_2$) or ϵ_r .

As Eq. (7.12) suggests, the entire phase dependence of the bound state energy is very well approximated by $E = \tilde{\Delta}[1 - T \sin^2(\phi/2)]$. This relation becomes exact in the two opposite limits $f(0) \ll 1$ (which happens for $\epsilon_r^2 + \Gamma^2 \gg \Delta$), where $\tilde{\Delta} \approx \Delta$, and $f(0) \gg 1$ (for $\epsilon_r^2 + \Gamma^2 \ll \Delta$), where $\tilde{\Delta} \approx \Gamma$. For intermediate values of Γ , the regime where the optimal fit to the experimental data lies, the agreement is still very good, as shown in Fig. 7.6(c). This justifies the use of the model of Eq. (7.2) for the calculation of the qubit levels. We note that for $\Gamma \gg \Delta$ the requirement of finite separation between the continuum and Andreev states is not fulfilled at $\phi = 0$. In this case, we expect the predictions of Eq. (2) in the main text to not be quantitatively reliable as the projection onto an effective two-level system is invalid around $\phi = 0$. These corrections will not affect the main conclusions regarding the enhanced suppression of the charge dispersion at resonance, which is also derived in Ref. [66] in a model where the Andreev levels touch the continuum at $\phi = 0$. In any case, for the optimal model parameters returned by our fit to the experimental data, the Andreev spectrum is separated from the continuum by a gap much larger than E_c at all values of ϕ .

7.6.3 QUBIT ENERGY LEVELS: NUMERICAL SOLUTIONS

The Hamiltonian Eq. (7.2) is used to determine the qubit energy levels given the input parameters E_C , n_g , $\tilde{\Delta}$ and $r = \sqrt{1-T}$. The Hamiltonian is solved numerically by discretizing the coordinate ϕ on a finite grid with grid spacing δ , chosen to be small enough to guarantee convergence of the eigenvalues. Following standard procedure, the derivative operator ∂_ϕ is implemented as a hopping operator between neighboring sites of the ϕ -grid, with hopping strength $4E_C/\delta^2$. The induced charge n_g enters the Hamiltonian, via the Peierls substitution, as a hopping phase $e^{i\delta n_g/2}$. We diagonalize the Hamiltonian on the interval $\phi \in [0, 4\pi]$ with anti-periodic boundary conditions. This choice is required to guarantee the smoothness of the wave functions and the correct offset of energy levels with respect to n_g .

7.7 TRANSPORT MEASUREMENTS

As the device described in the main text also has the capability of measuring transport when the FET is opened [98], we studied the resonances in DC transport measurements. At $V_{\text{FET}} = +4$ V, when the FET was fully conducting, we measured the current I_B and dI_B/dV_B as a function of voltage bias V_B and V_Q across the resonances. By inverting dI_B/dV_B and subtracting the line resistance $R = 57$ k Ω we infer the differential resistance across the qubit junction dV_J/dI_B as shown in Fig. 7.7(a). Here V_J is the voltage drop across the qubit junction. From this measurement the switching current I_s is extracted. I_s is defined as the maximal value of dV_J/dI_B before the junction turns from being in the non-resistive to the resistive state. In Fig. 7.7(b) we plot the two-tone spectroscopy measurement across the resonances, which is also presented in Fig. 1(c) in the main text. This allows us to compare the extracted I_s with the extracted f_{01} across the resonances, Fig. 7.7(c). Here we observe a resonance structure the measured I_s of similar width and spacing as the f_{01} . This further supports the interpretation of resonant tunneling through a single dot level [145]. In this comparison, V_Q is shifted ~ 200 mV for the measurements of I_s to align the resonances. We attribute this to gate drift

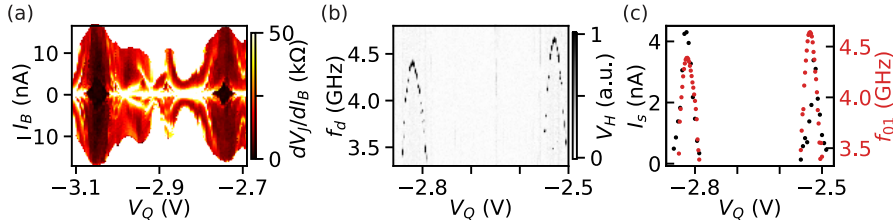


Figure 7.7: Comparison of DC transport and cQED measurements across the two resonances. (a) Measurement of the differential resistance dV_J/dI_B as a function of current bias I_B and V_Q across the two resonances. The measurement is performed at $V_{\text{FET}} = +4$ V where the FET is fully conducting such that the gate voltage across the nanowire effectively drops across the qubit junction. Two regions of supercurrent are observed. We identify the I_B where the junction change from the non-resistive state to the resistive state as the switching current I_s . (b) Two-tone spectroscopy data across both resonances measured at $V_{\text{FET}} = -4$ V completely depleting the FET. Qubit frequencies f_{01} are extracted by Lorentzian fits. (c) Comparison of the extracted I_s from (a) plotted on the left y-axis and the extracted f_{01} from (b). Due to gate drift the I_s curve is shifted by 200 mV to align the resonance peaks.

common to these devices and crosstalk between the two gates as the FET is being varied from conducting to non-conducting.

7.8 CHARGE DISPERSION EXTRACTION

Dispersion data were measured by varying n_g , either with V_Q (Res. 1) or V_{FET} (Res. 2). An example of a dataset is shown in Fig. 7.8(a). Here the frequencies of the even and odd branches are extracted by fits to a double Lorentzians for each ΔV_{FET} (For Res. 1 frequencies are extracted with fits for each V_Q). Here ΔV_{FET} refers to the voltage change in V_{FET} away from the static operation point at $V_{\text{FET}} = -3$ V, where the FET is fully depleted. An example of a fit is shown in Fig. 7.8(b). We extract f_+ and f_- at gate values of local maxima of their difference. We extract the degeneracy qubit frequency f_{01} by fits to a single Lorentzian at ΔV_{FET} where the odd and even branches cross.

For Res. 2 the $0 \rightarrow 2$ two-photon transitions frequencies are also extracted. An example is shown in Fig. 7.8(c) where it is evident that the lower branch of

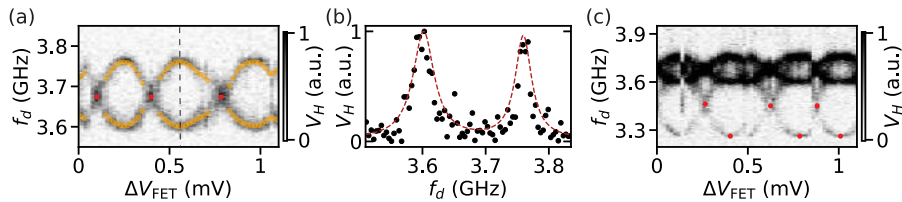


Figure 7.8: Examples of charge dispersion extraction.(a) An example of one of the datasets used to extract δ_{01} of Res. 2. By sweeping V_{FET} in a small range we change the offset charge n_g without varying f_{01} . ΔV_{FET} refer to the variation in V_{FET} from its usual operation point $V_{\text{FET}} = -4$ V. Varying V_{FET} over such small voltages allows changing n_g while keeping the FET depleted. By fitting each line to a double Lorentzians, we extract the two frequency branches (orange data points). Local maxima allow identifying f_+ . The qubit degeneracy frequency f_{01} (red data points) is extracted by fits to single Lorentzians. For Res. 2 an average of the extracted data points results in the extracted f_{01} and δ_{01} for each V_Q . For Res. 1 each extracted value correspond to one data point as f_{01} is varied together with n_g . (b) An example of a double Lorentzian fit used to identify the orange points in (a). The dashed line in (a) indicates ΔV_{FET} for the fitted dataset. (c) An example of a high power measurement of $\delta_{02}/2$ used to extract the data points in Fig. 7.5. The lower frequency branch of the $0 \rightarrow 2$ is extracted by fits to single Lorentzians. The degeneracy frequency $f_{02}/2$ is manually estimated (red data points). As in (a) an average of the extracted values result in the extracted $f_{02}/2$ and $\delta_{02}/2$.

the $0 \rightarrow 1$ interferes with the upper branch of the $0 \rightarrow 2$ transition. However, as both the degeneracy and minimal frequency are clearly distinguishable we define $\delta_{02} = f_{02} - f_{02,-}$. $f_{02,-}$ is extracted by fits to a single Lorentzian and f_{02} is extracted manually.

7.9 SPECTROSCOPY AND CHARGE DISPERSION IN THE OPEN REGIME

In the data presented in the main text we focus on the charge dispersion of the two dot resonances appearing near the pinch-off voltage of the qubit junction. We also extract the dispersion as V_Q is increased. The dispersion is measured in the same way as for Res. 1, where V_Q is swept finely to both vary n_g and the qubit frequency [Fig. 7.9(a)]. In Figs. 7.9(b, c) we show dependence of f_{01} on V_Q and a parametric plot of the extracted δ_{01} values as a function of f_{01} , plotted together with the data and curves presented in Fig. 7.4 of the main text. Here we observe a deviation compared to the transmon dispersion. However, the suppression is not as extreme as observed for the resonances. We attribute this to the transmission not approaching unity as dramatically in this regime, but rather that transport across the junction is described by a few highly transmitting modes. We also observe a non-monotonic behavior in both f_{01} and δ_{01} as a function of V_Q . We interpret this as crossing from a resonant tunneling regime where narrow controlled resonances are observed to a regime where mesoscopic fluctuations in the nanowire junction results in an uncontrolled variation of individual transmission coefficients as a function of V_Q .

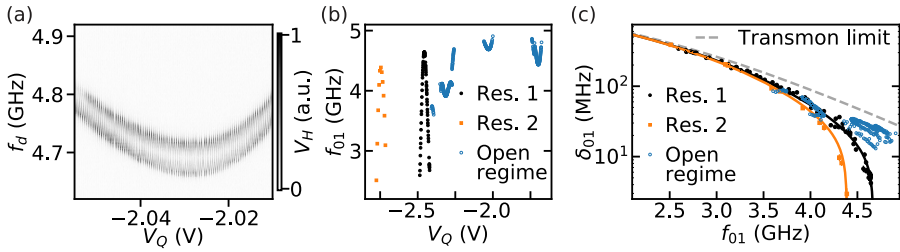


Figure 7.9: Charge dispersion for increasing V_Q . (a) An example of a measurement of δ_{01} in the open regime. (b) f_{01} as a function of V_Q . The data points across Res. 1 (black) and Res. 2 (orange) are the same as presented in the inset of Fig. 4 in the main text. As V_Q is increased further we extract f_{01} in the open regime (blue data points). For $V_Q > -1.7$ V we can no longer resolve δ_{01} , but f_{01} is still resolvable. (c) δ_{01} as a function of f_{01} . The data points across Res. 1 (black) and Res. 2 (orange) and theory curves are the same as presented in Fig. 7.4 in the main text for comparison to the measured δ_{01} in the open regime (blue).

8

Phase-twisted Andreev States in Proximitized Semiconducting Josephson Junctions

Understanding the fundamental Andreev properties of Josephson junctions has been key in building a range of superconducting quantum devices. Here, we demonstrate the emergence of a unique Andreev spectrum as the superconducting phase twists when a flux vortex is trapped in a full-shell nanowire gatemon qubit. Depending on junction gate voltage these coherent energy transitions appear near the qubit transition. As the semiconductor electron density is further increased qubit coherence is lost, associated with softening of the superconducting gap with Andreev states. The experimental observations are in agreement with numerical simulations.

This Chapter is adapted from Ref. [153]. Additional information on the device fabrication and the measurement setup is provided in Chapter 3.

This work was done in collaboration with G. W. Winkler, B. van Heck, T. W. Larsen, D. Sabonis, O. Erlandsson, P. Krogstrup, K. D. Petersson, and C. M. Marcus. The numerical simulations and theoretical modeling described in the text and Fig. 8.4 are developed by Georg W. Winkler and Bernard van Heck.

8.1 INTRODUCTION

The Josephson effect is a coherent macroscopic effect, emerging from underlying Andreev processes [64]. Each Andreev process is characterized by a transmission channel [109], where electrons are reflected as holes at the superconducting interfaces. This results in a pair of bound subgap states for each transmission channel. Several experimental realizations have probed these Andreev states, both spectroscopically [105, 110] and coherently [68, 69]. Originally, this has been studied in the short junction limit [154], where the coherence length ξ is much greater than the junction width L . In this limit, the energy spectrum is described by two phase dispersing spinless states and a phase independent spin degenerate state with a single quasiparticle excitation [56]. More recent demonstrations have demonstrated spin-split Andreev states due to spin-orbit coupling in proximitized semiconducting nanowires [125, 155]. In similar nanowires, superconducting gatemon qubits have been demonstrated [38, 39]. Here the gateable plasma frequency depends on the specific distribution of transmission channels, typically dominated by a few highly transmitting modes [101, 107, 113]. These devices usually operate at large ratios of Josephson energy E_J to charging energy E_C , which results in $\varphi \approx 0$ [30], where φ is the superconducting phase difference across the junction. As a consequence the transition energies of the Andreev spectrum are much larger than the qubit frequencies and therefore not detectable in traditional gatemon experiments. However, recent experiments, have demonstrated the compatibility of the proximitized nanowires with the destructive Little-Parks effect [137, 156, 157], where φ experiences the same number of twists as the number trapped flux vortices in the core of the nanowire [49]. As a result the Andreev states are expected to exhibit a rich dependence on φ and the electrostatic environment.

In this Chapter, we investigate the flux dependence of Andreev states in nanowire-based gatemon qubit devices measured in a cQED resonator architecture. We observe the emergence of unconventional, coherent energy transitions when a magnetic flux threads the full-shell nanowire. We associate these new transitions with Andreev states, where twists in the phase of the superconducting order parameter result in phase-dependent trajectories inside the junction. As a consequence a unique and unconventional gate-dependent energy spectrum is obtained. As the semiconductor electron density is fur-

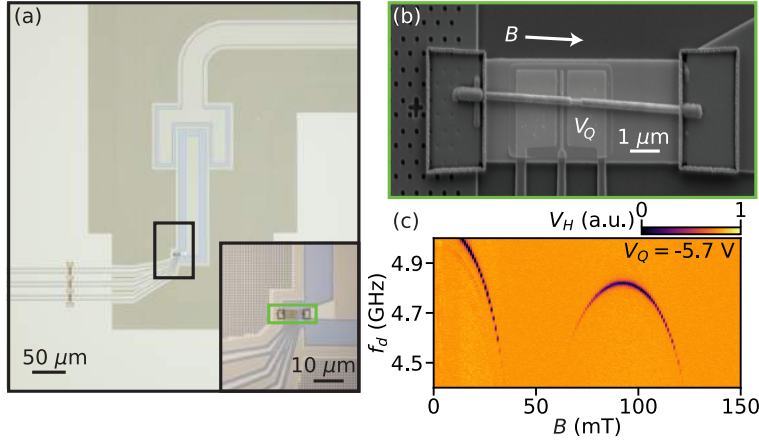


Figure 8.1: Field compatible device and Little-Parks effect. (a) Optical image of the qubit island region of the gatemon qubit device. A distributed readout resonator is capacitively coupled to the rectangular qubit island. An InAs/Al nanowire is placed in the highlighted region (black rectangle) on top of pre-defined bottom gates separated by a HfO₂ dielectric. A large density of flux pinning holes are patterned in the vicinity of the island and the resonator. Inset: Magnified optical image in the nanowire region. (b) Scanning electron micrograph of the nanowire region highlighted in (a) (green rectangle). A gateable Josephson junction (JJ) is formed by removing a ~ 400 nm region of the Al with each side contacted to the island and the ground plane, respectively. The JJ is tuned by the bottom gate V_Q . A magnetic field B is applied parallel to the nanowire (arrow). (c) Measurement of the demodulated transmission voltage V_H of device 1 as a function of B and drive frequency f_d . An oscillatory interference behaviour in f_{01} is observed, associated with the Little-Parks effect. For each column the background is subtracted due to variations in the resonator frequency.

ther increased qubit coherence is completely lost resulting in an enhanced decay rate of the resonator, which we attribute to an increased subgap density of states. Numerical simulations are in qualitative agreement with the experiential observations.

8.2 FIELD COMPATIBLE DEVICE

Nanowire-based gatemon qubit devices were fabricated on high resistivity silicon substrates covered with a 20 nm thin NbTiN film. Superconducting qubit islands, $\lambda/4$ distributed readout resonators with resonance frequencies

$f_{\text{res}} \sim 5$ GHz, transmission line, electrostatic voltage gates, and on-chip gate filters were defined with electron-beam lithography followed by a reactive ion etch, see Fig. 8.1(a). Nanowires are placed on top of the bottom gates separated by a 15 nm HfO₂ gate dielectric. The nanowires consist of an InAs core of 130 nm in diameter, fully coated with 30 nm epitaxial Al [89]. By a selective wet etch a ~ 400 nm segment of the Al shell is removed creating a Josephson junction (JJ) [Fig. 8.1(b)]. Contacting each side of the JJ to ground and the qubit island finalizes the gatemon circuit [38,39]. The ground plane is patterned with a large density of flux-pinning holes, crucial for magnetic field compatibility of the readout resonators [71,80]. Measurements are presented for three devices, device 1, device 2, and device 3.

We apply a magnetic field B parallel to the nanowire while monitoring the qubit frequency f_{01} by two-tone spectroscopy where a drive tone with variable frequency f_d drives the qubit, followed by a dispersive readout tone [27,28]. As B is increased, we observe an oscillatory lobe structure (zeroth lobe and first lobe visible) in the demodulated heterodyne transmission voltage V_H [Fig. 8.1(c)]. We associate this with the destructive Little-Parks where each region corresponds to a quantized number of fluxoids (zero and one magnetic flux quantum Φ_0 in the zeroth and first lobe) [137,156]. We note that the observed maximal value of the first lobe of $B_1 = 93$ mT corresponding to the applied flux $\Phi = \Phi_0$ is in good agreement with the expected $B_1 \sim \Phi_0/\pi r^2 \sim 100$ mT from the nanowire dimensions, where $r = 80$ nm is the nanowire radius.

8.3 PHASE-TWISTED ANDREEV STATES

At low values of junction gate voltage V_Q , the low electron density regime, the gatemon exhibit traditional qubit behaviour. However, as V_Q is increased the gatemon qubit devices operated in the first lobe are commonly observed to lose coherence. This phenomenon is visible by measuring the resonator frequency as a function of V_Q , as shown in Figs. 8.2(a,b). This is performed by varying the resonator drive frequency f_r and measuring the transmission S_{21} , see Chapter 3 for additional details on setup and measurements. At $B = 0$ [Fig. 8.2(a)], we observe a nonmonotonic modulation of f_{res} associated with the voltage modulation of f_{01} as V_Q is increased from complete depletion at $V_Q = -3$ V. For $V_Q \gtrsim -2$ V several avoided crossings are observed, indicating that the

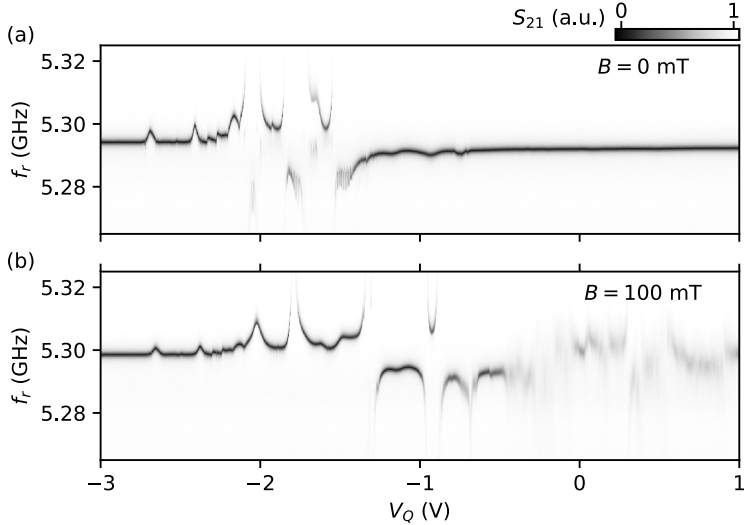


Figure 8.2: Damping of the resonator. Transmission voltage S_{21} measured for device 2 as a function of junction gate voltage V_Q and resonator drive frequency f_r at parallel magnetic field $B = 0$ mT and $B = 100$ mT in (a) and (b), respectively. At $B = 100$ mT, we observe a damping of the resonator frequency as V_Q is turned more positive, associated with an increasing qubit relaxation rate much bigger than that of the resonator.

qubit is tuned in and out of resonance with the resonator. As $V_Q \rightarrow 1$ V, f_{res} is approaching its unshifted value as $V_Q \rightarrow 1$ V, which indicates a vanishing dispersive shift as f_{01} is increasing far above f_{res} . In the first lobe ($B = 100$ mT), an almost identical pattern is observed for $V_Q \lesssim -1$ V [Fig. 8.2(b)], with the small differences due to the slight reduction in the induced superconducting gap Δ in the Al shell. For $V_Q \gtrsim -1$ V, however, the resonance frequency dip is both reduced and widened, in contrast to measurements in the zeroth lobe. We interpret this damping of the resonator to be decay through the qubit, indicating that the relaxation rate of the qubit is much larger than that of the resonator. By repeating these scans in intervals of $B = 5$ mT we fully map the behaviour in both the zeroth and first lobe, identifying the damping of the resonator as a distinct feature of the first lobe, see Section 8.6. We associate this resonator damping with softening of the induced gap in the nanowire JJ.

To further investigate the anomalous behaviour in the first lobe, we map the gate dependence of the qubit transition at $B = 100$ mT by to two-tone spec-

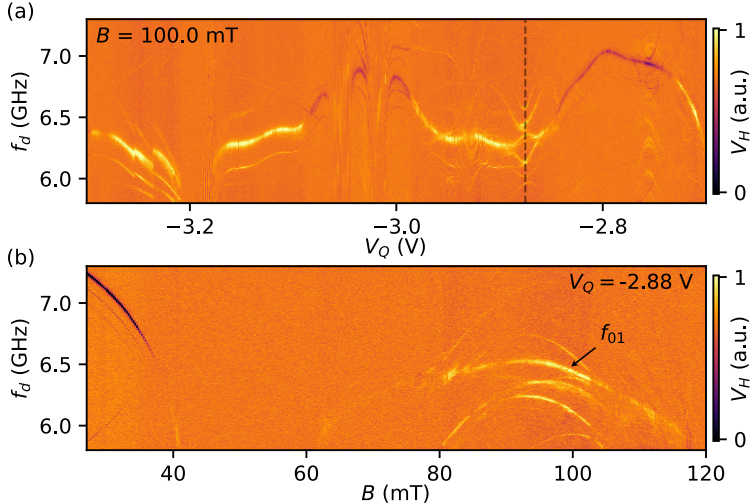


Figure 8.3: Measurements of phase-twisted Andreev transitions. (a) Two-tone spectroscopy measurement of demodulated transmission V_H as a function of f_d and V_Q at $B = 100$ mT. Multiple regions of new energy transitions are observed. (b) Measurement of V_H as a function of B and f_d at $V_Q = -2.88$ V [dashed line in (a)]. Both the qubit and additional transitions exhibit the expected oscillatory behaviour associated with Little-Parks effect with no extra transitions appearing in the zeroth lobe. We note different local maxima in B for the new states. We associate the widest transition with the qubit frequency f_{01} (arrow), which persist as a function of V_Q in (a). This transition exhibits a weaker dependence of B . Measurements presented are from device 1.

troscopy, see Fig. 8.3(a). In the regime just before the damping of the qubit starts to dominate, we observe a range of unconventional energy transitions emerging. These states show strong gate dependence near some values of V_Q , and several avoided crossings with the qubit transition, indicating that these states couple to the qubit. For $V_Q < -3.3$ V, we only observe the usual gatemon transition frequencies, see Section 8.7. We next study the field dependence of f_{01} at $V_Q = -2.88$ V, where these new transitions are observed. Here, we again observe an oscillatory behaviour in f_{01} associated with the Little-Parks effect with the bundle of transition frequencies visible in the first lobe only, see Fig. 8.3(b). These extra transitions exhibit local maxima at larger values of B than the qubit transition indicating smaller effective cross sectional areas of wavefunctions of these states. In addition, the transitions appear to have

distinctively different dependence on B , compared to the qubit transition [indicated in Fig. 8.3(b)]. We speculate that these transitions are associated with Andreev states whose transition frequencies scale with Δ [109] as opposed to f_{01} , which scales with $\sqrt{\Delta}$ [30]. We note the change in direction of the dispersive shift for $f_{01} \lesssim 6.5$ GHz in Figs. 8.3(a, b) associated with the straddling regime [30]. We speculate that the Andreev transitions always have the same sign of the dispersive shift as the qubit transition as they are only visible due to coupling via the qubit.

8.4 NUMERICAL SIMULATIONS

To understand the origin of the lobe-dependent subgap spectrum, we perform simulations of a full-shell nanowire Josephson junction of similar dimensions as the measured devices. We model a hexagonal InAs wire with 130 nm diameter coated by a 30 nm thick Al shell with a junction width of 150 nm. The simulations are performed with the same method applicable to realistic three dimensional devices as used in Ref. [158] adapted here to the Josephson junction geometry. Figures. 8.4(a, b) show a longitudinal cut of the device with the electrostatic potential ϕ in the InAs nanowire plotted for two different gate voltages V_{BG} . The phase of the superconducting order parameter is indicated in the Al shell. Apart from a possible phase difference $\Delta\varphi$ across the junction, in the first and higher lobes ($n \neq 0$) the flux induced phase winding causes a spatial dependence of the phase also on either side of the junction. Therefore, Andreev bound states can experience multiple different phase differences depending on the path they travel across the junction. In particular as V_{BG} is increased and the potential barrier is reduced [Figs. 8.4(a, b)], this effect of phase dependent paths are expected to be relevant. Possible paths travelling diagonally across the junction are indicated in Fig. 8.4(b), which would experience a π -phase difference in the first lobe.

The phase winding in the superconducting shell has dramatic effects on the Andreev bound state spectrum in the junction. In Figs. 8.4(c, d) we show the density of states (DOS) in the junction in the zeroth lobe. As V_{BG} is turned more positive the junction becomes more open due to the decreasing potential barrier and more Andreev bound states with strong phase dependence appear, with an energy minimum around $\Delta\varphi = \pi$. However, the energies of Andreev bound states remain on the order of the bulk superconducting gap

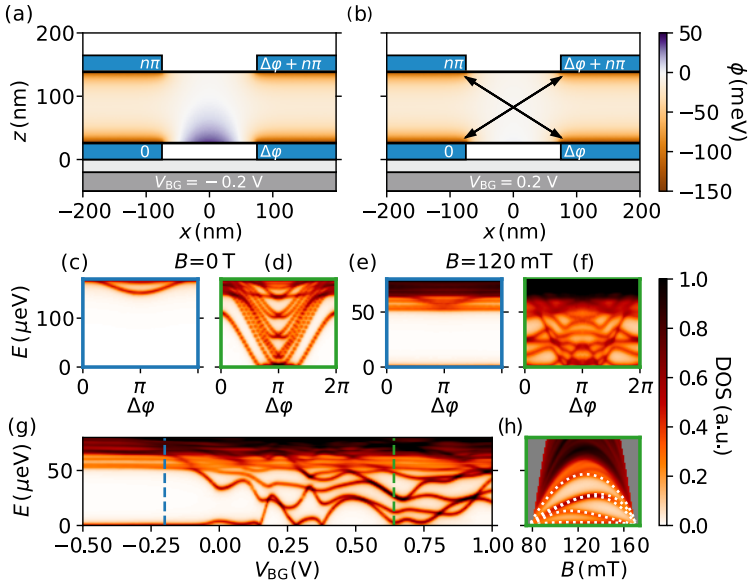


Figure 8.4: Numerical modeling of the flux-dependent Andreev states (a, b) Longitudinal cut of the simulated Josephson junction device at backgate voltage $V_{BG} = -0.2$ V and $V_{BG} = 0.2$ V. The electrostatic potential is shown in InAs, covered by a full Al shell (blue), separated from a global backgate (dark grey) by a thin HfO_2 dielectric (light gray). The band offset between InAs and Al has been chosen to be 150 meV, as in Ref. [158]. Values of the phase of the superconducting order parameter are indicated in the Al shell and possible diagonal paths of Andreev bound states (arrows) are shown in (b). (c, d) DOS in the junction as a function of $\Delta\varphi$ at zero magnetic field for $V_{BG} = -0.2$ V and $V_{BG} = 0.6$ V. (e, f) same as (c, d) but at $B \approx 0.12$ T in the middle of the first lobe. (g) DOS as a function of V_{BG} at $B \approx 0.12$ T for $\Delta\varphi = 0$. (h) DOS as a function of magnetic field at $V_{BG} = 0.6$ V and $\Delta\varphi = 0$. For (c–h) we assume a spin-orbit coupling of $\alpha = -0.1$ eV nm and InAs/Al band offset of 150 meV as in the main text of Ref. [158]. Dashed colored lines in (g) corresponds to values of V_{BG} in (c)–(f) and (g) (colored frames).

at $\Delta\varphi = 0$. In Figs. 8.4(e, f) we show the DOS in the first lobe, for parameters corresponding to the topological phase. Due to the presence of vortex states the bulk gap is reduced here [136]. The topological Majorana zero modes show up close to zero energy and show little phase dependence for the case of a closed junction, see Fig. 8.4(e). If the junction is opened the gap fills with low-energy Andreev bound states, see Fig. 8.4(f). While the Andreev bound

states still show strong dependence on $\Delta\varphi$, however now there are also low energy states around $\Delta\varphi = 0$. As discussed in Ref. [82], the presence of low energy states at $\Delta\varphi = 0$ can lead to additional lines and anti-crossings in the qubit spectrum. Furthermore, if the gap becomes densely filled with subgap states a damping of the resonator line would be expected. In Fig. 8.4(g) we show the dependence on V_{BG} of the subgap states at $\Delta\varphi = 0$. They show a complicated nonmonotonic dependence on V_{BG} which can explain the multiple transitions as a function of gate voltage observed in the experimental qubit spectroscopy. Figure 8.4(h) presents the dependence on magnetic field of these Andreev bound states at $\Delta\varphi = 0$. They do not follow the same magnetic field dependence as the Al gap, often having their energy maximum at a different flux, which is also compatible with the experimental observations in Fig. 8.3(b). While the results shown here correspond to the topological case, the results are qualitatively very similar in the trivial case.

8.5 TIME DOMAIN MEASUREMENTS

To further investigate the origin of the observed supgap states, we focus on a narrow region of V_Q , where the transitions exhibit local minima [Fig. 8.5(a)]. Here, we observe a strong dependence on V_Q indicating that the states reside in the junction. Additionally the states exhibit similar local minima in V_Q , possibly due to a local maxima in the transmission coefficients, which would bring down Andreev transitions in frequency. For $V_Q \gtrsim -2.7$ V qubit coherence is lost and we can no longer probe the qubit frequency, consistent with the findings of Fig. 8.2, see Section 8.6. We note that the measurements in Fig. 8.2 and Figs. 8.3, 8.5 are from two different devices with different threshold V_Q at which coherence is lost. The characteristic behavior is the same in all devices.

Throughout the gate scan presented in Fig. 8.5(a), the transitions can be driven coherently. Figure. 8.5(b) shows an example of Rabi measurements across the transitions at $V_Q = -2.752$ V. All transitions exhibit coherent oscillations with T_1 relaxation times of 3–5 μ s measured in a subsequent measurement. We observe that the transitions in closest vicinity to the uncoupled qubit transition demonstrated the fastest oscillations [green and red panels in Fig. 8.5(b)] supporting the interpretation that the Andreev states are visible due to the coupling via the qubit. This is in qualitative agreement with numerical simulations presented in Ref. [82]

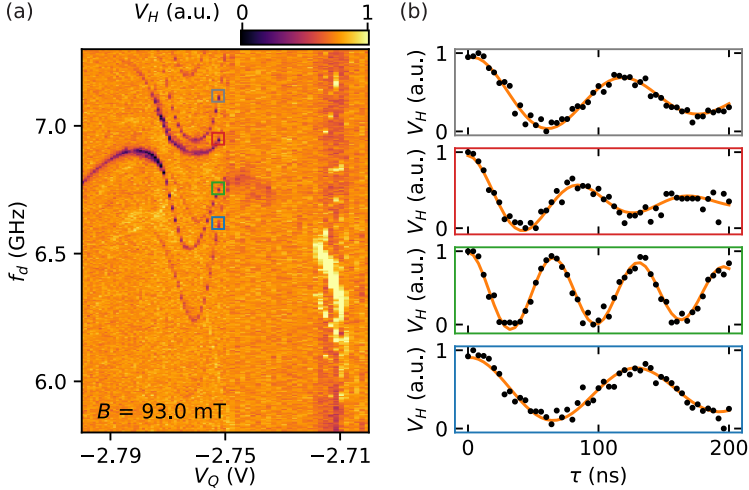


Figure 8.5: Time domain measurements of Andreev transitions. (a) Narrow gate dependence of the Andreev transitions at $B = 93$ mT. We observe that the extra transitions are strongly gate dependent and all with local minima at similar V_Q . For $V_Q \sim -2.7$ V the qubit can no longer be coherently driven. (b) Rabi measurements of V_H as a function of varying drive pulse width τ and f_d at $V_Q = -2.752$ V [colored squares in (a) match frame colors in (b)]. We observe Rabi oscillations of all the transitions in the frequency range, with fastest oscillations of the transitions nearest the uncoupled qubit transitions (green and red frames). The experimental data (black data points) are fitted to exponentially damped sinusoids (orange curves).

8.6 FIELD DEPENDENCE OF RESONATOR FREQUENCY

To investigate the observed damping of the readout resonator, we systematically map f_{res} for increasing values of B . We repeat the transmission scans performed in Fig. 8.2 for values of B increasing by 5 mT, as shown in Fig. 8.6. It is observed that the overall spectrum remain roughly unchanged up to $B = 45$ mT, except small changes in the avoided crossings, which is attributed to the field-induced decrease in Δ . At $B = 50$ – 55 mT, we enter the destructive regime ($\Phi \sim \Phi_0/2$), where superconductivity is destroyed. When entering the first lobe, superconductivity is restored. In the first lobe, the characteristic behavior of the spectra is very similar with few variations due to the field modulation of Δ . We observe the damping of the resonator for all values of B for $V_Q \gtrsim -0.5$ V, in contrast to the zeroth lobe.

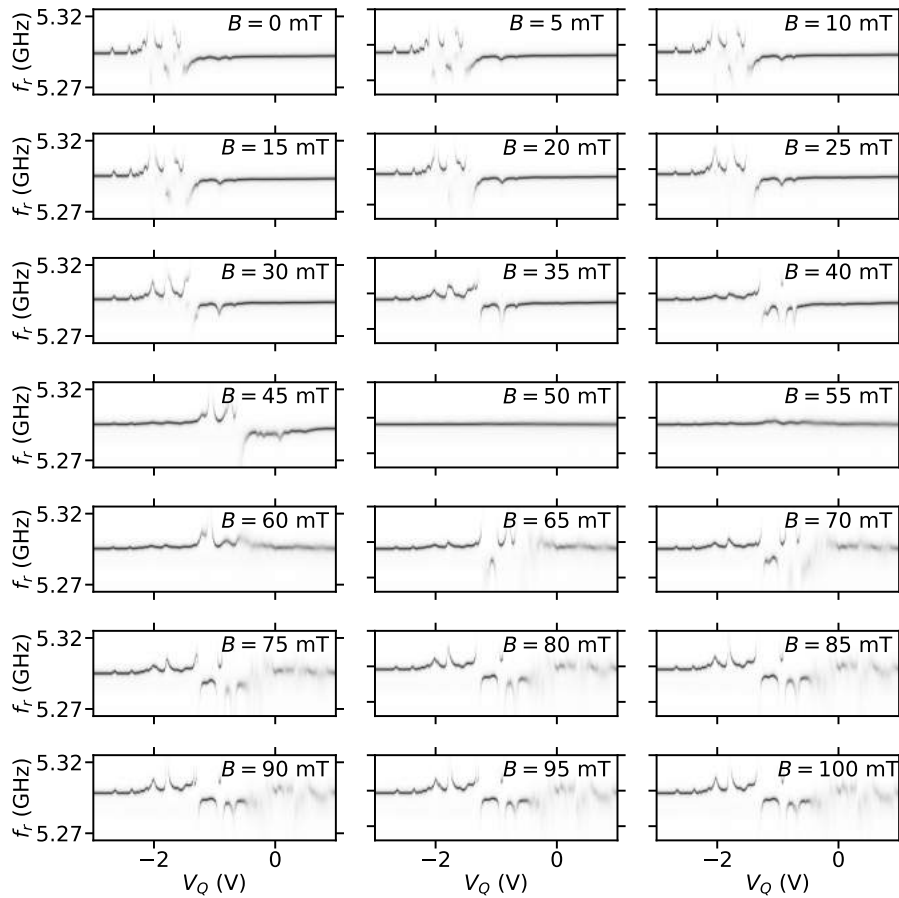


Figure 8.6: Full measurement of the lobe-dependent resonator damping. Transmission voltage S_{21} as a function of junction gate voltage V_Q and drive frequency f_d at increasing parallel magnetic field $B = 0\text{--}100 \text{ mT}$ in steps of 5 mT.

In Figs. 8.3 and 8.5 the behavior of the phase-winded Andreev transitions are investigated. For $V_Q > -2.7$ qubit coherence is lost. Figure 8.7 shows a resonator scan in this region, where we similarly observe the damping of the resonance frequency. This is consistent with the interpretation that the Andreev states are only visible in an open junction regime, with the resonator damping occurring due to softening of the superconducting gap.

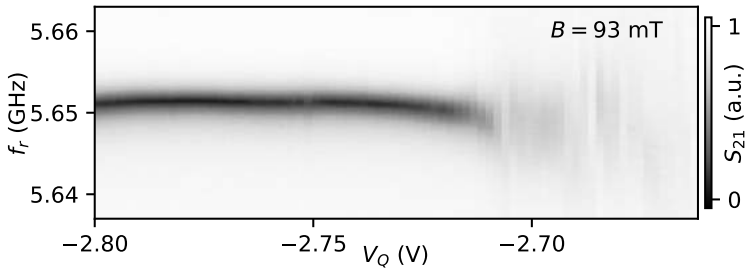


Figure 8.7: Corresponding resonator scan as a function of V_Q measured interleaved with the two-tone spectroscopy measurement presented in Fig. 8.5(a).

8.7 GATE DEPENDENCE IN ZERO TH AND FIRST LOBE

To further support that the observed transitions are a characteristic phenomenon associated with phase twists in the first lobe, we repeat the gate scan shown in Fig. 8.3(a) at $B = 35$ mT, shown in Fig. 8.8(a). We observe a traditional gatemon spectrum, where the power broadened $0 \rightarrow 1$ and the two-photon $0 \rightarrow 2$ transitions are visible without all the additional transitions visible at $B = 100$ mT [Fig. 8.8(b)]. The absence of extra transitions lines in the zeroth lobe supports the interpretation of phase winded Andreev energy states due to the lobe-dependent phase twists. We note the small region in Fig. 8.8(a) near $V_Q \sim -3$ V, where two main transitions are visible. We speculate that this could be due to fast occurring charge jumps resulting in a doubling of the qubit line [62]. At all other V_Q the qubit transition lines exhibit nearly identical behavior, with small modification in the absolute values due to the reduction in Δ at $B = 100$ mT.

From the numerical modeling presented in Fig. 8.4, the observation of phase-winded Andreev states are expected to be achievable for increasing

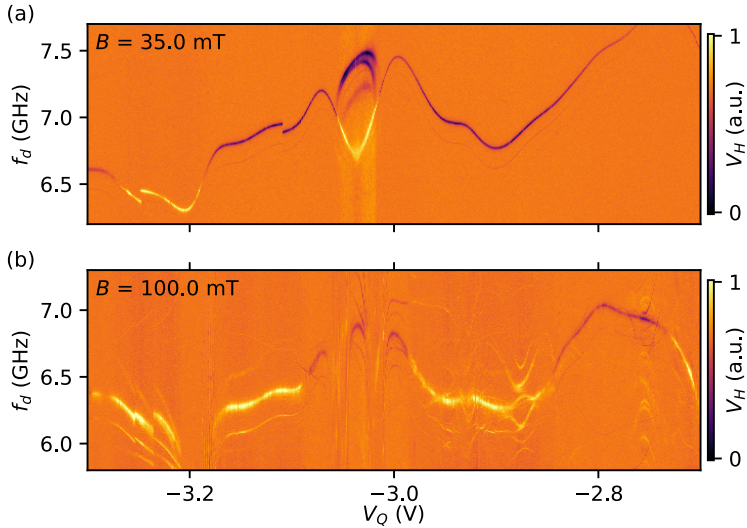


Figure 8.8: Comparison of zeroth and first lobe two-tone spectroscopy. Two-tone spectroscopy measurement as a function of f_d and V_Q at $B = 35$ and 100 mT in (a) and (b) to compare the gate dependence in the zeroth and first lobe. Panel (b) is also presented in Fig. 8.3(a).

values of V_Q . This interpretation is supported by gate scans probing the qubit spectrum for decreasing V_Q , as shown in Fig. 8.9. Here, we map the qubit spectrum for values of V_Q below the values shown in Fig. 8.8, and no additional states are observed with only a single qubit transition line visible. This observation is consistent with creating a junction barrier for low values of V_Q , and the effect of the phase dependent junction paths are much less important. As a result the gatemon spectrum behaves as it would in the zeroth lobe.

8.8 CHARGE DISPERSION IN FIELD

As discussed in Section 2.5, cQED gatemon architectures are potentially compatible with detecting Majorana zero modes (MZMs). If two MZMs at each side of the JJ overlap, a coherent path for $1e$ transport is created. As a consequence the two even-odd uncoupled charge dispersion branches will couple. This coupling is expected to result in a double-well potential with two introwell

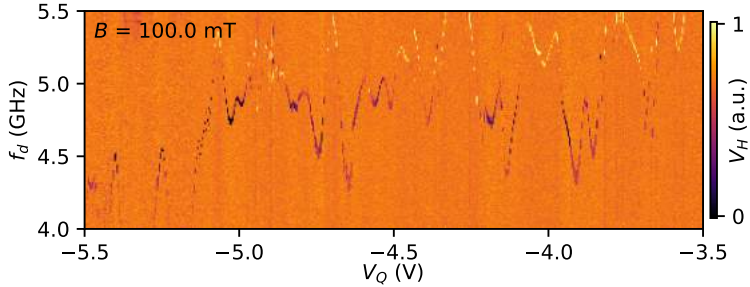


Figure 8.9: Qubit behavior at low V_Q . Two-tone spectroscopy measurement as a function of f_d at $B = 100$ mT for decreasing V_Q . In this regime, no additional transitions are observed.

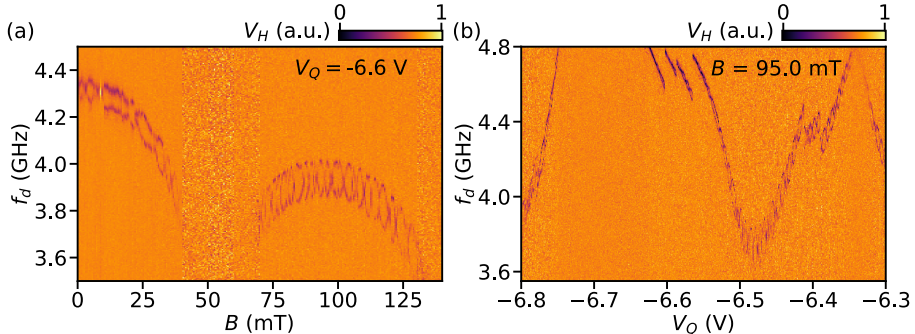


Figure 8.10: Mapping the qubit in the first lobe. (a) Two-spectroscopy as a function of parallel magnetic field B measured in device 3. We observe oscillations in the qubit frequency associated with the charge dispersion of the two parity branches. (b) Two-spectroscopy as a function of V_Q over the entire region in the first lobe of resolvable charge dispersion.

and two interwell transmon transitions [44], where the interwell transitions are expected to be suppressed due to vanishing overlap of wavefunctions. Experimentally this is expected to result in avoided crossings in the frequency charge dispersion spectrum along with a change in periodicity and doubling of transitions lines, depending on the energy scales [82]. Recent experimental and theoretical work [136,137] suggest that full-shell nanowires host MZMs in the first lobe. Motivated by this, we study the charge dispersion as a function of magnetic field in gateon full-shell devices.

We measure the qubit frequency as a function of B by two-tone spectroscopy, as shown in Fig. 8.10(a). This is measured in a third device of same design the device shown in Fig. 8.1, device 3. Here, the qubit frequency exhibit the oscillatory lobe behavior associated with the Little-Parks effect. Due to drift in the offset charge n_g we observe the parity branches of the qubit frequency oscillate on top of the oscillating Little-Parks envelope. At the center of the first lobe, $B_1 = 95$ mT, we map the qubit dependence of V_Q , see Fig. 8.10(b). Here, we find that the charge dispersion is resolvable in the range $V_Q = -6.8$ – -6.3 V. For $V_Q > -6.3$ V, the qubit frequency becomes too large to resolve the charge dispersion due to increasing ratios of E_J/E_C , and for $V_Q < -6.8$ V the qubit frequency is rapidly decreasing as the JJ approaches full depletion. In the entire range of resolvable charge dispersion, we measure the charge dispersion in steps of 25 mV and every 10 mT, with one example shown in Fig. 8.11. Here, we vary n_g by the middle gate shown in Fig. 8.1(a), V_{ng} . In doing so we observe an oscillating behavior of the parity branches, around a nearly constant qubit frequency. To look for differences between the zeroth and first lobe we perform these measurements starting at $B = 0$ T. We observe no signatures of anti-crossing or change in periodicity, as we transition from the zeroth to the first lobe. This indicates that the nanowires either do not host MZMs or that the overlapping energy E_M (see Section 2.5 for further details) is too small to resolve. The numerical simulations in Fig. 8.4(e, d) suggest that detectable overlap between the MZMs only occurs in regimes of large supgap DOS. This would mean that it is heavily complicated to observe signatures of MZMs this device geometry due to the large density of Andreev states. Even if the regime, in which the measurements of Fig. 8.3 and Fig. 8.5 are performed do host MZMs it is not possible to clearly distinguish the transitions from those of Andreev states. This is consistent with the simulations presented in Ref. [82], which also argue that the picture presented in Section 2.5 based on Ref. [44] is being modified by the presence of Andreev states and finite junction effects.

This type of study of the charge dispersion have been performed in several similar devices, and also in half-shell nanowire devices. In half-shell devices the nanowire is only partly coated with Al, allowing the semiconducting segments to be tuned by plungers gates. The device design shown in Figs. 8.1(a, b) has three gates compatible with half-shell devices, where the two plunger gates tune the segments on each side of the junction with the middle

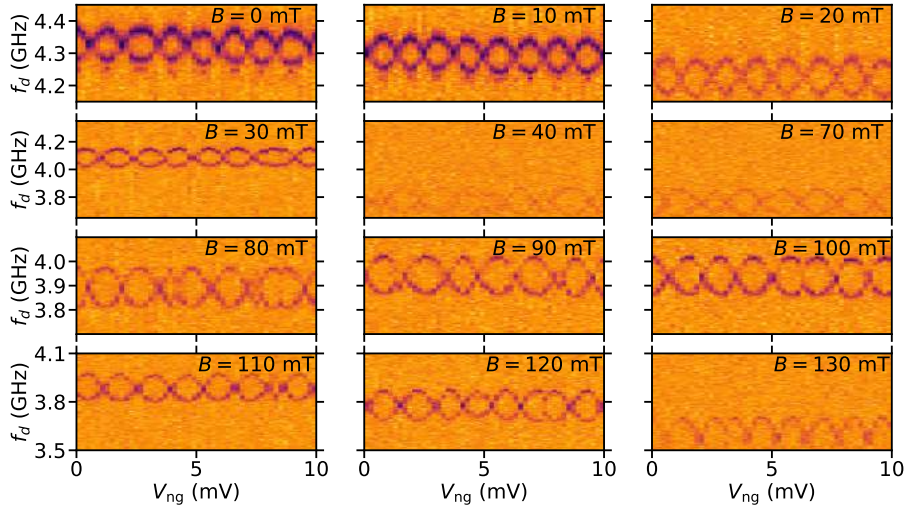


Figure 8.11: Mapping the charge dispersion in the first lobe. Dispersion measurements at increasing parallel magnetic field B acquired at $V_Q = -6.6$ V. Measuring V_H as a function of f_d and varying offset charge gate V_{ng} [the middle gate in Fig. 8.1(a)] yields an oscillating in the qubit spectra. Majorana signatures are predicted as avoided crossing and change in periodicity. No difference between dispersion measurements in zeroth lobe ($B = 0\text{--}40$ mT) compared the first lobe ($B = 70\text{--}130$ mT) is observed.

gate tuning the nanowire JJ. Similar charge dispersion experiments were also performed on those nanowires. For all devices, we did not observe any clear signatures of MZMs. For more details on experiments on half-shell device I refer to Refs. [71, 81].

8.9 CONCLUSIONS

In summary, we have observed flux-dependent, coherent energy transitions emerging when the superconducting phase twists as magnetic flux threads a full-shell nanowire-based gatemon qubit. We explain these transitions by phase-winded Andreev states in agreement with numerical simulations. This distinct new behavior of Andreev states exhibit strong variations as the junction gate is varied consistent with phase dependent paths inside the Josephson junction. As the voltage is increased qubit coherence is lost and an enhanced relaxation of the resonator is observed, interpreted as softening the supercon-

ducting gap due to a large density of subgap states. This new type of Andreev spectrum opens an exciting research direction for Andreev qubits. In addition future experiments directly probing the Andreev spectrum may be suitable to investigate the predicted emergence of topological regimes [44, 136].

9

Outlook

This thesis has explored the semiconducting Josephson junctions of superconducting qubits based on proximitized nanowires. We have performed qubit anharmonicity measurements, yielding information about the transmission properties of these junctions. We have demonstrated suppressed charge dispersion, which we explain by a ballistic conduction channel formed by a resonant level in the junction. Furthermore, we have shown the integration DC transport techniques in these devices and together with their field compatibility this opens a range of new operating regimes otherwise inaccessible for conventional superconducting qubits. This all together form a foundation for future fundamental explorations in these device architectures. Future research directions may take advantage of these features in devices based on two-dimensional electron gasses, where the lithographic freedom allows new device designs, which may open the possibility of new types of qubits. In addition, the ballistic conduction channel provided by resonant tunneling along with the magnetic field resilience motivates new extensions of Andreev qubit research. This may involve probing the phase-twisted Andreev states, spin-split odd states, and signatures of Majorana zero modes.

Gatemon qubits also present an interesting platform for more conventional superconducting qubit research. Improving qubit performances of devices based on scalable top-down approaches platforms, such as two-dimensional

electron gasses or selective area growth, may see gatemonas as a scalable all-electric alternative to conventional superconducting qubits. With the advantage of *in-situ* tunability of qubit parameters this would allow gatemonas to participate in this exciting, and progressing research field.

A

Fabrication

This Appendix presents the fabrication recipe used for the device in Chapter 4. This recipe is adapted from Ref. [96]

AL FILM

- Load high resistive Si wafer into AJA International metal evaporation system
- Kaufmann argon milling 15 s at 300 V with 15 cm³/min Ar gas flow with ion gas on and 1 mTorr pressure - warm up 60 s before milling
- Evaporate 100 nm of Al with rate $\sim 2 \text{ \AA/s}$

CONTROL LINES, QUBITS ISLANDS, READOUT RESONATORS, AND TRANSMISSION LINE

- Spin AZ1505 photo resist at 4000 rpm for 45 s and bake the resist at 115°C for 1 min
- Expose design with Heidelberg μ PG101 LED writer, expose each write field 30 ms, defocus -5

- Develop the resist with AZ developer for 40 s followed by 30 s Milli-Q water rinse and 4 min plasma ashing (cleaning with oxygen plasma)
- Etch the pattern for 1 min in 50°C Transcene Al etchant type D followed by 10, 30 s Milli-Q water rinse - blow dry with N₂ and 1 min plasma ashing

LED DEFINED MARKS

- Spin AZ1505 photo resist at 4000 rpm for 45 s and bake the resist at 115°C for 1 min
- Expose design with Heidelberg μ PG101 LED writer, expose each write field 30 ms, defocus -5
- Develop the resist with AZ developer for 40 s followed by 30 s Milli-Q water rinse and 4 min plasma ashing
- Evaporate 5 nm Ti followed by 80 nm Au with rate \sim 1 Å/s
- Lift off in 80°C NMP (1-methyl-2-pyrrolidone) for 1 hr. followed by 30 s sonication. Rinsed in acetone, IPA - blow dry with N₂ and 2 min plasma ashing

WIRE ALIGNMENTS MARKS

- Spin EL9/CSAR9 EBL resist at 4000 rpm for 45 s and bake 1, 3 min 185°C
- Define pattern with electron-beam lithography (EBL) with a dose time of 0.56 μ s/point, beam current of 2 nA, 300 μ m field size, 20k points
- Develop for 60 s in o-xylene, 30 s in 1:3 MIBK:IPA and 10 s in IPA - blow dry with N₂ and 2 min plasma ashing
- Evaporate 5 nm Ti followed by 80 nm Au with rate \sim 1 Å/s
- Over night lift off in acetone, 2 min sonication in IPA, 2 min plasma ashing

WIRE WINDOWS

- Spin EL9 EBL resist at 4000 rpm for 45 s and bake 3 min 185°C
- Define pattern with EBL with a dose time of 0.56 μ s, beam current of 5 nA, 300 μ m field size, 20k points

CLEAVING

- Cleave chip in 9 pairs using Loomis automatic scriber with a scribe pressure of 1.8 psi and break pressure of 6.0 psi

WIRE PLACEMENT

- Develop for 75 s in 1:3 MIBK:IPA followed by 10 s IPA rinse - blow dry with N₂ and 1 min plasma ashing
- Randomly place nanowires in the defined windows with the tip of a cleanroom wipe
- Strip resist by rinsing chip in acetone, IPA and 2 min plasma ashing

WIRE JUNCTION ETCH

- Spin PMMA 4% EBL resist at 4000 rpm for 45 s and bake 3 min 185°C
- Load optical images into design file for alignment of design to nanowires
- Define etch windows with EBL, 0.3 μ s/point does time, 1 nA beam current, 300 μ m field size, 60k points
- Develop for 60 s in 1:3 MIBK:IPA followed by 10 s IPA rinse - blow dry with N₂ and 1 min plasma ashing
- Etch nanowire junction for 1 min in 50°C Transcene Al etchant type D followed by 30 s Milli-Q water, 10 s IPA rinse and nitrogen blow dry
- Strip resist by rinsing chip in acetone, IPA - blow dry with N₂ and 2 min plasma ashing
- SEM image the etched nanowires to find suitable candidates for the qubit junction

CONTACTS AND SIDE GATE

- Spin EL9, PMMA 4% EBL resist at 4000 rpm for 45 s and bake 1, 3 min 185°C
- load SEM images to design for gates, contacts,
- Define gate and contact pattern with EBL, 0.3 μs dose time, 1200 $\frac{\mu\text{C}}{\text{cm}^2}$ area dose, 1 nA beam current, 300 μm field size, 60k points
- Develop 60 s 1:3 MIBK:IPA followed by 10 s IPA rinse - blow dry with N₂ and 1 min plasma ashing
- Load sample into AJA evaporation system, argon mill oxide layer on nanowire for 4.5 min, evaporate 1 nm Ti and 150 nm Al
- Lift off 80° C NMP for 1 hr followed by 30 s sonication. Rinsed in acetone, IPA - blow dry with N₂ and 2 min plasma ashing

WIRE BONDING

- Glued to PCB sample board with PMMA - dry for ~ 30 min
- Al wire bonded control lines to PCB sample board
- Loading in indium sealed Al box and sample holder

B

Fabrication

This Appendix presents the fabrication recipe used for the device in Chapters 6–8. The fabrication process and fabricated were carried out by Marina Hesselberg, Karthik Jambunathan, Robert McNeil, Karolis Parfeniukas, Agnieszka Telecka, Shivendra Upadhyay, and Sachin Yadav.

DEEP ETCHED ALIGNMENT MARKS

- Spin CSAR13 EBL resist at 4000 rpm for 45 s and bake 1 min 185°C on high resistive Si wafer
- Define pattern with EBL with a base dose of $430 \mu\text{C}/\text{cm}^2$, beam current of 10 and 100 nA, 500 μm field size, 50k points
- Develop for 30 s in o-xylene, 15 s in 1:3 MIBK:IPA and 10 s in IPA - blow dry with N_2 and 2 min plasma ashing
- Deep etch using advanced silicon etching
- Clean: 80°C NMP, Acetone, IPA, Milli-Q water for 2 hr, 15 min, 10 min, 10 min, 30 s - blow dry with N_2 and 2 min plasma ashing

N_BTiN FILM

- Clean in buffered oxide etch for 2 min, 3 × 15 Milli-Q water rinse - blow dry with N₂
- Load high resistive Si wafer into AJA International metal evaporation system
- NbTiN deposition: sputter NbTi in N atmosphere - 20 nm
- Rinse in acetone, IPA for 2, 2 min- blow dry with N₂

CONTROL LINES, QUBITS ISLANDS, FLUX PINNING HOLES, READOUT RESONATORS, AND TRANSMISSION LINE

- Spin CSAR13 EBL resist at 4000 rpm for 45 s and bake 2 min 185°C
- Define pattern with EBL with a base dose of 430 μC/cm², beam current of 10 and 100 nA, 500 μm field size, 50k points
- Develop for 30 s in o-xylene, 15 s in 1:3 MIBK:IPA and 10 s in IPA - blow dry with N₂ and 2 min plasma ashing
- Etch the pattern with Reactive Ion Etch, PRO ICP etcher (Inductively Coupled Plasma Etching) with Cl₂ gas
- Clean: 80°C NMP, NMP, IPA, Acetone, Milli-Q water for 2 hr, 15 min, 10 min, 10 min, 30 s - blow dry with N₂ and 2 min plasma ashing

GATE DIELECTRIC AND CROSS OVER DIELECTRIC

- Spin EL13, PMMA 4% EBL resist at 4000 rpm for 45 s and bake 1, 1 min 185°C
- Define pattern with EBL with a base dose of 1300 μC/cm², beam current of 10 nA, 500 μm field size, 50k points
- Develop for 60 s in 1:3 MIBK:IPA followed by 15 s IPA rinse - blow dry with N₂ and 1 min plasma ashing
- Atomic layer deposition (ALD) - 15 nm HfO₂ at 110°C
- Lift off 80°C NMP, NMP, acetone, IPA, Milli-Q water for 2 hr, 10 min, 5 min, 5 min, 30 s - blow dry with N₂ and 2 min plasma ashing

DICING

- Spin AZ1505 photo resist at 4000 rpm for 45 s and bake the resist at 115°C for 1 min
- Dice in subsets to proceed for nanowire placements

WIRE PLACEMENT

- Clean: acetone, IPA for 5, 5 min - blow dry with N₂ and 2 min plasma ashing
- Place single nanowires on top of gate dielectric in predefined region with a micro manipulator

WIRE JUNCTION ETCH

- Spin AR 300-80 adhesion promoter at 4000 rpm for 45 s slow acceleration and bake 2 min 115°C
- Clean: Dioxalene, acetone, IPA for 2 min, 2 min, 30 s - blow dry with N₂
- Spin EL9 resist at 4000 rpm for 45 s slow acceleration and bake 3 min 185°C
- Define etch windows with EBL with a base dose of 450 $\mu\text{C}/\text{cm}^2$, beam current of 5 nA, 500 μm field size, 200k points
- Develop 22 s 1:3 MIBK:IPA followed by 20 s IPA rinse - blow dry with N₂ and 1 min plasma ashing
- Etch nanowire junction for 52 s in MF321 Al etchant followed by Milli-Q water, Dioxalene, acetone, IPA for 30, 120, 120, 30 s - blow dry with N₂ and 1 min plasma ashing

CROSS LINKED PMMA CROSS OVERS

- Spin PMMA 4% resist at 4000 rpm for 45 s slow acceleration and bake 2 min 115°C
- Define pattern with EBL with a base dose of 60k $\mu\text{C}/\text{cm}^2$, beam current of 100 nA, 500 μm field size, 200k points

CONTACTS AND CROSS OVERS

- Spin 2×PMMA 4% resist at 4000 rpm for 45 s slow acceleration and bake 2 min 115°C
- Define pattern with EBL with a base dose of $1300 \mu\text{C}/\text{cm}^2$, beam current of 10 nA, 500 μm field size, 50k points
- Develop 75 s 1:3 MIBK:IPA followed by 10 s IPA and 30 s Milli Q rinse - blow dry with N₂ and 2 min plasma ashing
- Load device into AJA International metal evaporation system
- Kaufmann argon milling 15 s at 300 V with 15 cm³/min Ar gas flow with ion gas on and 1 mTorr pressure - warm up 60 s before milling
- NbTiN deposition: sputter NbTi in N atmosphere - 180 nm
- Lift off 80°C NMP, acetone, IPA for 1 hr, 1 min, 1 min - blow dry with N₂ and 2 min plasma ashing

WIRE BONDING

- Glued to PCB sample board with PMMA
- Al wire bonded control lines to PCB sample board
- Loading in indium sealed CuBe box and sample holder

References

- [1] A. Einstein, B. Podolsky, and N. Rosen, “Can quantum-mechanical description of physical reality be considered complete?,” *Phys. Rev.*, vol. 47, pp. 777–780, May 1935.
- [2] E. Schrödinger, “Discussion of probability relations between separated systems,” *Mathematical Proceedings of the Cambridge Philosophical Society*, vol. 31, no. 4, p. 555563, 1935.
- [3] N. Bohr, “Can quantum-mechanical description of physical reality be considered complete?,” *Phys. Rev.*, vol. 48, pp. 696–702, Oct 1935.
- [4] I. L. Chuang, “Quantum error correction,” in *Quantum Machines: Measurement and Control of Engineered Quantum Systems*, Lecture Notes of the Les Houches Summer School: Vol. 96, July 2011, Oxford University Press, 2014.
- [5] E. Schrödinger, “Are there quantum jumps? part ii,” *The British Journal for the Philosophy of science*, vol. 3, no. 11, pp. 233–242, 1952.
- [6] R. P. Feynman, “Simulating physics with computers,” *International Journal of Theoretical Physics*, vol. 21, no. 6, pp. 467–488, 1982.
- [7] D. Deutsch, “Quantum theory, the church–turing principle and the universal quantum computer,” in *Proceedings of the Royal Society of London. A. Mathematical and Physical Sciences*, vol. 400, pp. 97–117, The Royal Society London, 1985.
- [8] P. W. Shor, “Algorithms for quantum computation: Discrete logarithms and factoring,” in *Proceedings 35th annual symposium on foundations of computer science*, pp. 124–134, Ieee, 1994.
- [9] L. K. Grover, “A fast quantum mechanical algorithm for database search,” in *Proceedings of the Twenty-Eighth Annual ACM Symposium on Theory of Computing*, STOC 96, (New York, NY, USA), p. 212219, Association for Computing Machinery, 1996.

- [10] M. A. Nielsen and I. L. Chuang, *Quantum Computation and Quantum Information: 10th Anniversary Edition*. USA: Cambridge University Press, 10th ed., 2011.
- [11] J. Bardeen and W. H. Brattain, "The transistor, a semi-conductor triode," *Phys. Rev.*, vol. 74, pp. 230–231, Jul 1948.
- [12] W. Shockley, "Transistor technology evokes new physics," *Nobel lecture*, vol. 11, 1956.
- [13] G. E. Moore, "Cramming more components onto integrated circuits," *Electronics*, vol. 38, Apr 1965.
- [14] D. E. Gottesman, *Stabilizer Codes and Quantum Error Correction*. PhD thesis, California Institute of Technology, 1997.
- [15] B. M. Terhal, "Quantum error correction for quantum memories," *Rev. Mod. Phys.*, vol. 87, pp. 307–346, Apr 2015.
- [16] J. Preskill, "Quantum computing in the nisq era and beyond," *Quantum*, vol. 2, p. 79, 2018.
- [17] D. Leibfried, R. Blatt, C. Monroe, and D. Wineland, "Quantum dynamics of single trapped ions," *Rev. Mod. Phys.*, vol. 75, pp. 281–324, Mar 2003.
- [18] C. D. Bruzewicz, J. Chiaverini, R. McConnell, and J. M. Sage, "Trapped-ion quantum computing: Progress and challenges," *Applied Physics Reviews*, vol. 6, no. 2, p. 021314, 2019.
- [19] R. Hanson, L. P. Kouwenhoven, J. R. Petta, S. Tarucha, and L. M. Vandersypen, "Spins in few-electron quantum dots," *Rev. Mod. Phys.*, vol. 79, no. 4, p. 1217, 2007.
- [20] L. Vandersypen, H. Bluhm, J. Clarke, A. Dzurak, R. Ishihara, A. Morello, D. Reilly, L. Schreiber, and M. Veldhorst, "Interfacing spin qubits in quantum dots and donorshot, dense, and coherent," *npj Quantum Information*, vol. 3, no. 1, p. 34, 2017.
- [21] J. L. O'brien, A. Furusawa, and J. Vučković, "Photonic quantum technologies," *Nat. Photonics*, vol. 3, no. 12, p. 687, 2009.
- [22] C. Weedbrook, S. Pirandola, R. García-Patrón, N. J. Cerf, T. C. Ralph, J. H. Shapiro, and S. Lloyd, "Gaussian quantum information," *Rev. Mod. Phys.*, vol. 84, pp. 621–669, May 2012.

- [23] D. P. DiVincenzo, "The physical implementation of quantum computation," *Fortschritte der Physik: Progress of Physics*, vol. 48, no. 9-11, pp. 771–783, 2000.
- [24] V. Bouchiat, D. Vion, P. Joyez, D. Esteve, and M. Devoret, "Quantum coherence with a single cooper pair," *Physica Scripta*, vol. 1998, no. T76, p. 165, 1998.
- [25] Y. Nakamura, Y. A. Pashkin, and J. S. Tsai, "Coherent control of macroscopic quantum states in a single-cooper-pair box," *Nature*, vol. 398, no. 6730, pp. 786–788, 1999.
- [26] M. Kjaergaard, M. E. Schwartz, J. Braumüller, P. Krantz, J. I.-J. Wang, S. Gustavsson, and W. D. Oliver, "Superconducting qubits: Current state of play," *Annual Review of Condensed Matter Physics*, vol. 11, 2019.
- [27] A. Blais, R.-S. Huang, A. Wallraff, S. M. Girvin, and R. J. Schoelkopf, "Cavity quantum electrodynamics for superconducting electrical circuits: An architecture for quantum computation," *Phys. Rev. A*, vol. 69, no. 6, p. 062320, 2004.
- [28] A. Wallraff, D. I. Schuster, A. Blais, L. Frunzio, R.-S. Huang, J. Majer, S. Kumar, S. M. Girvin, and R. J. Schoelkopf, "Strong coupling of a single photon to a superconducting qubit using circuit quantum electrodynamics," *Nature*, vol. 431, pp. 162–167, Sept. 2004.
- [29] *Exploring the quantum: atoms, cavities, and photons*. Oxford :: Oxford University Press, 2006-08-10.
- [30] J. Koch, T. M. Yu, J. M. Gambetta, A. A. Houck, D. I. Schuster, J. Majer, A. Blais, M. H. Devoret, S. M. Girvin, and R. J. Schoelkopf, "Charge-insensitive qubit design derived from the Cooper pair box," *Phys. Rev. A*, vol. 76, p. 042319, Oct. 2007.
- [31] D. Schuster, A. A. Houck, J. Schreier, A. Wallraff, J. Gambetta, A. Blais, L. Frunzio, J. Majer, B. Johnson, M. Devoret, *et al.*, "Resolving photon number states in a superconducting circuit," *Nature*, vol. 445, no. 7127, p. 515, 2007.
- [32] A. A. Houck, D. I. Schuster, J. M. Gambetta, J. A. Schreier, B. R. Johnson, J. M. Chow, L. Frunzio, J. Majer, M. H. Devoret, S. Girvin, and R. J. Schoelkopf, "Generating single microwave photons in a circuit," *Nature*, vol. 449, no. 7160, p. 328, 2007.

- [33] A. G. Fowler, M. Mariantoni, J. M. Martinis, and A. N. Cleland, "Surface codes: Towards practical large-scale quantum computation," *Phys. Rev. A*, vol. 86, p. 032324, Sep 2012.
- [34] N. Ofek, A. Petrenko, R. Heeres, P. Reinhold, Z. Leghtas, B. Vlastakis, Y. Liu, L. Frunzio, S. Girvin, L. Jiang, *et al.*, "Extending the lifetime of a quantum bit with error correction in superconducting circuits," *Nature*, vol. 536, no. 7617, pp. 441–445, 2016.
- [35] L. Hu, Y. Ma, W. Cai, X. Mu, Y. Xu, W. Wang, Y. Wu, H. Wang, Y. Song, C.-L. Zou, S. M. Girvin, L.-M. Duan, and L. Sun, "Quantum error correction and universal gate set operation on a binomial bosonic logical qubit," *Nat. Phys.*, vol. 15, no. 5, p. 503, 2019.
- [36] F. Arute, K. Arya, R. Babbush, D. Bacon, J. C. Bardin, R. Barends, R. Biswas, S. Boixo, F. G. S. L. Bradao, D. A. Buell, B. Burkett, Y. Chen, Z. Chen, B. Chiaro, R. Collins, W. Courtney, A. Dunsworth, E. Farhi, B. Foxen, *et al.*, "Quantum supremacy using a programmable superconducting processor," *Nature*, vol. 574, no. 7779, pp. 505–510, 2019.
- [37] IBM Quantum Experience [<https://quantum-computing.ibm.com>].
- [38] T. W. Larsen, K. D. Petersson, F. Kuemmeth, T. S. Jespersen, P. Krogstrup, J. Nygard, and C. M. Marcus, "A semiconductor nanowire-based superconducting qubit," *Phys. Rev. Lett.*, vol. 115, p. 127001, 2015.
- [39] G. de Lange, B. van Heck, A. Bruno, D. J. van Woerkom, A. Geresdi, S. R. Plissard, E. P. A. M. Bakkers, A. R. Akhmerov, and L. DiCarlo, "Realization of microwave quantum circuits using hybrid superconducting-semiconducting nanowire josephson elements.," *Phys. Rev. Lett.*, vol. 115, p. 127002, 2015.
- [40] L. Casparis, M. R. Connolly, M. Kjaergaard, N. J. Pearson, A. Kringshøj, T. W. Larsen, F. Kuemmeth, T. Wang, C. Thomas, S. Gronin, G. C. Gardner, M. J. Manfra, C. M. Marcus, and K. D. Petersson, "Superconducting gatemon qubit based on a proximitized two-dimensional electron gas," *Nat. Nanotechnol.*, vol. 13, no. 10, pp. 915–919, 2018.
- [41] J. Kroll, W. Uilhoorn, K. van der Enden, D. de Jong, K. Watanabe, T. Taniguchi, S. Goswami, M. Cassidy, and L. Kouwenhoven, "Magnetic field compatible circuit quantum electrodynamics with graphene josephson junctions," *Nat. Commun.*, vol. 9, no. 1, p. 4615, 2018.

- [42] J. I.-J. Wang, D. Rodan-Legrain, L. Bretheau, D. L. Campbell, B. Kannan, D. Kim, M. Kjaergaard, P. Krantz, G. O. Samach, *et al.*, “Coherent control of a hybrid superconducting circuit made with graphene-based van der waals heterostructures,” *Nat. Nanotechnol.*, vol. 14, no. 2, p. 120, 2019.
- [43] V. Mourik, K. Zuo, S. M. Frolov, S. R. Plissard, E. P. A. M. Bakkers, and L. P. Kouwenhoven, “Signatures of majorana fermions in hybrid superconductor-semiconductor nanowire devices,” *Science*, vol. 336, no. 6084, pp. 1003–1007, 2012.
- [44] E. Ginossar and E. Grosfeld, “Microwave transitions as a signature of coherent parity mixing effects in the Majorana-transmon qubit,” *Nat. Commun.*, vol. 5, p. 4772, Sept. 2014.
- [45] A. Y. Kitaev, “Unpaired Majorana fermions in quantum wires,” *Physics-Uspekhi*, vol. 44, no. 10S, pp. 131–136, 2001.
- [46] H. Paik, D. I. Schuster, L. S. Bishop, G. Kirchmair, G. Catelani, A. P. Sears, B. R. Johnson, M. J. Reagor, L. Frunzio, L. I. Glazman, S. M. Girvin, M. H. Devoret, and R. J. Schoelkopf, “Observation of High Coherence in Josephson Junction Qubits Measured in a Three-Dimensional Circuit QED Architecture,” *Phys. Rev. Lett.*, vol. 107, p. 240501, Dec. 2011.
- [47] L. N. Cooper, “Bound electron pairs in a degenerate fermi gas,” *Phys. Rev.*, vol. 104, pp. 1189–1190, Nov 1956.
- [48] J. Bardeen, L. N. Cooper, and J. R. Schrieffer, “Theory of superconductivity,” *Phys. Rev.*, vol. 108, pp. 1175–1204, Dec 1957.
- [49] M. Tinkham, *Introduction to Superconductivity*. Courier Corporation, 2004.
- [50] H. KAMERLINGH, “Further experiments with liquid helium. C. on the change of electric resistance of pure metals at very low temperatures, etc. iv. the resistance of pure mercury at helium temperatures,” *Comm. Phys. Lab. Univ. Leiden*, vol. 120, 1911.
- [51] S. M. Girvin, “Circuit QED: Superconducting qubits coupled to microwave photons,” in *Quantum Machines: Measurement and Control of Engineered Quantum Systems*, Lecture Notes of the Les Houches Summer School: Vol. 96, July 2011, Oxford University Press, 2014.

- [52] H. Wang, M. Hofheinz, M. Ansmann, R. C. Bialczak, E. Lucero, M. Neeley, A. D. O'Connell, D. Sank, J. Wenner, A. N. Cleland, and J. M. Martinis, "Measurement of the decay of fock states in a superconducting quantum circuit," *Phys. Rev. Lett.*, vol. 101, p. 240401, Dec 2008.
- [53] C. Wang, Y. Y. Gao, P. Reinhold, R. W. Heeres, N. Ofek, K. Chou, C. Axline, M. Reagor, J. Blumoff, K. Sliwa, *et al.*, "A schrödinger cat living in two boxes," *Science*, vol. 352, no. 6289, pp. 1087–1091, 2016.
- [54] B. D. Josephson, "Possible new effects in superconductive tunnelling," *Phys. lett.*, vol. 1, no. 7, pp. 251–253, 1962.
- [55] M. H. Devoret and R. J. Schoelkopf, "Superconducting Circuits for Quantum Information: An Outlook," *Science*, vol. 339, pp. 1169–1174, Mar. 2013.
- [56] A. A. Golubov, M. Y. Kupriyanov, and E. Il'ichev, "The current-phase relation in josephson junctions," *Rev. Mod. Phys.*, vol. 76, pp. 411–469, Apr 2004.
- [57] G. Ithier, E. Collin, P. Joyez, P. J. Meeson, D. Vion, D. Esteve, F. Chiarello, A. Shnirman, Y. Makhlin, J. Schriefl, and G. Schön, "Decoherence in a superconducting quantum bit circuit," *Phys. Rev. B*, vol. 72, p. 134519, Oct 2005.
- [58] J. A. Schreier, A. A. Houck, J. Koch, D. I. Schuster, B. R. Johnson, J. M. Chow, J. M. Gambetta, J. Majer, L. Frunzio, M. H. Devoret, S. M. Girvin, and R. J. Schoelkopf, "Suppressing charge noise decoherence in superconducting charge qubits," *Phys. Rev. B*, vol. 77, p. 180502(R), May 2008.
- [59] P. Krantz, M. Kjaergaard, F. Yan, T. P. Orlando, S. Gustavsson, and W. D. Oliver, "A quantum engineer's guide to superconducting qubits," *Appl. Phys. Rev.*, vol. 6, no. 2, p. 021318, 2019.
- [60] M. Reed, *Entanglement and Quantum Error Correction with Superconducting Qubits*. PhD thesis, Yale University, 2013.
- [61] L. Casparis, T. W. Larsen, M. S. Olsen, F. Kuemmeth, P. Krogstrup, J. Nygård, K. D. Petersson, and C. M. Marcus, "Gatemon benchmarking and two-qubit operations," *Phys. Rev. Lett.*, vol. 116, p. 150505, Apr 2016.
- [62] F. Luthi, T. Stavenga, O. W. Enzing, A. Bruno, C. Dickel, N. K. Langford, M. A. Rol, T. S. Jespersen, J. Nygård, P. Krogstrup, and L. DiCarlo, "Evolution of nanowire transmon qubits and their coherence in a magnetic field," *Phys. Rev. Lett.*, vol. 120, p. 100502, 2018.

- [63] F. Krizek, J. E. Sestoft, P. Aseev, S. Marti-Sánchez, S. Vaitiekėnas, L. Casparis, S. A. Khan, Y. Liu, T. c. v. Stankevič, A. M. Whiticar, A. Fursina, F. Boekhout, R. Koops, E. Uccelli, L. P. Kouwenhoven, C. M. Marcus, J. Arbiol, and P. Krogstrup, “Field effect enhancement in buffered quantum nanowire networks,” *Phys. Rev. Materials*, vol. 2, p. 093401, Sep 2018.
- [64] A. Andreev, “The thermal conductivity of the intermediate state in superconductors,” *JETP*, vol. 19, no. 5, p. 1228, 1964.
- [65] D. A. Ivanov and M. V. Feigel’man, “Two-level hamiltonian of a superconducting quantum point contact,” *Phys. Rev. B*, vol. 59, pp. 8444–8446, Apr 1999.
- [66] D. V. Averin, “Coulomb blockade in superconducting quantum point contacts,” *Phys. Rev. Lett.*, vol. 82, pp. 3685–3688, May 1999.
- [67] D. Ristè, C. Bultink, M. Tiggelman, R. Schouten, K. Lehnert, and L. DiCarlo, “Millisecond charge-parity fluctuations and induced decoherence in a superconducting transmon qubit,” *Nat. Commun.*, vol. 4, p. 1913, 2013.
- [68] C. Janvier, L. Tosi, L. Bretheau, Ç. Ö. Girit, M. Stern, P. Bertet, P. Joyez, D. Vion, D. Esteve, M. F. Goffman, H. Pothier, and C. Urbina, “Coherent manipulation of andreev states in superconducting atomic contacts,” *Science*, vol. 349, no. 6253, pp. 1199–1202, 2015.
- [69] M. Hays, G. de Lange, K. Serniak, D. J. van Woerkom, D. Bouman, P. Krogstrup, J. Nygård, A. Geresdi, and M. H. Devoret, “Direct microwave measurement of andreev-bound-state dynamics in a semiconductor-nanowire josephson junction,” *Phys. Rev. Lett.*, vol. 121, p. 047001, Jul 2018.
- [70] M. T. Bell, J. Paramanandam, L. B. Ioffe, and M. E. Gershenson, “Protected josephson rhombus chains,” *Phys. Rev. Lett.*, vol. 112, p. 167001, Apr 2014.
- [71] T. W. Larsen, *Mesoscopic Superconductivity towards Protected Qubits*. PhD thesis, University of Copenhagen, 2018.
- [72] A. A. Houck, J. A. Schreier, B. R. Johnson, J. M. Chow, J. Koch, J. M. Gambetta, D. I. Schuster, L. Frunzio, M. H. Devoret, S. M. Girvin, and

- R. J. Schoelkopf, "Controlling the Spontaneous Emission of a Superconducting Transmon Qubit," *Phys. Rev. Lett.*, vol. 101, p. 080502, Aug. 2008.
- [73] E. M. Purcell, H. C. Torrey, and R. V. Pound, "Resonance absorption by nuclear magnetic moments in a solid," *Phys. Rev.*, vol. 69, pp. 37–38, Jan 1946.
- [74] M. D. Reed, B. R. Johnson, A. A. Houck, L. DiCarlo, J. M. Chow, D. I. Schuster, L. Frunzio, and R. J. Schoelkopf, "Fast reset and suppressing spontaneous emission of a superconducting qubit," *Applied Physics Letters*, vol. 96, no. 20, p. 203110, 2010.
- [75] R. M. Lutchyn, J. D. Sau, and S. Das Sarma, "Majorana fermions and a topological phase transition in semiconductor-superconductor heterostructures," *Phys. Rev. Lett.*, vol. 105, p. 077001, Aug 2010.
- [76] Y. Oreg, G. Refael, and F. von Oppen, "Helical liquids and majorana bound states in quantum wires," *Phys. Rev. Lett.*, vol. 105, p. 177002, Oct 2010.
- [77] S. M. Albrecht, A. P. Higginbotham, M. Madsen, F. Kuemmeth, T. S. Jespersen, J. Nygård, P. Krogstrup, and C. M. Marcus, "Exponential protection of zero modes in Majorana islands," *Nature*, vol. 531, pp. 206–209, Mar. 2016.
- [78] M. Deng, S. Vaitiekėnas, E. B. Hansen, J. Danon, M. Leijnse, K. Flensberg, J. Nygård, P. Krogstrup, and C. M. Marcus, "Majorana bound state in a coupled quantum-dot hybrid-nanowire system," *Science*, vol. 354, no. 6319, pp. 1557–1562, 2016.
- [79] H. Zhang, C.-X. Liu, S. Gazibegovic, D. Xu, J. A. Logan, G. Wang, N. van Loo, J. D. S. Bommer, M. W. A. de Moor, D. Car, R. L. M. Op het Veld, P. J. van Veldhoven, S. Koelling, M. A. Verheijen, M. Pendharkar, D. J. Pennachio, B. Shojaei, J. S. Lee, C. J. Palmstrøm, E. P. A. M. Bakkers, S. D. Sarma, and L. P. Kouwenhoven, "Quantized Majorana conductance," *Nature*, vol. 556, no. 7699, pp. 74–79, 2018.
- [80] J. Kroll, F. Borsoi, K. van der Enden, W. Uilhoorn, D. de Jong, M. Quintero-Pérez, D. van Woerkom, A. Bruno, S. Plissard, D. Car, E. Bakkers, M. Cassidy, and L. Kouwenhoven, "Magnetic-field-resilient superconducting coplanar-waveguide resonators for hybrid circuit

- quantum electrodynamics experiments," *Phys. Rev. Applied*, vol. 11, p. 064053, Jun 2019.
- [81] O. Erlandsson, "Circuit qed devices for probing majorana zero modes," Master's thesis, University of Copenhagen, 2018.
- [82] A. Keselman, C. Murthy, B. van Heck, and B. Bauer, "Spectral response of Josephson junctions with low-energy quasiparticles," *SciPost Phys.*, vol. 7, p. 50, 2019.
- [83] J. G. Kroll, *Magnetic field compatible hybrid circuit quantum electrodynamics*. PhD thesis, Delft University of Technology, 2019.
- [84] A. Bruno, G. De Lange, S. Asaad, K. Van der Enden, N. Langford, and L. DiCarlo, "Reducing intrinsic loss in superconducting resonators by surface treatment and deep etching of silicon substrates," *Appl. Phys. Lett.*, vol. 106, no. 18, p. 182601, 2015.
- [85] T. Ihn, *Semiconductor Nanostructures: Quantum states and electronic transport*. Oxford University Press, 2010.
- [86] X. Mi, J. Cady, D. Zajac, J. Stehlik, L. Edge, and J. R. Petta, "Circuit quantum electrodynamics architecture for gate-defined quantum dots in silicon," *Appl. Phys. Lett.*, vol. 110, no. 4, p. 043502, 2017.
- [87] COMSOL, Inc., [<https://www.comsol.com>].
- [88] D. M. Pozar, *Microwave engineering*. John Wiley & Sons, 2009.
- [89] P. Krogstrup, N. L. B. Ziino, W. Chang, S. M. Albrecht, M. H. Madsen, E. Johnson, J. Nygård, C. M. Marcus, and T. S. Jespersen, "Epitaxy of semiconductor-superconductor nanowires," *Nat. Mater.*, vol. 14, pp. 400–406, Apr. 2015.
- [90] W. Chang, *Superconducting Proximity Effect in InAs Nanowires*. PhD thesis, Harvard University, 2014.
- [91] F. Krizek, *Semiconductor Nanowire Networks Grown By Molecular Beam Epitaxy: Vapor-Liquid-Solid and Selective Area Growth*. PhD thesis, University of Copenhagen, 2018.
- [92] Z. Chen, A. Megrant, J. Kelly, R. Barends, J. Bochmann, Y. Chen, B. Chiaro, A. Dunsworth, E. Jeffrey, J. Mutus, *et al.*, "Fabrication and characterization of aluminum airbridges for superconducting microwave circuits," *Appl. Phys. Lett.*, vol. 104, no. 5, p. 052602, 2014.

- [93] R. Barends, J. Wenner, M. Lenander, Y. Chen, R. C. Bialczak, J. Kelly, E. Lucero, P. O’Malley, M. Mariantoni, D. Sank, *et al.*, “Minimizing quasiparticle generation from stray infrared light in superconducting quantum circuits,” *Appl. Phys. Lett.*, vol. 99, no. 11, p. 113507, 2011.
- [94] A. D. Córcoles, J. M. Chow, J. M. Gambetta, C. Rigetti, J. R. Rozen, G. A. Keefe, M. Beth Rothwell, M. B. Ketchen, and M. Steffen, “Protecting superconducting qubits from radiation,” *Appl. Phys. Lett.*, vol. 99, no. 18, p. 181906, 2011.
- [95] QDevil [<https://www.qdevil.com>].
- [96] A. Kringshøj, “Readout and control of semiconductor-nanowire-based superconducting qubits,” Master’s thesis, University of Copenhagen, 2016.
- [97] C. Macklin, K. O’Brien, D. Hover, M. E. Schwartz, V. Bolkhovsky, X. Zhang, W. D. Oliver, and I. Siddiqi, “A near-quantum-limited josephson traveling-wave parametric amplifier,” *Science*, vol. 350, no. 6258, pp. 307–310, 2015.
- [98] A. Kringshøj, T. W. Larsen, B. van Heck, D. Sabonis, O. Erlandsson, I. Petkovic, D. I. Pikulin, P. Krogstrup, K. D. Petersson, and C. M. Marcus, “Controlled dc monitoring of a superconducting qubit,” *Phys. Rev. Lett.*, vol. 124, p. 056801, Feb 2020.
- [99] B. R. Johnson, *Controlling Photons in Superconducting Electrical Circuits*. PhD thesis, Yale University, 2011.
- [100] D. C. McKay, C. J. Wood, S. Sheldon, J. M. Chow, and J. M. Gambetta, “Efficient z gates for quantum computing,” *Phys. Rev. A*, vol. 96, p. 022330, Aug 2017.
- [101] A. Kringshøj, L. Casparis, M. Hell, T. W. Larsen, F. Kuemmeth, M. Leijnse, K. Flensberg, P. Krogstrup, J. Nygård, K. D. Petersson, and C. M. Marcus, “Anharmonicity of a superconducting qubit with a few-mode josephson junction,” *Phys. Rev. B*, vol. 97, p. 060508(R), Feb 2018.
- [102] R. Barends, J. Kelly, A. Megrant, A. Veitia, D. Sank, E. Jeffrey, T. C. White, J. Mutus, A. G. Fowler, B. Campbell, Y. Chen, Z. Chen, B. Chiaro, A. Dunsworth, C. Neill, P. J. J. O’Malley, P. Roushan, A. Vainsencher, J. Wenner, A. N. Korotkov, A. N. Cleland, and J. M. Martinis, “Superconducting quantum circuits at the surface code threshold for fault tolerance,” *Nature*, vol. 508, pp. 500–503, Apr. 2014.

- [103] J. Kelly, R. Barends, A. G. Fowler, A. Megrant, E. Jeffrey, T. C. White, D. Sank, J. Y. Mutus, B. Campbell, Y. Chen, Z. Chen, B. Chiaro, A. Dunsworth, I.-C. Hoi, C. Neill, P. J. J. O’Malley, C. Quintana, P. Roushan, A. Vainsencher, J. Wenner, A. N. Cleland, and J. M. Martinis, “State preservation by repetitive error detection in a superconducting quantum circuit,” *Nature*, vol. 519, pp. 66–69, Mar. 2015.
- [104] S. Sheldon, E. Magesan, J. M. Chow, and J. M. Gambetta, “Procedure for systematically tuning up cross-talk in the cross-resonance gate,” *Phys. Rev. A*, vol. 93, p. 060302, Jun 2016.
- [105] L. Bretheau, Ç. Ö. Girit, H. Pothier, D. Esteve, and C. Urbina, “Exciting Andreev pairs in a superconducting atomic contact,” *Nature (London)*, vol. 499, pp. 312–315, July 2013.
- [106] Y.-J. Doh, J. A. van Dam, A. L. Roest, E. P. A. M. Bakkers, L. P. Kouwenhoven, and S. De Franceschi, “Tunable Supercurrent Through Semiconductor Nanowires,” *Science*, vol. 309, pp. 272–275, July 2005.
- [107] E. M. Spanton, M. Deng, S. Vaitiekėnas, P. Krogstrup, J. Nygård, C. M. Marcus, and K. A. Moler, “Current-phase relations of few-mode inas nanowire josephson junctions,” *Nat. Phys.*, vol. 13, pp. 1177–, Aug. 2017.
- [108] W. Chang, S. M. Albrecht, T. S. Jespersen, F. Kuemmeth, P. Krogstrup, J. Nygård, and C. M. Marcus, “Hard gap in epitaxial semiconductor-superconductor nanowires,” *Nat. Nanotechnol.*, vol. 10, pp. 232–236, Mar. 2015.
- [109] C. W. J. Beenakker, “Universal limit of critical-current fluctuations in mesoscopic josephson junctions,” *Phys. Rev. Lett.*, vol. 67, pp. 3836–3839, Dec 1991.
- [110] D. J. van Woerkom, A. Proutski, B. van Heck, D. Bouman, J. I. Väyrynen, L. I. Glazman, P. Krogstrup, J. Nygård, L. P. Kouwenhoven, and A. Geresdi, “Microwave spectroscopy of spinful andreev bound states in ballistic semiconductor josephson junctions,” *Nat. Phys.*, vol. 13, pp. 876–, June 2017.
- [111] S. Chuang, Q. Gao, R. Kapadia, A. C. Ford, J. Guo, and A. Javey, “Ballistic inas nanowire transistors,” *Nano Lett.*, vol. 13, pp. 555–558, Feb. 2013.
- [112] T. S. Jespersen, M. L. Polianski, C. B. Sørensen, K. Flensberg, and J. Nygård, “Mesoscopic conductance fluctuations in inas nanowire-based sns junctions,” *New J. Phys.*, vol. 11, no. 11, pp. 113025–, 2009.

- [113] M. F. Goffman, C. Urbina, H. Pothier, J. Nygård, C. M. Marcus, and P. Krogstrup, "Conduction channels of an inas-al nanowire josephson weak link," *New J. Phys.*, vol. 19, no. 9, pp. 092002–, 2017.
- [114] R. Barends, J. Kelly, A. Megrant, D. Sank, E. Jeffrey, Y. Chen, Y. Yin, B. Chiaro, J. Mutus, C. Neill, P. J. J. O'Malley, P. Roushan, J. Wenner, T. C. White, A. N. Cleland, and J. M. Martinis, "Coherent Josephson Qubit Suitable for Scalable Quantum Integrated Circuits," *Phys. Rev. Lett.*, vol. 111, p. 080502, Aug. 2013.
- [115] ANSYS, Inc., pr [<https://www.ansys.com>].
- [116] D. V. Averin, "Coulomb blockade in superconducting quantum point contacts," *Phys. Rev. Lett.*, vol. 82, pp. 3685–3688, May 1999.
- [117] S. Jezouin, Z. Iftikhar, A. Anthore, F. D. Parmentier, U. Gennser, A. Cavanna, A. Ouerghi, I. P. Levkivskyi, E. Idrisov, E. V. Sukhorukov, L. I. Glazman, and F. Pierre, "Controlling charge quantization with quantum fluctuations," *Nature*, vol. 536, no. 7614, pp. 58–62, 2016.
- [118] A. Kringshøj, B. van Heck, T. W. Larsen, O. Erlandsson, D. Sabonis, P. Krogstrup, L. Casparis, K. D. Petersson, and C. M. Marcus, "Suppressed charge dispersion via resonant tunneling in a single-channel transmon," *arXiv:1911.10011*, 2019.
- [119] B. Douçot and L. B. Ioffe, "Physical implementation of protected qubits," *Rep. Prog. Phys.*, vol. 75, no. 7, p. 072001, 2012.
- [120] A. Bargerbos, W. Uilhoorn, C.-K. Yang, P. Krogstrup, L. P. Kouwenhoven, G. de Lange, B. van Heck, and A. Kou, "Controlling the charge dispersion of a nearly-open superconducting island," *arXiv preprint arXiv:1911.10010*, 2019.
- [121] P. A. Smith, C. D. Nordquist, T. N. Jackson, T. S. Mayer, B. R. Martin, J. Mbainyo, and T. E. Mallouk, "Electric-field assisted assembly and alignment of metallic nanowires," *Appl. Phys. Lett.*, vol. 77, no. 9, pp. 1399–1401, 2000.
- [122] E. M. Freer, O. Grachev, X. Duan, S. Martin, and D. P. Stumbo, "High-yield self-limiting single-nanowire assembly with dielectrophoresis," *Nat. Nanotechnol.*, vol. 5, no. 7, p. 525, 2010.

- [123] X. Duan, C. Niu, V. Sahi, J. Chen, J. W. Parce, S. Empedocles, and J. L. Goldman, "High-performance thin-film transistors using semiconductor nanowires and nanoribbons," *Nature*, vol. 425, no. 6955, p. 274, 2003.
- [124] M. Li, R. B. Bhiladvala, T. J. Morrow, J. A. Siess, K.-K. Lew, J. M. Redwing, C. D. Keating, and T. S. Mayer, "Bottom-up assembly of large-area nanowire resonator arrays," *Nat. Nanotechnol.*, vol. 3, no. 2, p. 88, 2008.
- [125] L. Tosi, C. Metzger, M. F. Goffman, C. Urbina, H. Pothier, S. Park, A. L. Yeyati, J. Nygård, and P. Krogstrup, "Spin-orbit splitting of Andreev states revealed by microwave spectroscopy," *Phys. Rev. X*, vol. 9, p. 011010, Jan 2019.
- [126] K. Zuo, V. Mourik, D. B. Szombati, B. Nijholt, D. J. van Woerkom, A. Geresdi, J. Chen, V. P. Ostroukh, A. R. Akhmerov, S. R. Plissard, D. Car, E. P. A. M. Bakkers, D. I. Pikulin, L. P. Kouwenhoven, and S. M. Frolov, "Supercurrent interference in few-mode nanowire Josephson junctions," *Phys. Rev. Lett.*, vol. 119, p. 187704, Nov 2017.
- [127] V. Ambegaokar and A. Baratoff, "Tunneling between superconductors," *Phys. Rev. Lett.*, vol. 11, pp. 104–104, Jul 1963.
- [128] F. E. Schmidt, M. D. Jenkins, K. Watanabe, T. Taniguchi, and G. A. Steele, "A ballistic graphene superconducting microwave circuit," *Nat. Commun.*, vol. 9, no. 1, p. 4069, 2018.
- [129] T. Klapwijk, G. Blonder, and M. Tinkham, "Explanation of subharmonic energy gap structure in superconducting contacts," *Physica (Amsterdam)*, vol. 109(B+C), pp. 1657–1664, 1982.
- [130] R. L. Kautz and J. M. Martinis, "Noise-affected i-v curves in small hysteretic Josephson junctions," *Phys. Rev. B*, vol. 42, pp. 9903–9937, Dec 1990.
- [131] Y. Chen, C. Neill, P. Roushan, N. Leung, M. Fang, R. Barends, J. Kelly, B. Campbell, Z. Chen, B. Chiaro, A. Dunsworth, E. Jeffrey, A. Megrant, J. Mutus, P. O'Malley, C. Quintana, D. Sank, A. Vainsencher, J. Wenner, T. White, M. R. Geller, A. Cleland, and J. M. Martinis, "Qubit Architecture with High Coherence and Fast Tunable Coupling," *Phys. Rev. Lett.*, vol. 113, p. 220502, Nov. 2014.
- [132] L. Casparis, N. J. Pearson, A. Kringshøj, T. W. Larsen, F. Kuemmeth, J. Nygård, P. Krogstrup, K. D. Petersson, and C. M. Marcus,

- "Voltage-controlled superconducting quantum bus," *Phys. Rev. B*, vol. 99, p. 085434, Feb 2019.
- [133] P. J. Jones, J. A. M. Huhtamäki, J. Salmilehto, K. Y. Tan, and M. Möttönen, "Tunable electromagnetic environment for superconducting quantum bits," *Sci. Rep.*, vol. 3, p. 1987, 2013.
- [134] R. Ma, B. Saxberg, C. Owens, N. Leung, Y. Lu, J. Simon, and D. I. Schuster, "A dissipatively stabilized Mott insulator of photons," *Nature (London)*, vol. 566, no. 7742, pp. 51–57, 2019.
- [135] S. De Franceschi, L. Kouwenhoven, C. Schönenberger, and W. Wernsdorfer, "Hybrid superconductor–quantum dot devices," *Nat. Nanotechnol.*, vol. 5, no. 10, p. 703, 2010.
- [136] R. M. Lutchyn, G. W. Winkler, B. Van Heck, T. Karzig, K. Flensberg, L. I. Glazman, and C. Nayak, "Topological superconductivity in full shell proximitized nanowires," *arXiv:1809.05512*, 2018.
- [137] S. Vaitiekėnas, M.-T. Deng, P. Krogstrup, and C. M. Marcus, "Flux-induced majorana modes in full-shell nanowires," *arXiv:1809.05513*, 2018.
- [138] Y. Makhlin, G. Schön, and A. Shnirman, "Quantum-state engineering with josephson-junction devices," *Rev. Mod. Phys.*, vol. 73, pp. 357–400, May 2001.
- [139] K. Flensberg, "Capacitance and conductance of mesoscopic systems connected by quantum point contacts," *Phys. Rev. B*, vol. 48, pp. 11156–11166, Oct 1993.
- [140] K. A. Matveev, "Coulomb blockade at almost perfect transmission," *Phys. Rev. B*, vol. 51, pp. 1743–1751, Jan 1995.
- [141] Y. V. Nazarov, "Coulomb blockade without tunnel junctions," *Phys. Rev. Lett.*, vol. 82, pp. 1245–1248, Feb 1999.
- [142] S. R. Patel, S. M. Cronenwett, D. R. Stewart, A. G. Huibers, C. M. Marcus, C. I. Duruöz, J. S. Harris, K. Campman, and A. C. Gossard, "Statistics of coulomb blockade peak spacings," *Phys. Rev. Lett.*, vol. 80, pp. 4522–4525, May 1998.

- [143] D. Duncan, D. Goldhaber-Gordon, R. Westervelt, K. Maranowski, and A. Gossard, "Coulomb-blockade spectroscopy on a small quantum dot in a parallel magnetic field," *Appl. Phys. Lett.*, vol. 77, no. 14, pp. 2183–2185, 2000.
- [144] L. Glazman and K. Matveev, "Resonant josephson current through kondo impurities in a tunnel barrier," *JETP Lett.*, vol. 49, no. 10, p. 659, 1989.
- [145] C. W. J. Beenakker and H. van Houten, "Resonant josephson current through a quantum dot," in *Single-Electron Tunneling and Mesoscopic Devices* (H. Koch and H. Lübbig, eds.), (Berlin, Heidelberg), pp. 175–179, Springer Berlin Heidelberg, 1992.
- [146] I. A. Devyatov and M. Y. Kupriyanov, "Resonant josephson tunneling through s-i-s junctions of arbitrary size," *JETP*, vol. 85, pp. 189–194, Jul 1997.
- [147] S. Hart, Z. Cui, G. Ménard, M. Deng, A. E. Antipov, R. M. Lutchyn, P. Krogstrup, C. M. Marcus, and K. A. Moler, "Current-phase relations of inas nanowire josephson junctions: From interacting to multimode regimes," *Phys. Rev. B*, vol. 100, p. 064523, Aug 2019.
- [148] A. Larkin and K. Matveev, "Current-voltage characteristics of mesoscopic semiconductor contacts," *JETP*, vol. 66, no. 3, p. 590, 1987.
- [149] D. A. Ivanov and M. V. Feigel'man, "Coulomb effects in a ballistic one-channel s-s-s device," *JETP*, vol. 87, pp. 349–356, Aug 1998.
- [150] A. Zazunov, V. S. Shumeiko, G. Wendin, and E. N. Bratus', "Dynamics and phonon-induced decoherence of andreev level qubit," *Phys. Rev. B*, vol. 71, p. 214505, Jun 2005.
- [151] E. Vecino, A. Martín-Rodero, and A. Levy Yeyati, "Josephson current through a correlated quantum level: Andreev states and π junction behavior," *Phys. Rev. B*, vol. 68, p. 035105, Jul 2003.
- [152] A. Martín-Rodero and A. Levy Yeyati, "Josephson and andreev transport through quantum dots," *Advances in Physics*, vol. 60, no. 6, pp. 899–958, 2011.
- [153] A. Kringshøj, G. W. Winkler, T. W. Larsen, D. Sabonis, O. Erlandsson, P. Krogstrup, B. van Heck, K. D. Petersson, and C. M. Marcus, "Phase-twisted andreev states in proximitized semiconducting josephson junctions," *in preparation*, 2020.

- [154] C. W. J. Beenakker and H. van Houten, "Josephson current through a superconducting quantum point contact shorter than the coherence length," *Phys. Rev. Lett.*, vol. 66, pp. 3056–3059, Jun 1991.
- [155] M. Hays, V. Fatemi, K. Serniak, D. Bouman, S. Diamond, G. de Lange, P. Krogstrup, J. Nygård, A. Geresdi, and M. Devoret, "Continuous monitoring of a trapped, superconducting spin," *arXiv:1908.02800*, 2019.
- [156] W. A. Little and R. D. Parks, "Observation of quantum periodicity in the transition temperature of a superconducting cylinder," *Phys. Rev. Lett.*, vol. 9, pp. 9–12, Jul 1962.
- [157] D. Sabonis, O. Erlandsson, A. Kringshøj, T. W. Larsen, I. Petkovic, B. van Heck, P. Krogstrup, K. D. Petersson, and C. M. Marcus, "Little-Parks effect in a semiconductor-based superconducting qubit," *in preparation*, 2020.
- [158] S. Vaitiekėnas, G. W. Winkler, B. van Heck, T. Karzig, M. T. Deng, K. Flensberg, L. Glazman, C. Nayak, P. Krogstrup, R. M. Lutchyn, and C. M. Marcus, "Flux-induced topological superconductivity in full-shell nanowires," *to be published*, 2020.